UNCLASSIFIED

AD 262 543

UNCLASSIFIED

DISCLAIMER NOTICE

THIS DOCUMENT IS THE BEST

QUALITY AVAILABLE.

COPY FURNISHED CONTAINED

A SIGNIFICANT NUMBER OF

PAGES WHICH DO NOT

REPRODUCE LEGIBLY.

Reentry Physics
&
Project PRESS Programs

Semiannual Technical Summary Report
to the
Advanced Research Projects Agency

30 June 1961

Lincoln Laboratory

Massachusetts Institute of Technology

Unclassified

MASSACHUSETTS INSTITUTE OF TECHNOLOGY

LINCOLN LABORATORY

REENTRY PHYSICS

&

PROJECT PRESS PROGRAMS

SEMIANNUAL TECHNICAL SUMMARY REPORT

TO THE

ADVANCED RESEARCH PROJECTS AGENCY

1 JANUARY 1961 – 30 JUNE 1961

ISSUED 3 AUGUST 1961

LEXINGTON   MASSACHUSETTS

ASTIA

SEP 7 1961

Unclassified

TABLE OF CONTENTS

TABLE OF CONTENTS (Continued)

FOREWORD

This report describes the program in reentry physics being conducted by Lincoln Laboratory with the support of the Advanced Research Projects Agency. Many groups and individuals have contributed to various parts of the activity. The management responsibility for the program resides in Division 3, Radio Physics, J. V. Harrington, Head. The responsibility for the planning, conduct and coordination of the over-all activities associated with the program is assigned to Group 312, Electromagnetics, G. F. Pippert, Leader, L. J. Sullivan Associate Leader, and S. Edelberg, Assistant Leader. The engineering and design of the reentry test-vehicle system have been provided by the Aerodynamics Branch, W. N. Gardner, Chief, Systems Applications Section of the Applied Materials and Physics Division, National Aeronautics and Space Administration, Langley Research Center, Virginia. The hypervelocity model shots were monitored at the Hypervelocity Ballistic Range, National Aeronautics and Space Administration, Ames Research Center, Moffett Field, California.

Major engineering and scientific contributions to the program are being provided by Division 2, Systems, C. R. Wieser Head, through the efforts of Group 21, Surveillance, O. V. Fortier, Leader, and L. C. Wilber, Associate Leader, Division 4, Radar, J. Freedman Head through Group 47, Radar Receivers, D. L. Clark, Leader, Division 7, Engineering, J. A. Vitale, Head, through Group 75 Construction Engineering, D. C. Moore, Leader. Additional contributions in Division 3 were provided by Group 32, Pacific Range Measurements, P. B. Sebring Leader, Group 35, Plasma Physics, M. A. Herlin Leader, Group 39 Engineering Services, E. W. Blaisdell, Leader, Group 315, Antennas, L. J. Ricardi, Leader. Principal individual contributors to the various phases of the effort are listed with the sections of the report.

The management responsibility for the PRESS Program resides in Division 3, Radio Physics, J. V. Harrington, Head. The responsibility for the planning, conduct, and coordination of the over-all activities of the PRESS Program is assigned to G. F. Pippert, PRESS Program Leader, and P. B. Sebring, Associate Leader.

iv

I. INTRODUCTION AND SUMMARY

This report is the fifth Semiannual Technical Summary Report required by Air Force Contract No. AF 19(604)-7400 under which the work in reentry physics at Lincoln Laboratory is performed. The reporting period for this report is from 1 January 1961 to 30 June 1961.

Laminar equilibrium far-wake results have been obtained theoretically which are appropriate to the enhancement region of the Trailblazer Ie reentry. These results include fluid velocities, enthalpies, air-density axial variations, axial temperature variations, axial electron-density variations, axial variations for NO vibration-rotation radiation, and the variation of total infrared radiation from the wake as a function of altitude.

The General Applied Sciences Laboratories, Inc., on subcontract to Lincoln Laboratory, has completed the flow calculations around the Trailblazer I body and the near wake, including trailing shocks. Similar calculations for the Trailblazer II body are in progress.

Photography of the turbulent wakes of pellets in the Lincoln Hypervelocity Ballistic Range has been extended downward in pressure to 40 mm Hg, and the laminar-turbulent transition has been observed directly. Motion pictures show clearly the growth of the wake, the slowing of the forward component of velocity in the wake, the evolution of the individual eddies, and the growth of 'feathers' and other fine structure.

A series of low-pressure shots at the NASA Ames HBR has been monitored with Lincoln's diagnostic equipment. Some of these have been interpreted and yield quantitative information of trail characteristics which are reliable to about an order of magnitude. The causes of the scatter in the data are being traced, and improvements in equipment and experimental techniques are being made in order to obtain more accurate pellet wake characteristics.

In the area of electromagnetic far field scattering from plasma configurations, new theoretical results have been obtained for scattering from a sphere consisting of a series of concentric plasma shells, scattering from an infinite plasma cylinder with a radial variation in electron density, and the analysis of leaky wave modes on plasma cylinders.

The Optical Laboratory was completed in March 1961, and the base pedestal, primary mirror and servo-control electronics for the 48-inch tracking and spectrometric telescope were installed. Initial tests indicate that the boresight requirement has been realized, and the static tracking error has been decreased to approximately 20 sec of arc.

The present S-band conical-scan tracking system at Wallops Island is being converted to monopulse in order to provide a modulation-free data channel through which both pulse-to-pulse amplitude and phase measurements can be made. A coherent klystron transmitter with 0.2-μsec to 1.5-μsec pulse capability is also being added through the sum channel of the above modification in order to improve the pulse shape measurements. Other radar improvements involve the addition of an orthogonal receiving system to the UHF radar to observe any depolarization effects from the turbulent wake. Also, the UHF radar has been made fully coherent, and phase shape, along with pulse shape, has been recorded.

Trailblazer If was fired on 17 January 1961, and its reentry body carried an outer shell of copper. S-band and UHF pulse radar scattering data were obtained. A strong enhancement in the S-band cross section of 30 to 35 db is observed at about 190,000 ft altitude. Large enhancements are observed until about 125,000 ft. Within this altitude range, the large fluctuations in the data indicate possible turbulence in the wake. UHF enhancement amounts to about 35 db. The major rise in cross section takes place at the same altitude as the large increase in S-band cross section, but the increase in measured cross section is more rapid at UHF.

Trailblazer Ig was fired on 21 April 1961, and its outer shell material was aluminum. A shaped charge carried by the sixth stage was ignited at 760 kft altitude to propel a steel pellet about 3/32 inch thick and 1/2 inch in diameter downward at a very high reentry velocity. The Super Schmidt cameras were used to obtain optical radiation data from both the sixth (aluminum) and seventh (steel) stages.

Trailblazer Ih was fired on 18 May 1961, and its outer shell material was iron. The optical reentry was observed by the Super Schmidt camera.

Equipment was used during the Trailblazer If firing to measure pulse amplitude shape and pulse phase shape at UHF. These remained "well behaved" until about 195,000 ft altitude. Then, for about 0.1 sec, a "tail" of about 6-μsec duration appeared behind the otherwise normal pulse. Below 190,000 ft the pulse shapes became anomalous. In the area of optical data interpretation, theoretical computations for optical radiation from an equilibrium gas cap have been computed and compared with observed results for the Trailblazer Ie firing.

Several studies for Project PRESS are in progress. A study of the various sources of error is being made in order to determine the component requirements of the Airborne Optics Control Subsystem. Another study has shown that the station-keeping computer need be only one-tenth as fast as an IBM 7090 and will require about 1000 words of core storage. A study of available radio altimeters has narrowed the possibilities to either the AN/APN-42 or the AN/APN-110. Studies are also continuing in the areas of search and tracking radars, beacons, inertial reference systems, and optical mounts.

II. FLOW FIELD STUDIES[*]

A. FLOW FIELD STUDIES AT LINCOLN LABORATORY

The laminar equilibrium far-wake program described in an earlier Semi-annual Report[1] has been run for four combinations of altitudes and speeds:

Altitude (ft)	Speed (ft/sec)
150,000	17,300
140,000	16,350
130,000	15,000
125,000	14,100

These represent measured values lying within the region of radar and radiation enhancement during reentry of Trailblazer Ie (see Ref. 1).

For the calculations of far-wake properties, the initial profiles for $[1 - (u/u_\infty)]$ and $[(h/h_\infty) - 1]$ were taken as Gaussian of the form

$$1 - (u/u_\infty) = u_0 \, e^{-\gamma R^2} \quad , \tag{II-1}$$

$$(h/h_\infty) - 1 = h_0 \, e^{-\beta R^2} \quad . \tag{II-2}$$

Here u, h, and ρ are the speed, enthalpy, and density, respectively. The subscript ∞ refers to ambient values. R is defined by the relation

$$R^2 = 2/r_n^2 \int_0^r (\rho/\rho_\infty) \, r \, dr \quad , \tag{II-3}$$

where r is the radial coordinate and r_n is the nose radius. The four quantities u_0, h_0, γ, and β are then determined as functions of the axial coordinates by methods similar to those of S. Feldman[2] and will not be discussed further. In these calculations the initial values of γ and β were taken to be unity. In Ref. 2, and also in a report by P. Lykoudis,[3] appropriate values for the initial Gaussian widths γ and β have been discussed. We have calculated initial

---

[*] The flow field studies in this section were performed by E. L. Murphy; the programming for these studies by L. B. Raisty and L. G. Peterson; computations by N. E. Holway,. all of Group 312.

profiles for $[1 - (u/u_\infty)]$ and $[(h/h_\infty) - 1]$ using isentropic expansion from the bow shock to the ambient pressure of the far wake, with a bow shock for a hemispherical nose given by[4]

$$X = \frac{r^2}{2(r_n + \Delta)} \quad , \tag{II-4}$$

$$\Delta = \frac{2}{3} \frac{r_n}{[(\rho_2/\rho_1) - 1]} \quad , \tag{II-5}$$

where X is the axial distance from the apex of the shock, r is the radial coordinate, Δ is the shock stand-off distance, and ρ_2/ρ_1 is the density ratio across the shock. For example, in Figs. II-1 and II-2, initial profiles calculated in this way are compared with the Gaussian profiles. However, it is probably not too meaningful to ask what represents a good fit because of the approximation methods used to integrate the differential equations for the far wake.

In Figs. II-3 through II-6, the axial variation of air density, temperature, electron density, and NO vibration-rotation radiation are presented for the four sets of flight conditions. In these figures, x_2 is the axial distance measured from the region behind the vehicle where the pressure can be considered to have returned to the undisturbed value. From blast theory,[5] $(M_\infty^2/5)\, r_n$ is a reasonable estimate of the distance behind the vehicle where the far wake begins. M_∞ is the flight Mach number.

For the radiation calculations, the formulae for emissivities from the report by Kivel and Bailey[6] were used together with the composition of equilibrium air as a function of temperature, at fixed pressure. The latter was determined from a Lincoln Laboratory machine program that calculates the composition of equilibrium air for any increment of temperature with pressure as an input. The radial variations were integrated to give I, the intensity of radiation per unit length of trail.

In Fig. II-7, the variation of the total radiation, $\mathcal{I}$, of NO vibration-rotation radiation from the trail (the area under the curves of Fig. II-6) is presented as a function of altitude.
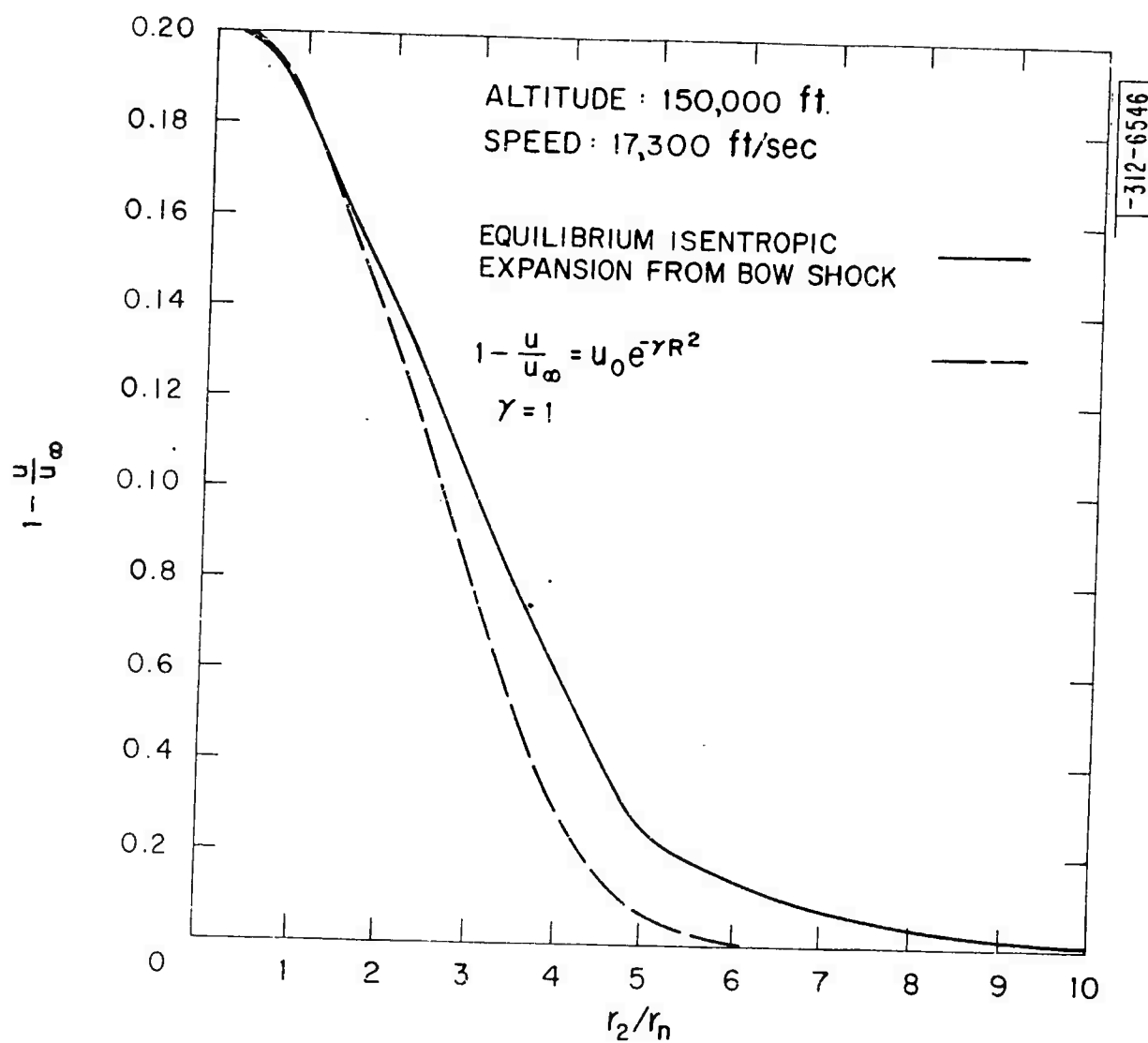
Fig. II-1. Radial variation of fluid speed at $x_2/r_n = 0$.
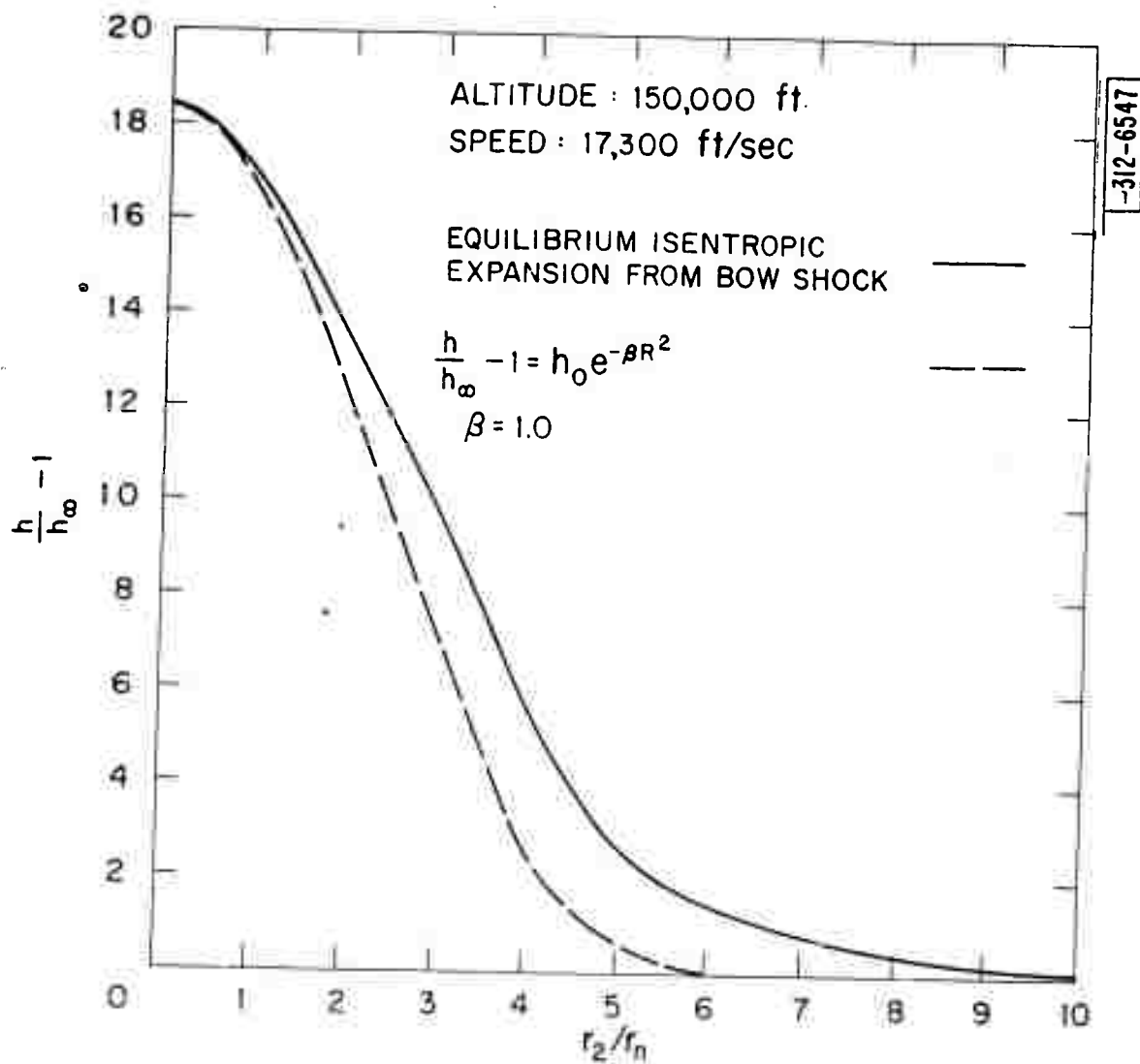
Fig. II-2. Radial variation of enthalpy at $x_2/r_n = 0$.
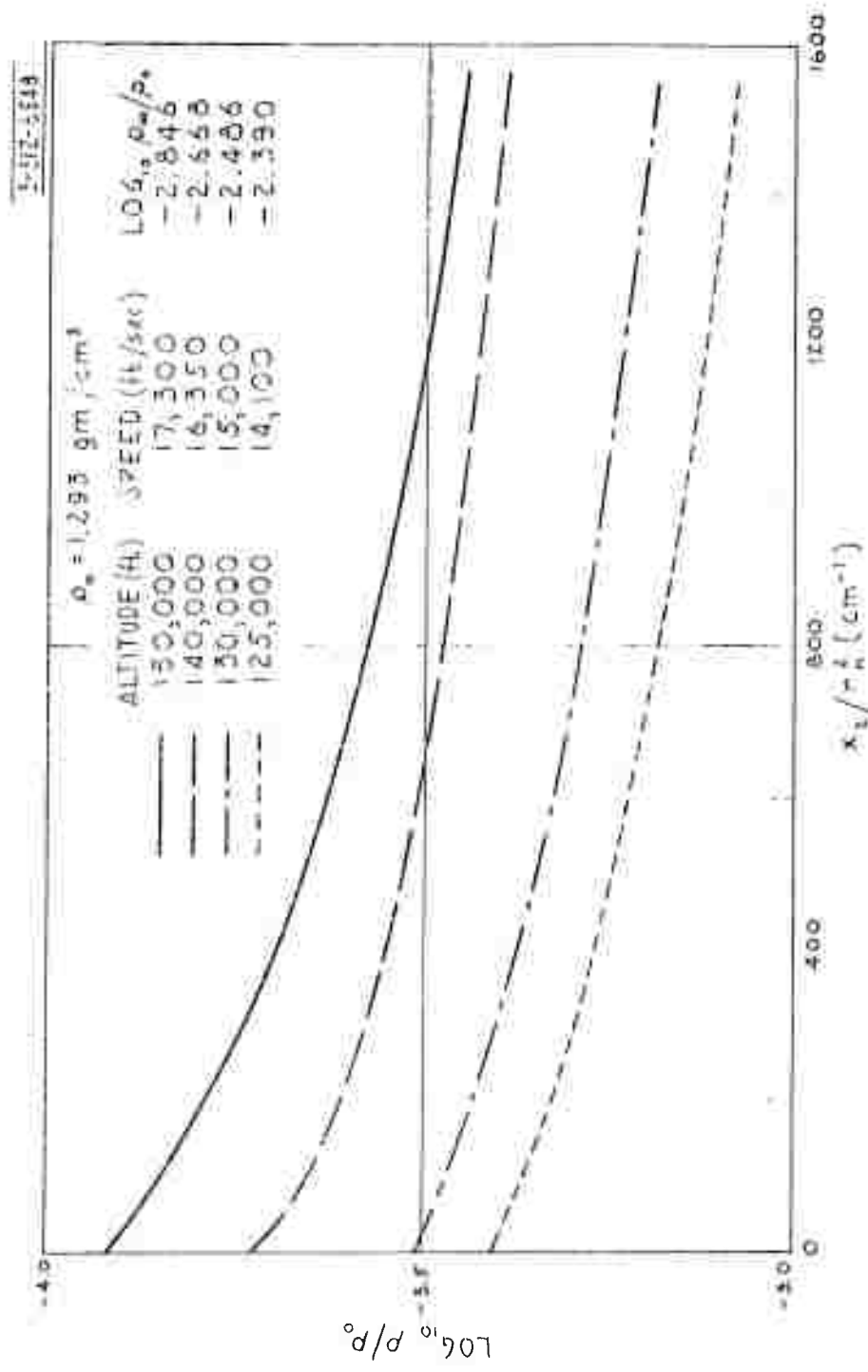
Fig. II-3.   Far-wake air-density axial variation.

-312-6549

ALTITUDE (ft)	VELOCITY (ft/sec)
150,000	17,300
140,000	16,350
130,000	15,000
125,000	14,100

x_2/r_n^2 (cm^{-1})

TEMP ($^\circ$K)

3000

2000

1000

200   400   600   800   1000   1200   1400
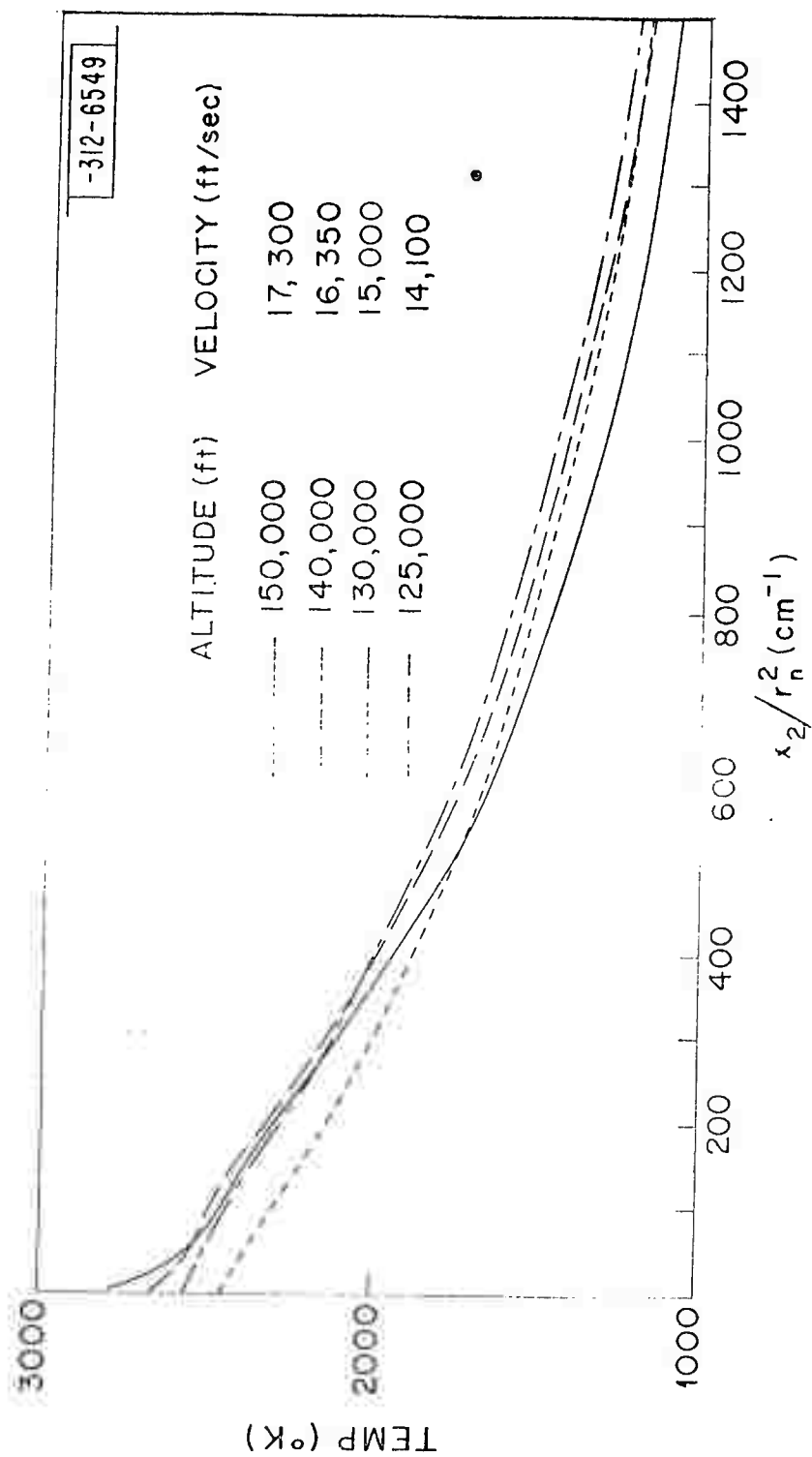
Fig. II-4. Far-wake axial temperature variation.
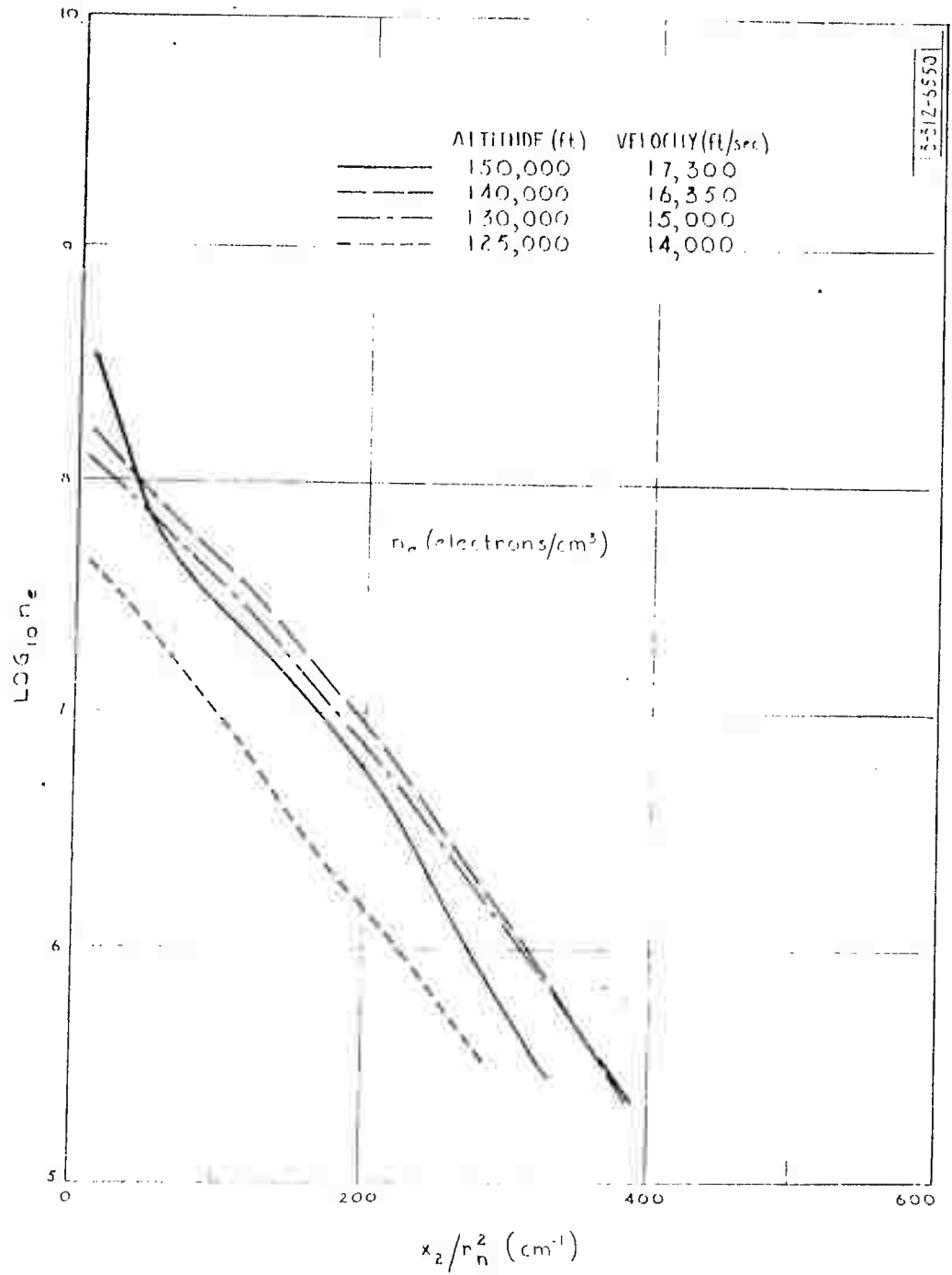
Fig. II-5. Far-wake axial electron-density variation.
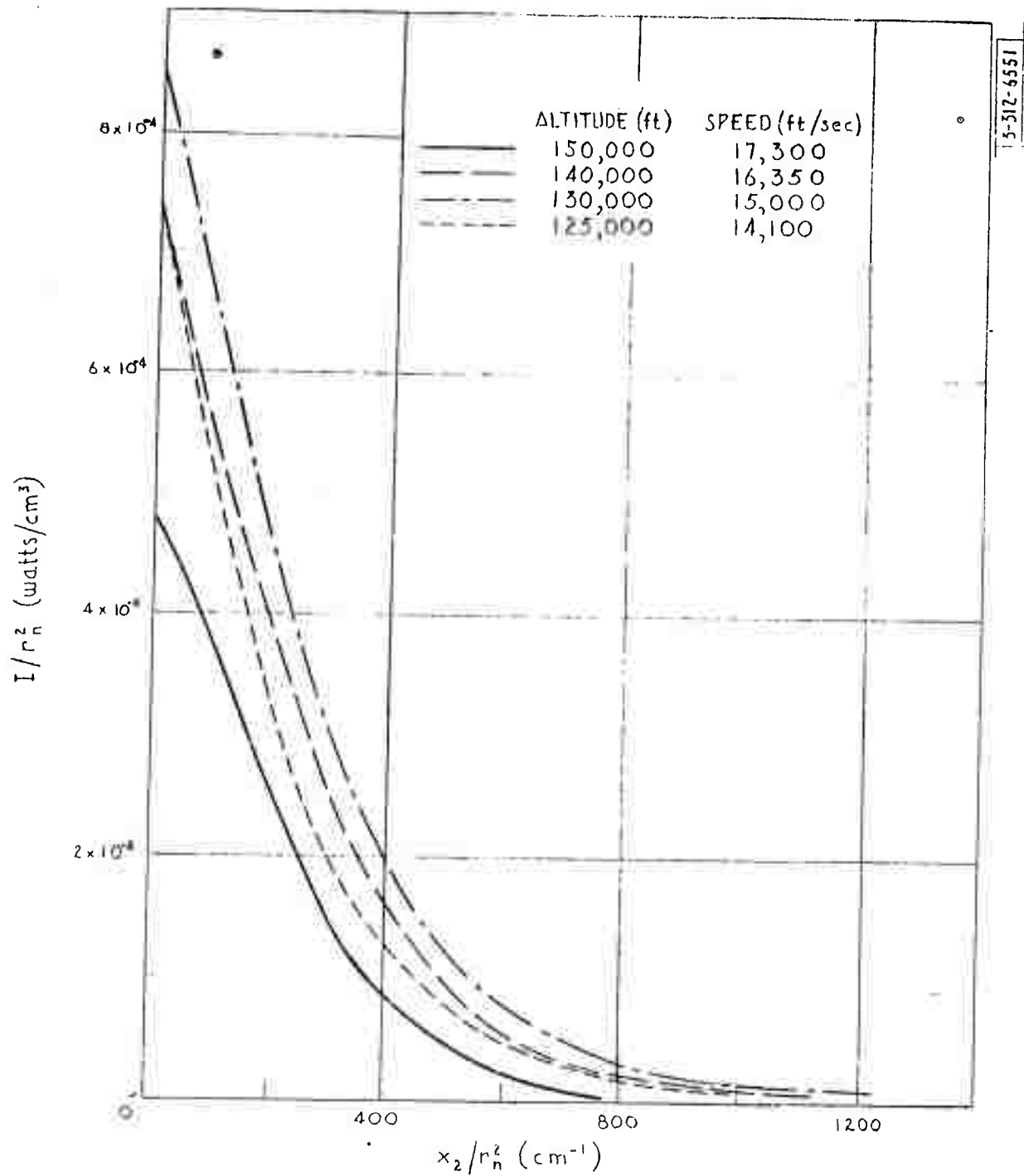
Fig. II-6. Far-wake axial variation for NO vibration-rotation radiation.
I ≡ thermal radiation intensity per unit length.
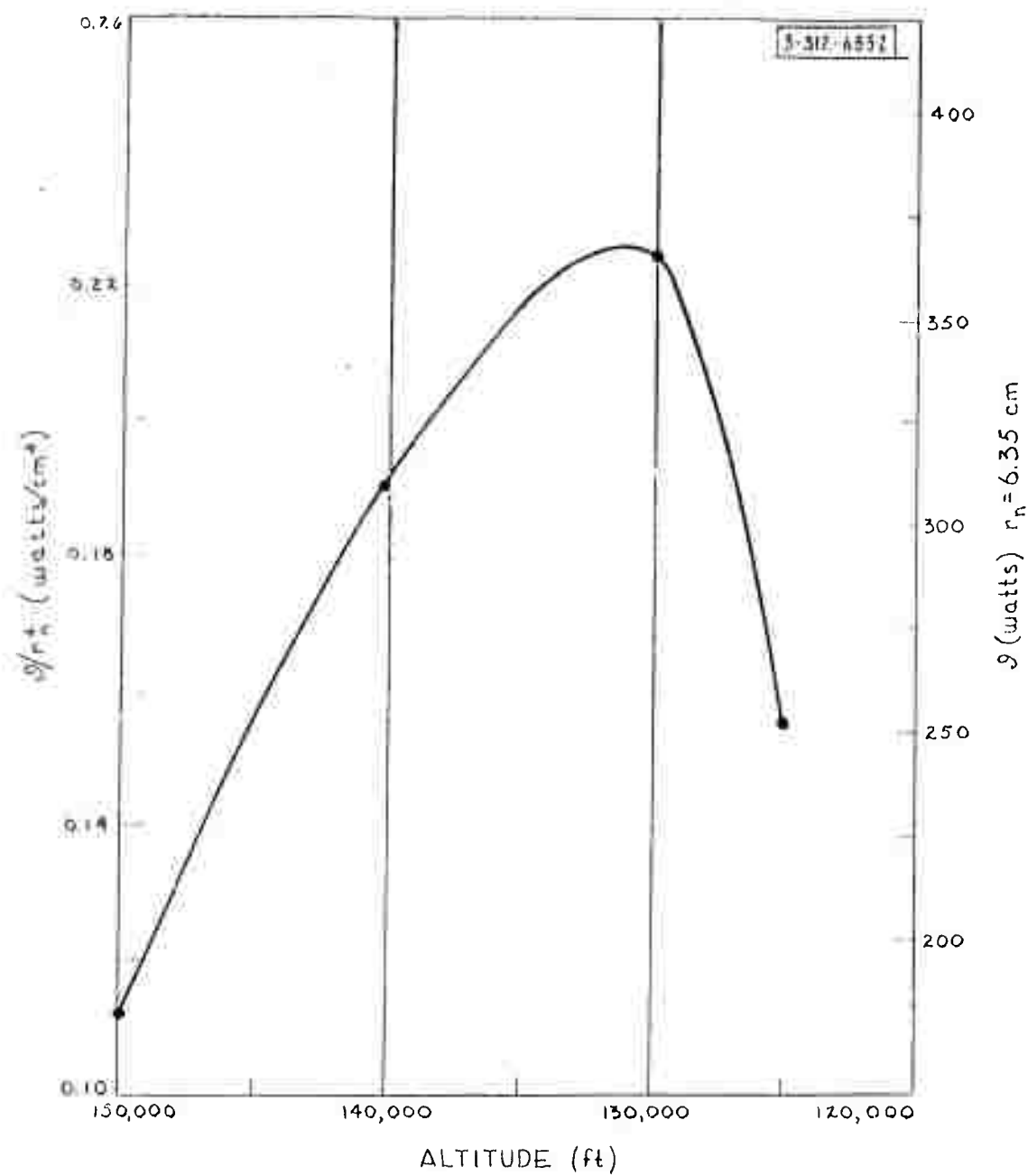
Fig. II-7. NO vibration-rotation radiation from far wake based on laminar equilibrium calculation. $\mathcal{J} \equiv$ total thermal radiation from far wake.
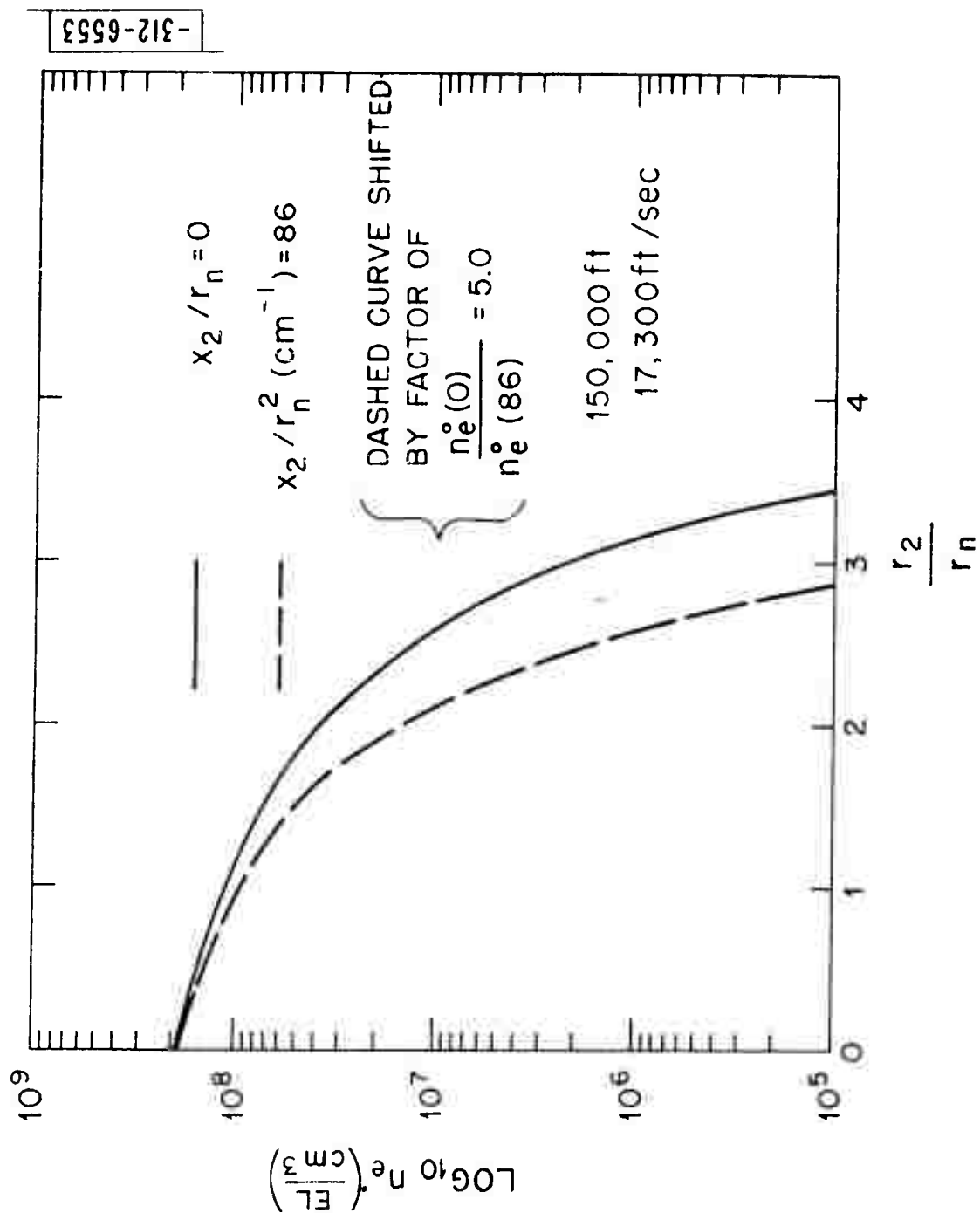
Fig. II-8. Electron-density radial variation.

The figure shows a plot with:
- Box label: -312-6553-
- Vertical axis: $\text{LOG}_{10}\, n_e \left(\frac{EL}{cm^3}\right)$ ranging from 10^5 to 10^9
- Horizontal axis: $\dfrac{r_2}{r_n}$ ranging from 0 to 4

Legend:
- (solid line) $x_2/r_n = 0$
- (dashed line) $x_2/r_n^2\,(cm^{-1}) = 86$

DASHED CURVE SHIFTED BY FACTOR OF $\dfrac{n_e^{\circ}(0)}{n_e^{\circ}(86)} = 5.0$

150,000 ft

17,300 ft/sec

For the first set of flight parameters, 150,000 ft and 17,300 ft/sec, the radial electron-density profiles at two axial locations are compared in Fig. II-8. In the notation on Fig. II-8, the symbol $n_e^o(x_2/r_n^2)$ is the electron density on the axis. The dashed curve has been shifted as indicated. Note the relatively small change in the shape of the profiles.

B.   FLOW FIELD CALCULATIONS BY GASL[*]

1.   Trailblazer I Vehicles

Detailed flow calculations for a reentry body of a shape approximating that of the Trailblazer I series vehicles of the Wallops Island Reentry Program have been completed by the General Applied Science Laboratories, Inc. under Subcontract No. 226 for Lincoln Laboratory. In the Semiannual Report for December 1960 (Ref. 1), the effect of a laminar equilibrium boundary layer on the downstream wake and the results of calculations for the far wake were described for altitudes of 250,000, 200,000 and 150,000 ft. Flight conditions were taken from the calculated trajectory presented in Fig. VII-3 of Ref. 7. The final report[8] on Trailblazer I vehicles covers the flow around the body and the near wake including trailing shocks. The results described in that report are summarized here.

Preliminary studies indicated that the flow in the subsonic and slightly supersonic regions was in thermodynamic and chemical equilibrium. An existing GASL machine program was used to generate the flow properties in this region as initial conditions for continuing the calculations around the body. The supersonic region and the remainder of the bow shock were developed by the method of characteristics programmed for an IBM 704. The chemical composition was considered frozen in this region except at points immediately behind the extended shock where equilibrium conditions were assumed in calculating the initial composition. Throughout the flow field, the degree of ionization was calculated for the reaction $N + O \leftrightarrows NO^+ + e$ based on this reaction being in equilibrium at the local temperature and density of the frozen chemistry flow

---

[*] Performed for Lincoln Laboratory under Subcontract No. 226.

field. The justification for these simplifications followed from detailed calculations of the rate processes by Bloom and Steiger.[9]

The location and shape of trailing and wake shocks were estimated, and it was found that these shocks cause order-of-magnitude increases in electron concentration. In Fig. II-9, the various shocks and some of the streamlines for 150,000 ft and 18,900 ft/sec are presented. A cylinder with radius one-half that of the nose has been assumed to extend downstream from the wake shock. This addition is suggested by photographs of actual wakes where the wake shocks begin, roughly, this distance from the axis; furthermore, the characteristics equations require special treatment if they are to be used near the axis.

Pressure, density, temperature, and electron-density distributions across the shock layer are given in Figs. II-10(a-d) at stations A, B and C of Fig. II-9 In these figures, $\overline{y}$ is the distance from the body surface to the radial point considered divided by the distance between the body surface and the shock.

In Figs II-11(a-d), profiles for the same quantities are given at a distance of 9 nose radii downstream of the nose These profiles show the effects of the trailing shocks.

In Figs. II-12(a-d), the profiles are given for a location 23 nose radii downstream of the vehicle nose. At this distance, the profiles have become smooth; the trailing shock discontinuities at location $x/r_n = 9.0$ disappear as the far wake is approached.

Profiles for chemical composition have also been calculated and these, together with the thermodynamic variable profiles, are presently being used to estimate radiation from these regions of the flow field.

Similar calculations for other altitudes and speeds have been completed.

2. Trailblazer II Vehicles

Under an extension to Subcontract No. 226, calculations by GASL of the shock layer, near wake, and far wake for a vehicle shape appropriate to present plans for Trailblazer II vehicles (Fig. II-13) are in progress for the following flight conditions:

Altitude (ft)	Speed (ft/sec)
80,000	9,150
100,000	15,875
150,000	21,600
200,000	22,475
250,000	22,550

Equilibrium flow calculations have been completed for the shock layer flow for 80,000 and 100,000 ft, and frozen flow for 100,000 ft. Attempts to run frozen-flow calculations for the other cases have run into some difficulties. Once these are overcome, some estimates of non-equilibrium effects can be made by a perturbation procedure on which GASL has done considerable work.

Boundary layer calculations have been initiated for those cases for which flow field calculations exist. Calculations of the near wake have also been started for these flight conditions.

Fig. II-9. Flow field details.
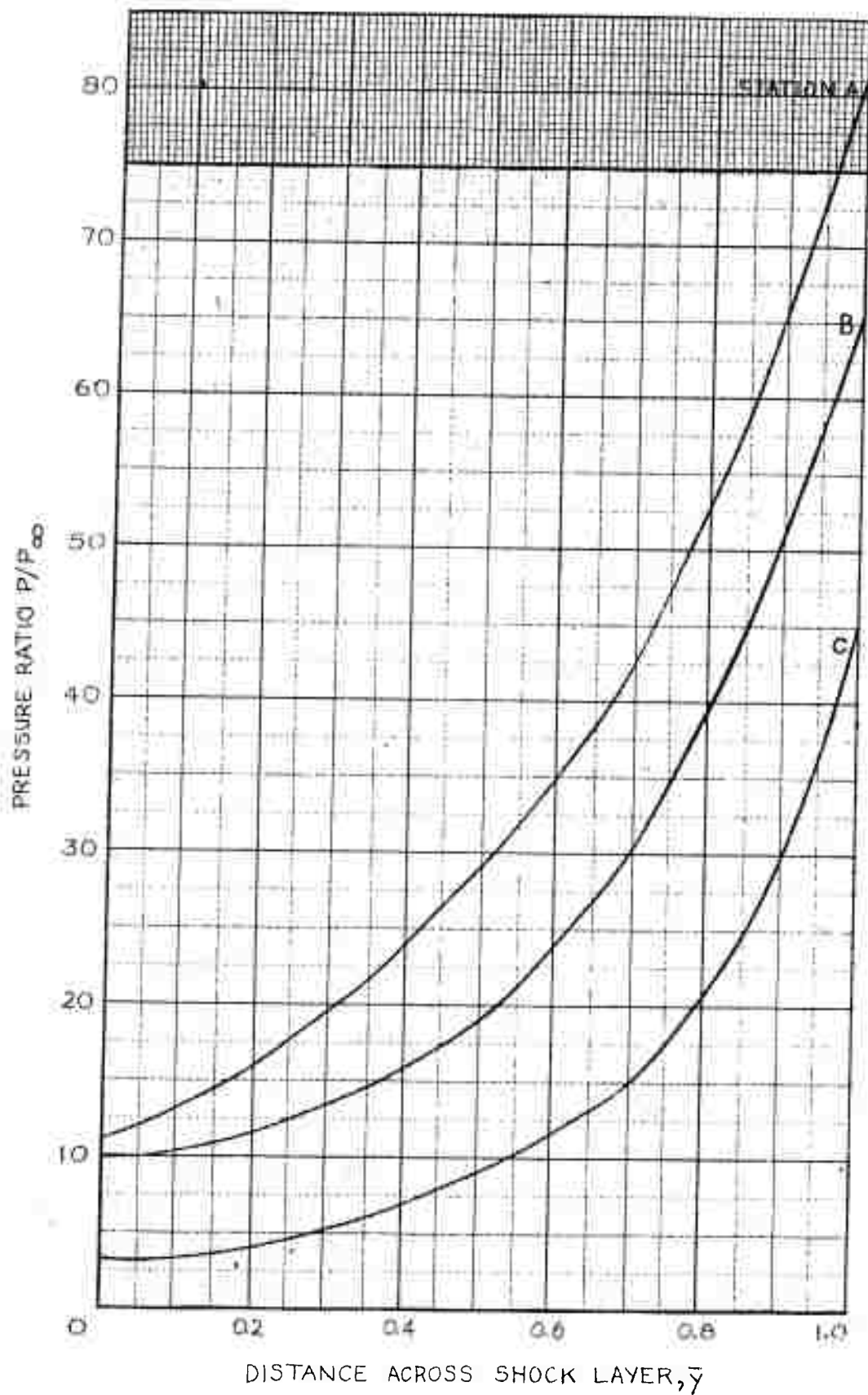
Fig. II-10(a). Pressure ratio across shock layer at stations
A, B and C of Fig. II-9. Altitude 150,000 feet.
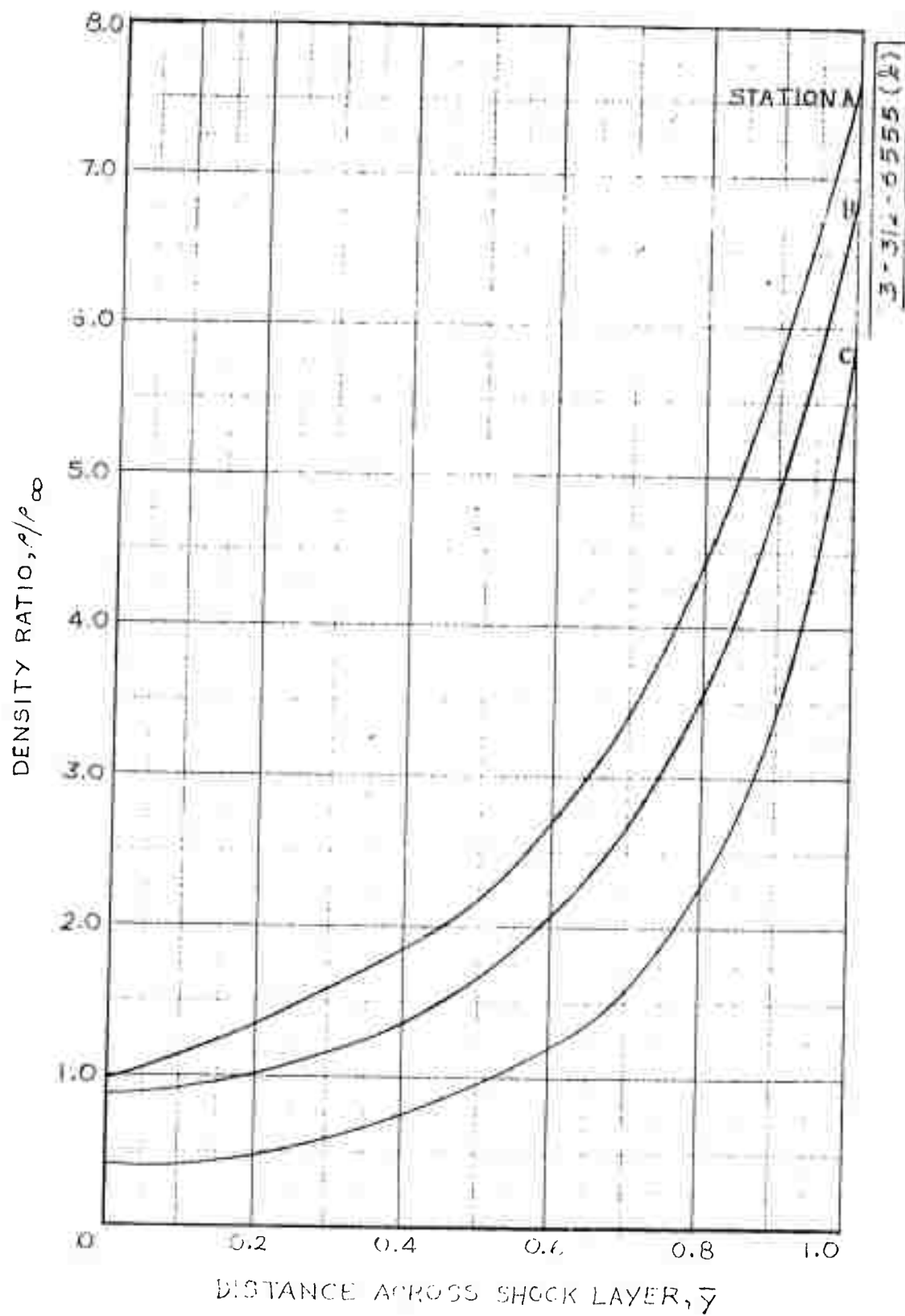
Fig. II-10(b). Density ratio across shock layer at stations
A, B and C of Fig. II-9. Altitude 150,000 feet.
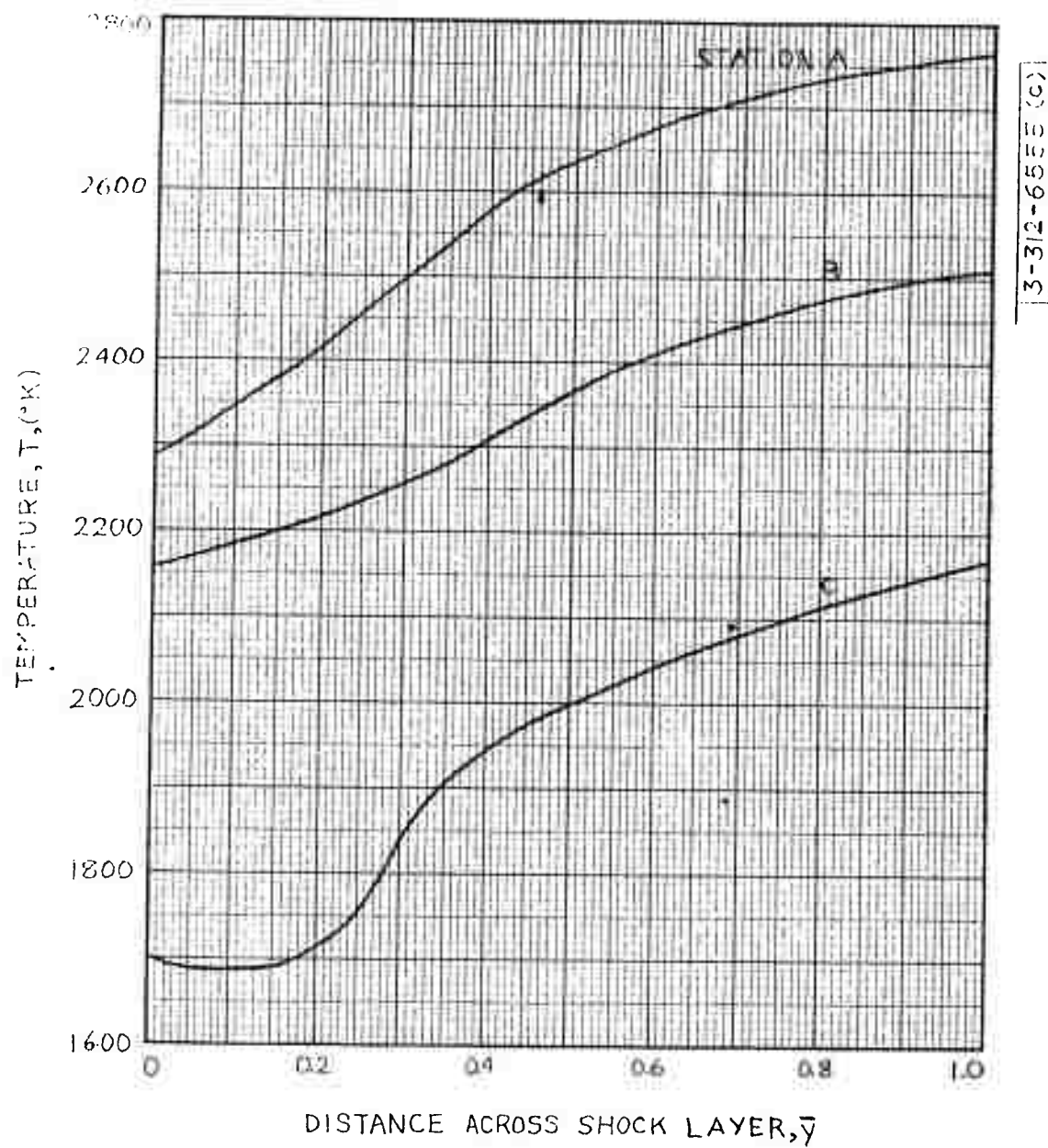
Fig. II-10(c). Temperature distribution across shock layer at stations A, B and C of Fig. II-9. Altitude 150,000 feet.
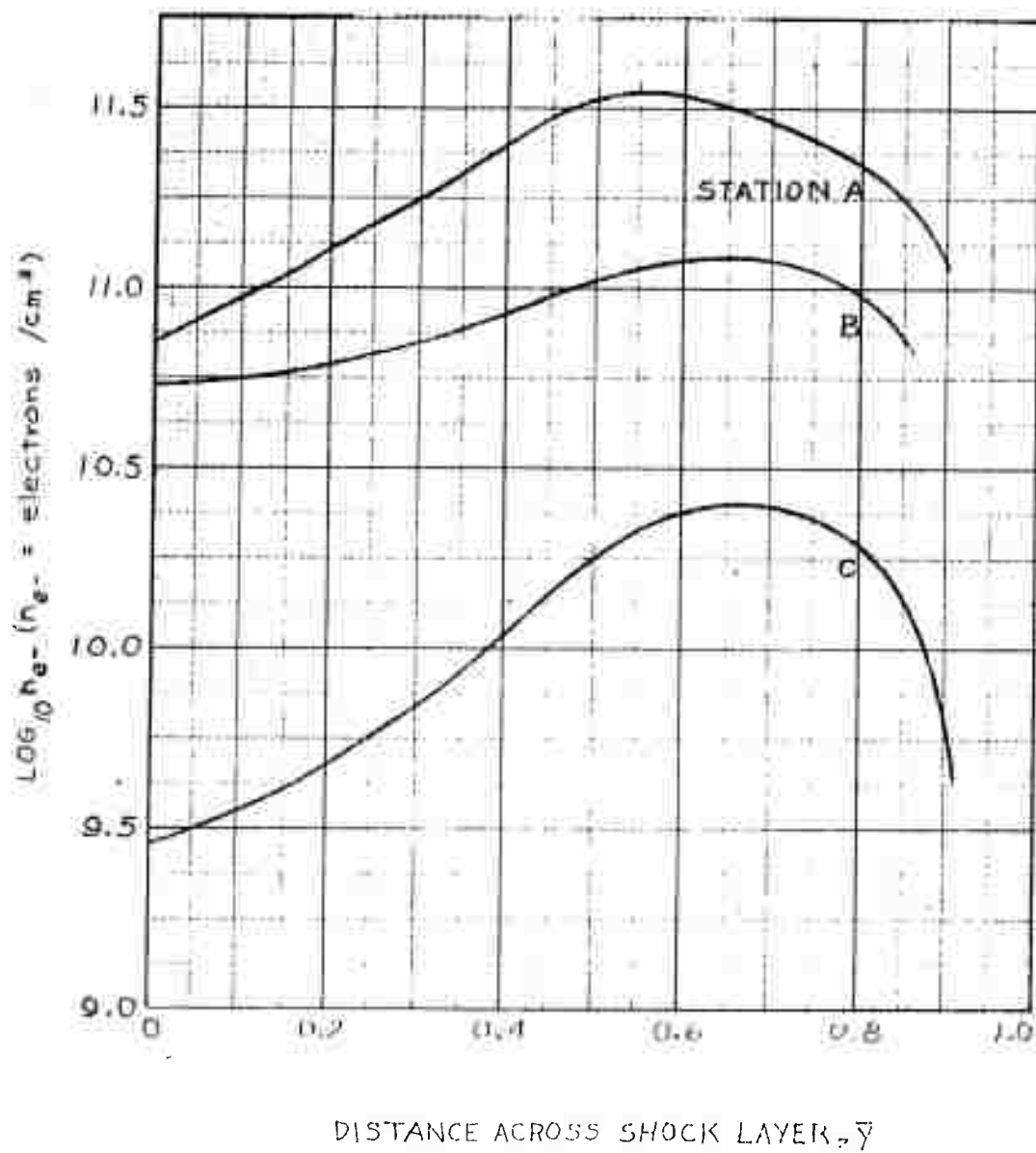
Fig. II-10(d). Electron-density distribution across shock layer
at stations A, B and C of Fig. II-9. Altitude 150,000 feet.
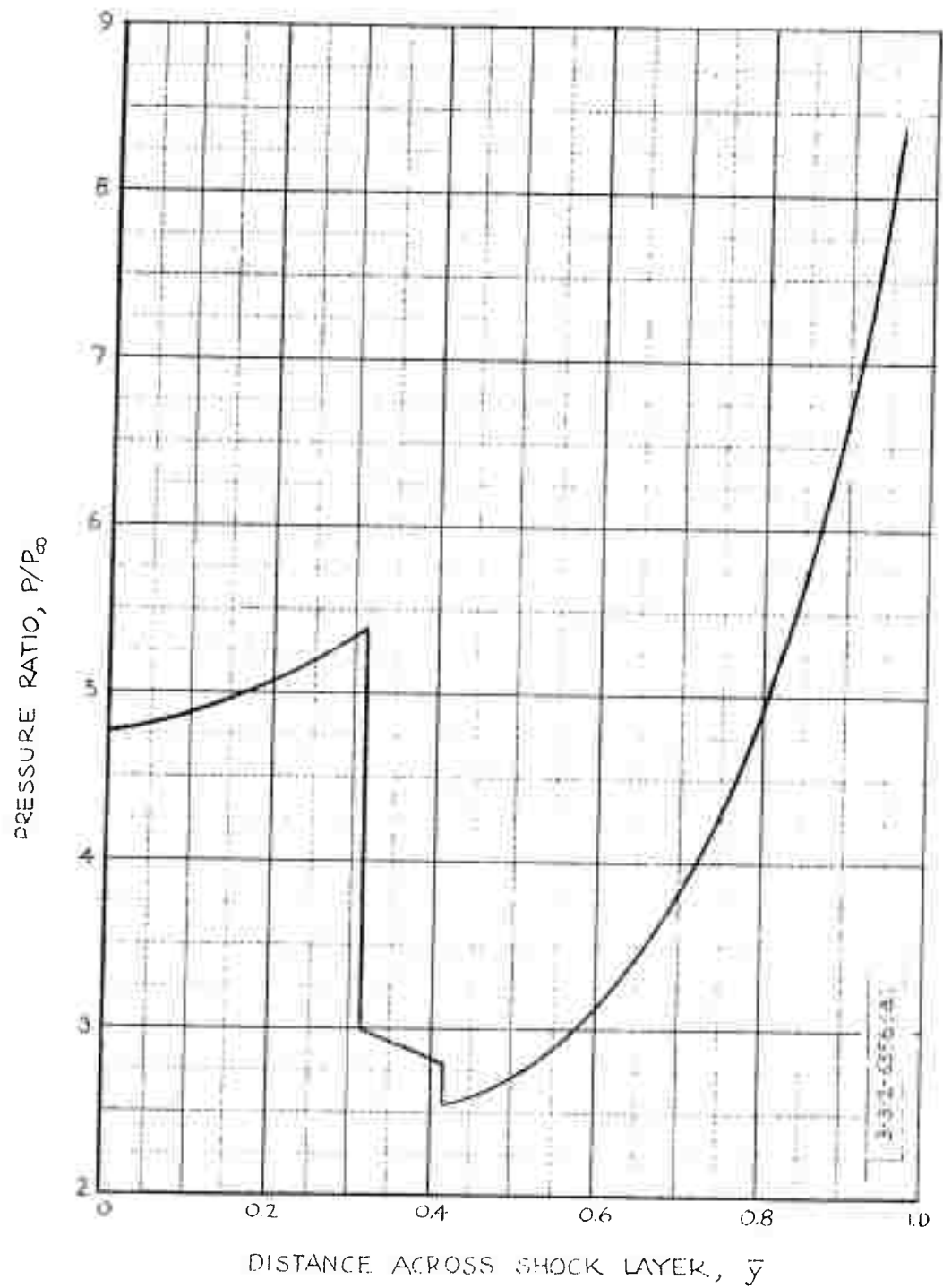
Fig. II-11(a). Pressure ratio across shock layer. $x/r_n = 9$.
Altitude 150,000 feet.
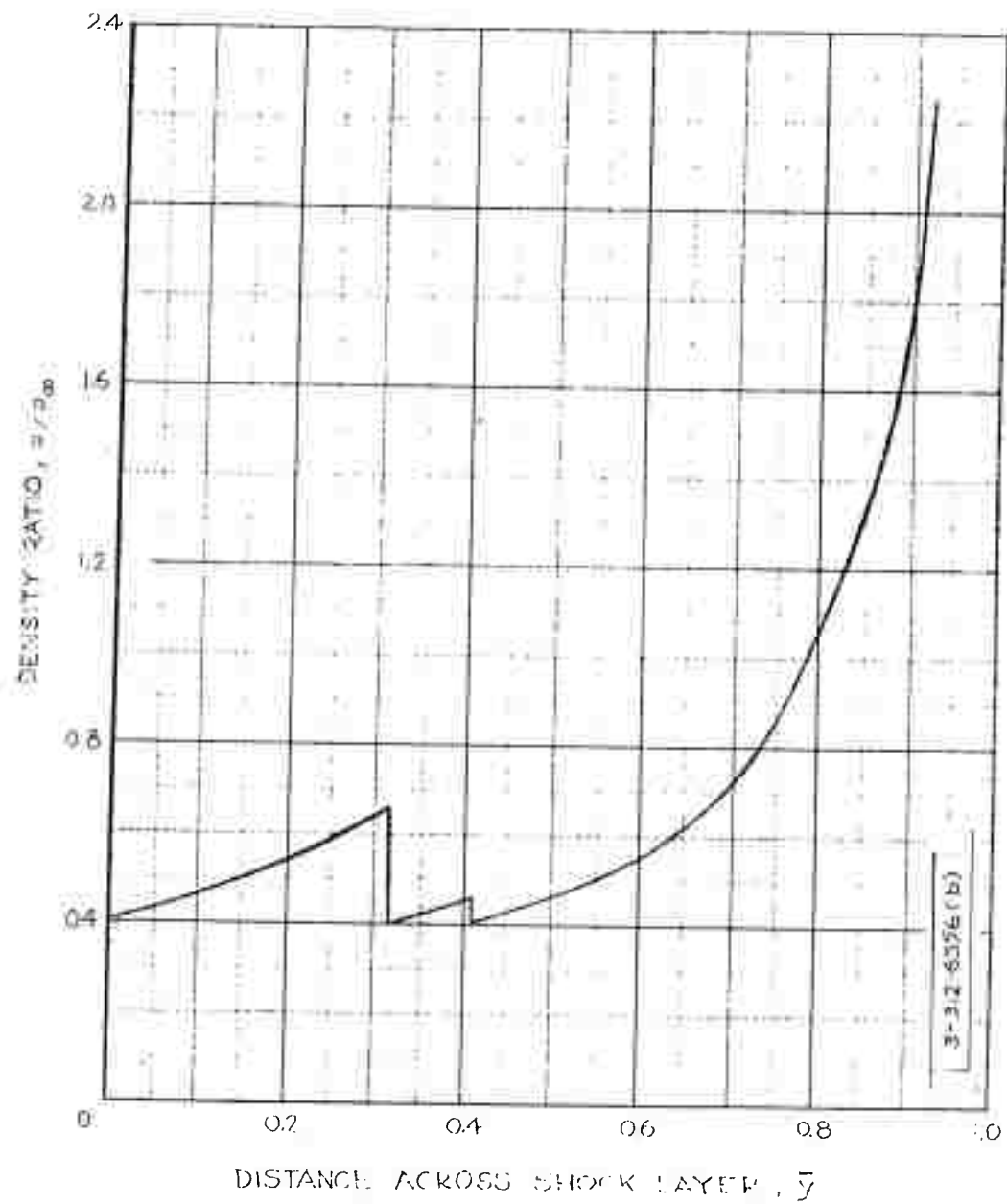
Fig. II-11(b). Density ratio across shock layer. $x/r_n = 9$.
Altitude 150,000 feet.
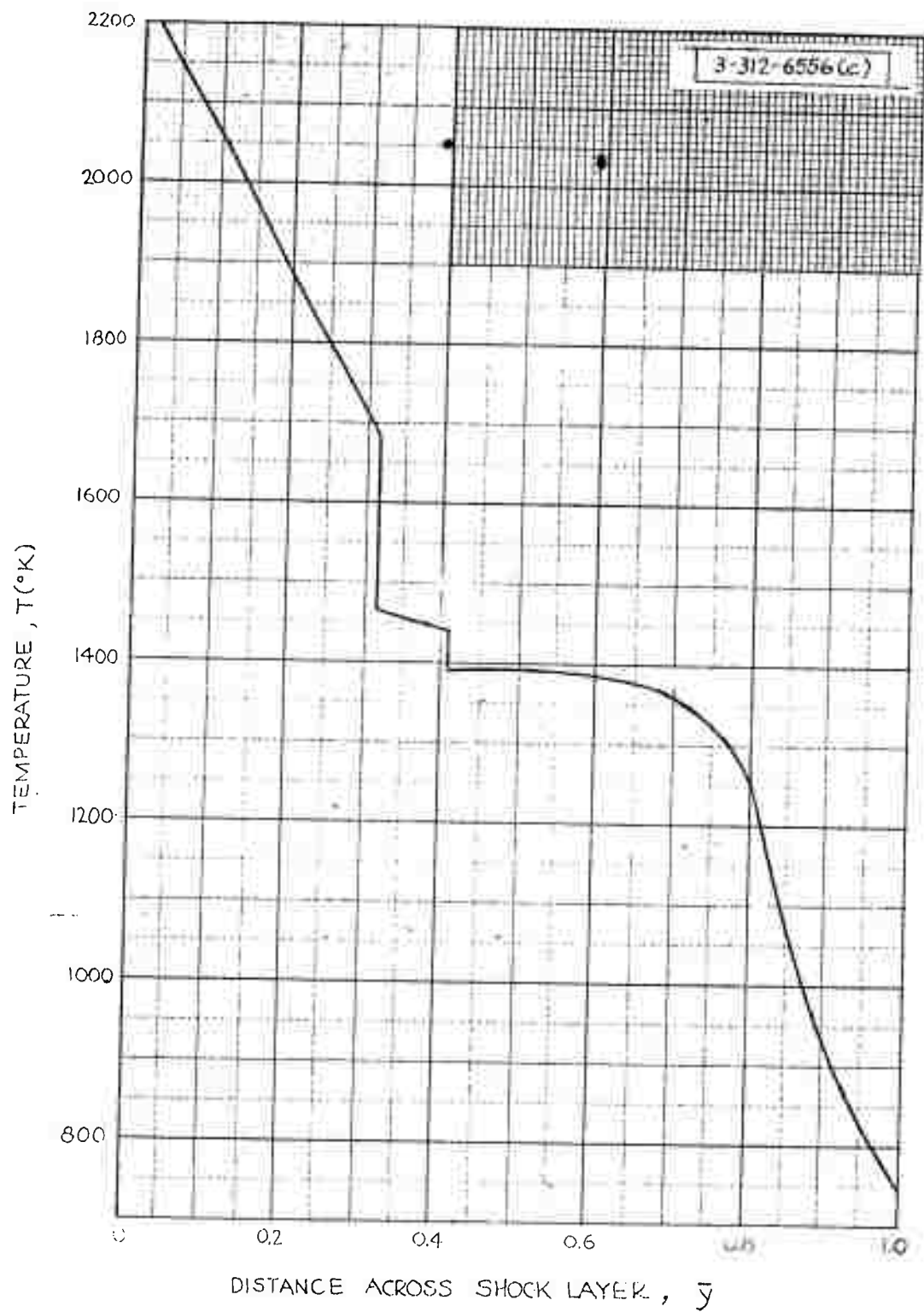
Fig. II-11(c). Temperature distribution across shock layer. $x/r_n = 9$.
Altitude 150,000 feet.

II-21
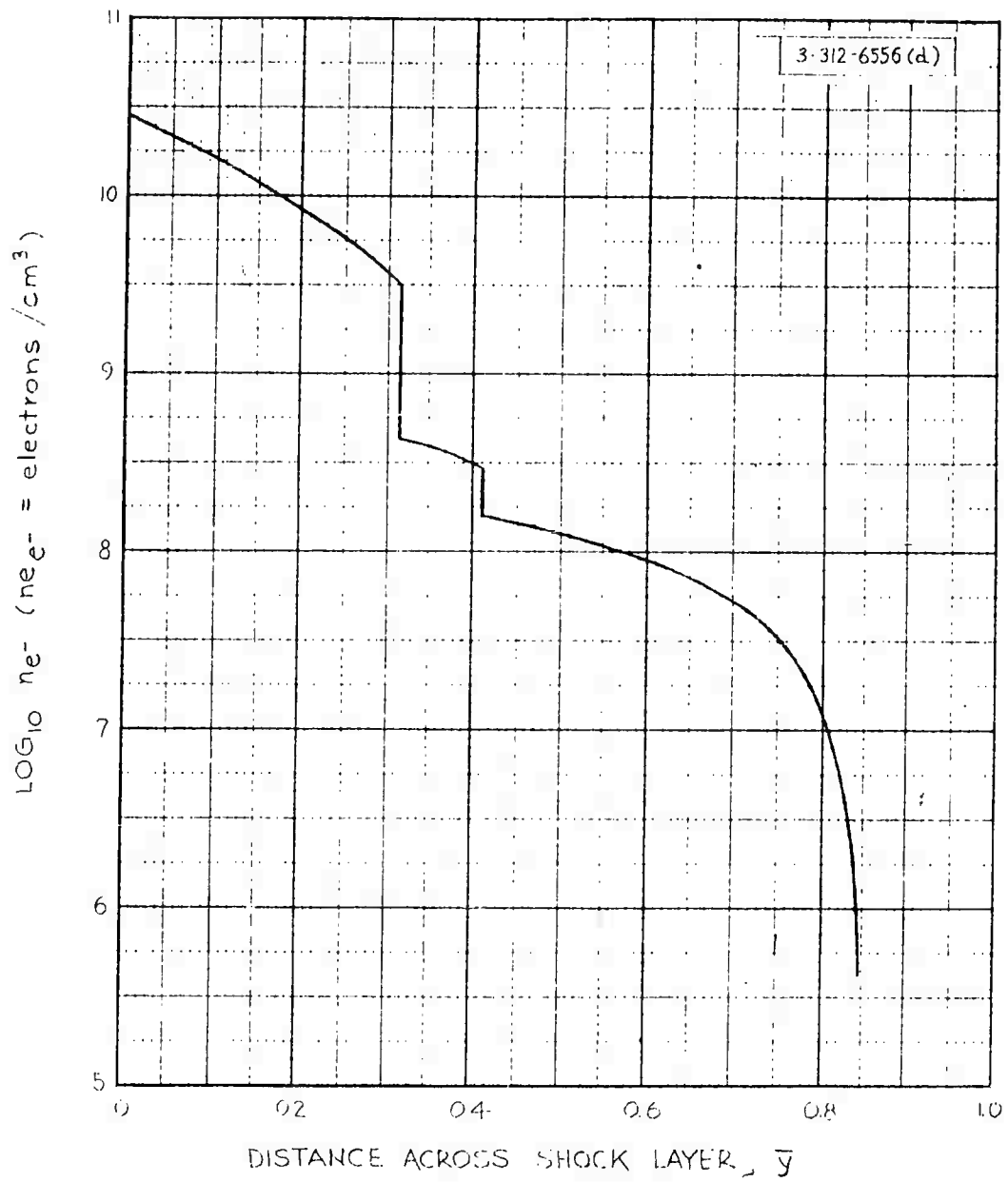
Fig. II-11(d). Electron-density distribution across shock layer. $x/r_n = 9$. Altitude 150,000 feet.
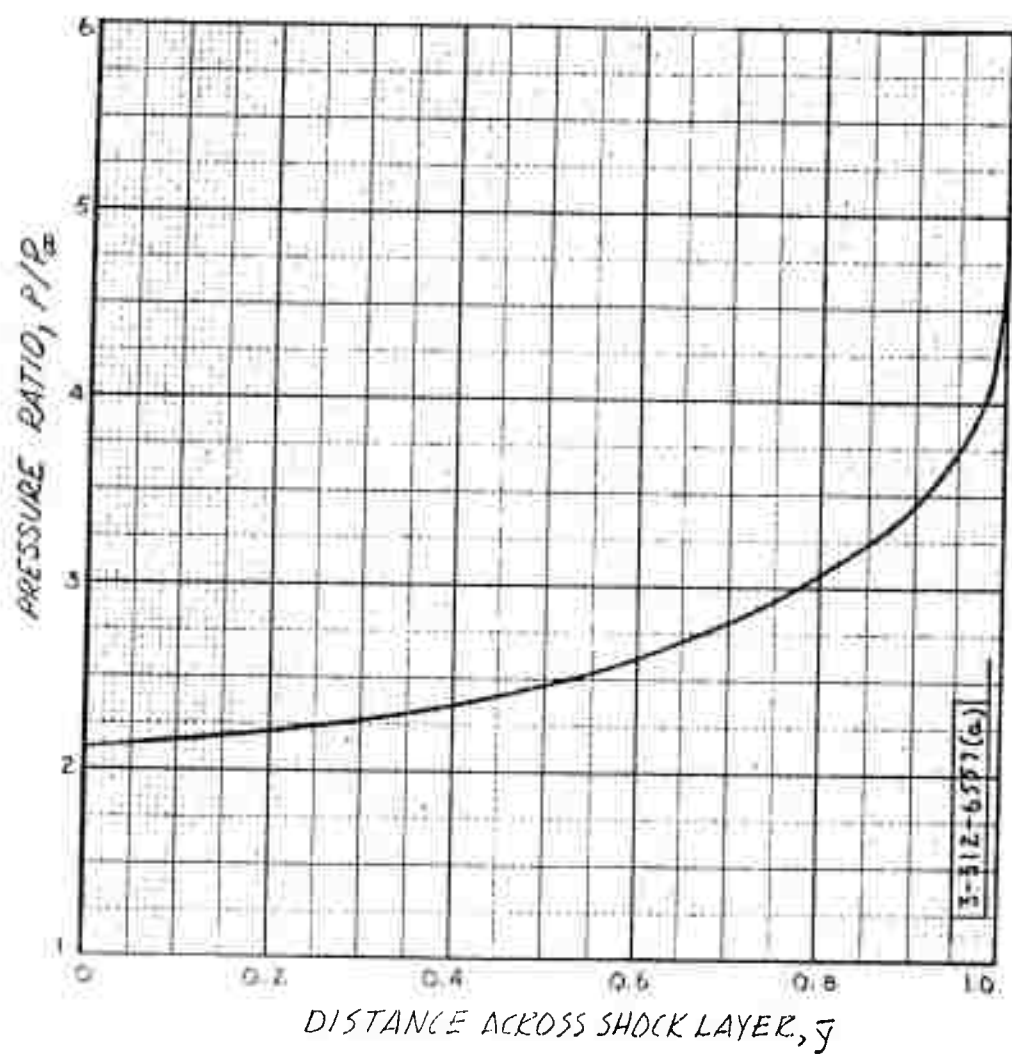
Fig. II-12(a). Pressure ratio across shock layer. $x/r_n = 23$. Altitude 150,000 feet.
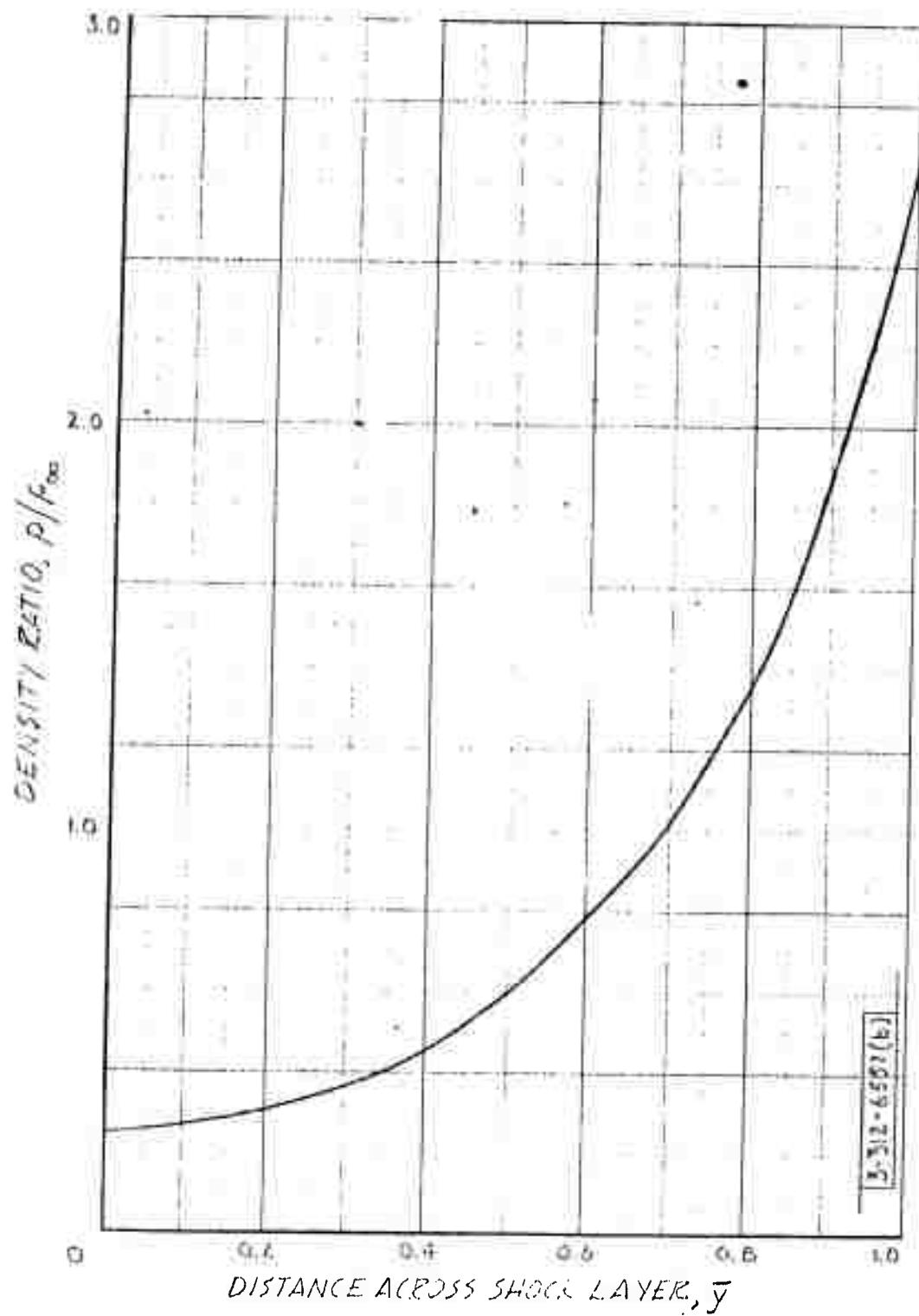
Fig. II-12(b). Density ratio across shock layer. $x/r_n = 23$. Altitude 150,000 feet.
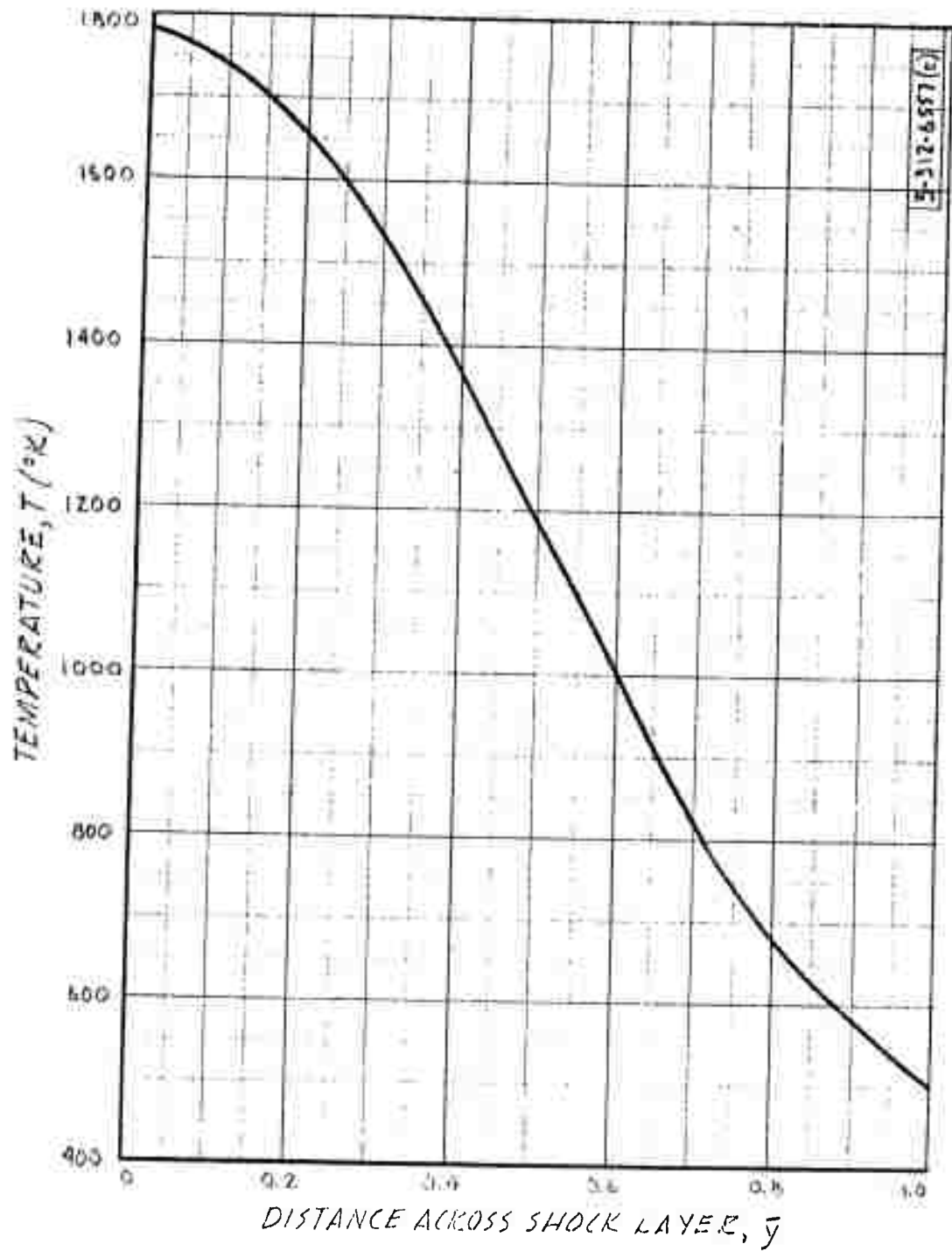
Fig. II-12(c). Temperature distribution across shock layer. $x/r_n = 23$.
Altitude 150,000 feet.
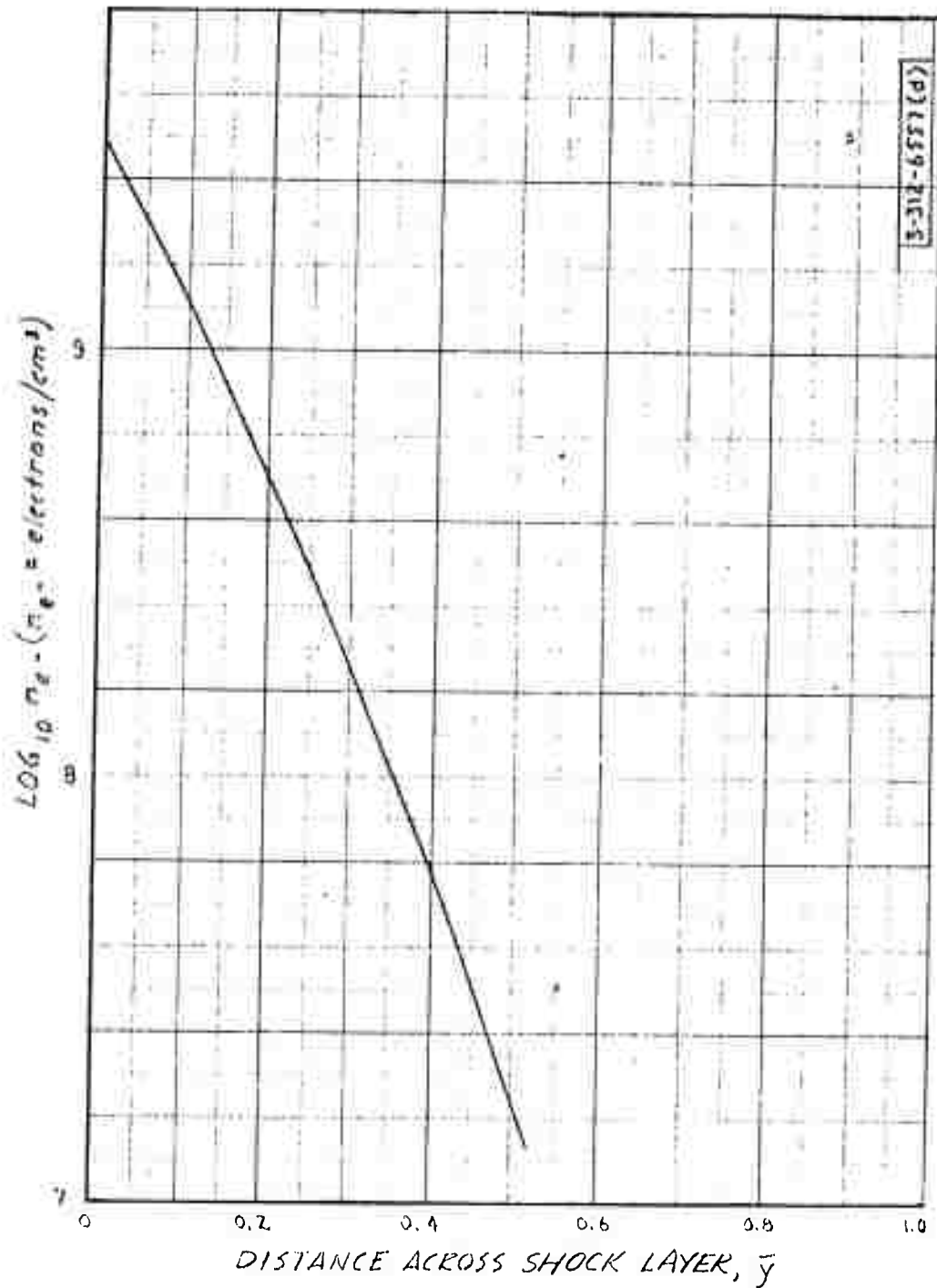
Fig. II-12(d). Electron-density distribution across shock layer. x/r_n = 23.
Altitude 150,000 feet.
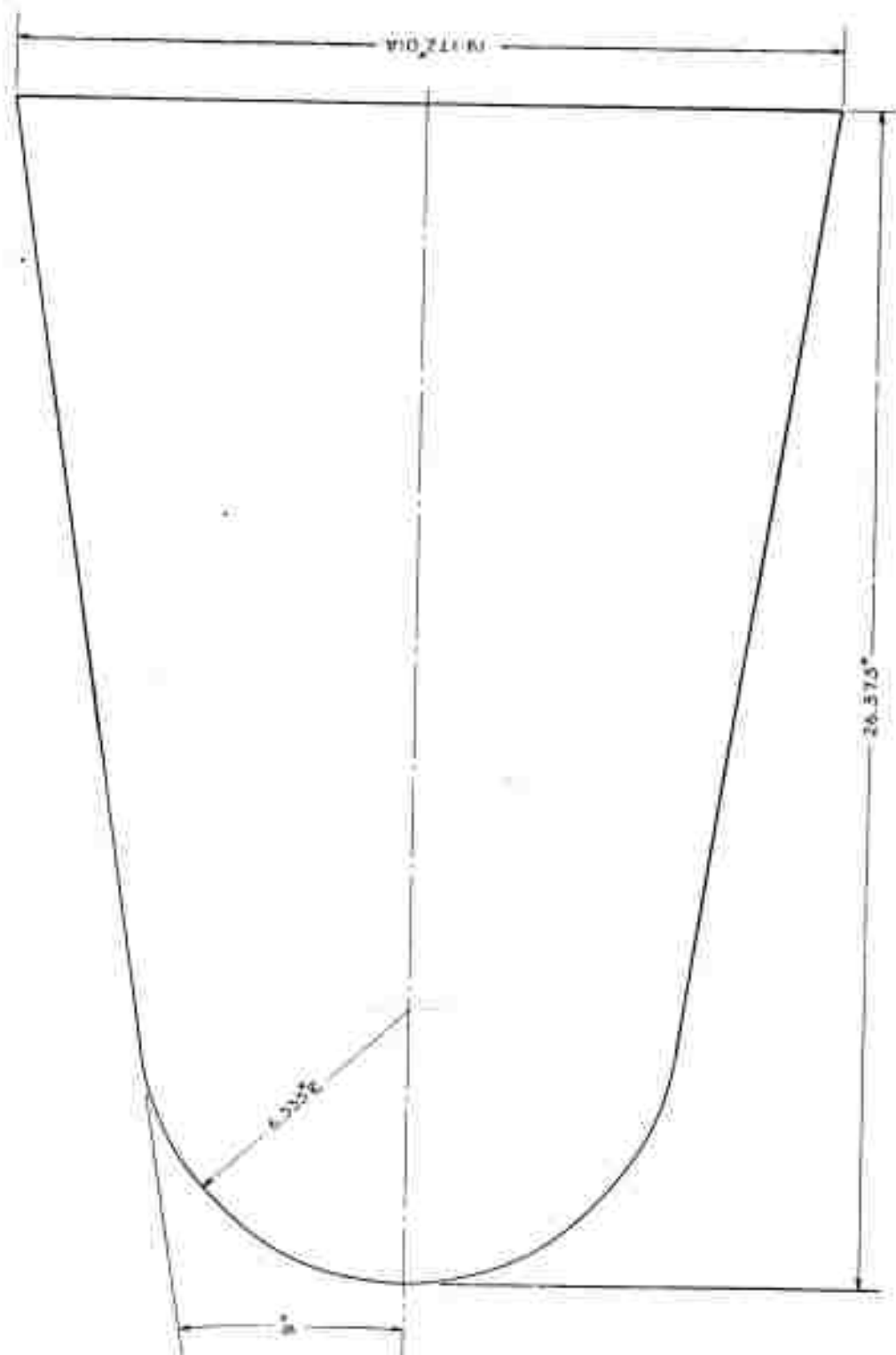
Fig. II-13. Vehicle shape for GASL Trailblazer II flow calculations.

II-27

REFERENCES

1. "Reentry Physics Program Semiannual Technical Summary Report to the Advanced Research Projects Agency," Lincoln Laboratory, M.I.T. (31 December 1960), p. 10, ASTIA 252669.

2. S. Feldman, "Trails of Axi-Symmetric Hypersonic Blunt Bodies Flying through the Atmosphere," Research Report No. 82, AVCO-Everett (December 1959).

3. P. Lykoudis, "Theory of Ionized Trails for Bodies at Hypersonic Speeds," Research Memorandum RM-2682, RAND Corporation (May 1961).

4. R. Vaglio-Laurin, Final Report, Part X, "On the Determination of Real Gas Flows About Blunt-Nosed Bodies," Technical Report No. 104, General Applied Science Laboratories, Inc. (July 1959).

5. S.C. Lin, "Cylindrical Shock Waves Produced by Instantaneous Energy Release," J. Appl. Phys. $\underline{25}$, 54 (1954).

6. B. Kivel and K. Bailey, "Tables of Radiation from High Temperature Air," Research Report No. 21, AVCO-Everett (December 1957).

7. "Reentry Physics Program Semiannual Technical Summary Report to the Advanced Research Projects Agency," Lincoln Laboratory, M.I.T. (30 June 1959), ASTIA 228431, H-125.

8. E. Kennedy and A. Fields, "The Numerical Calculation of the Flow Field Around a Reentry Body," Technical Report No. 231, General Applied Science Laboratories, Inc. (April 1961), prepared for Lincoln Laboratory under Subcontract No. 226.

9. M.H. Bloom and M.H. Steiger, "Inviscid Flow with Nonequilibrium Molecular Dissociation for Pressure Distributions Encountered in Hypersonic Flight," Journal of the Aero/Space Sciences $\underline{27}$, No. 11 (November 1960).

III. ELECTRONIC PROPERTIES OF REENTRY PLASMAS*

A. INTRODUCTION

Section III describes work performed by Group 35 directed toward a basic understanding of the generation, distribution, and decay of free electrons in the wakes of hypervelocity bodies. The principal laboratory tool is the in-house hypervelocity range, employing a light-gas gun to project pellets at reentry speeds through a tank simulating upper-atmospheric conditions. The range is instrumented with a resonant-cavity electron-density probe, a CW Doppler radar operating in waveguide, and shadowgraph and schlieren still and motion-picture photography. A larger-caliber, lower-speed, powder-driven gun is also employed for studies of aerodynamic turbulence and impact studies.

The first data on light-gas-gun shots were reported in the 31 December 1960 Semiannual Report. Further data from the cavity and Doppler experiments are reported here. The following papers presented at the Colorado Springs AMRAC meeting, 8-10 May 1961, also contain results from this work:

> "Doppler Measurement of the Ionized Wakes of Hypervelocity Pellets," R. E. Richardson and M. A. Herlin

> "Electron Density Measurements in the Wakes of Hypervelocity Pellets," M. Labitt and M. A. Herlin

A third paper was also presented at this meeting

> "Hypervelocity Rod Impact into Aluminum at Normal and Yawed Incidence," W. G Clay, R E Slattery and E. W. Pike

Because this last work does not directly concern reentry physics, reference is made to the Symposium Proceedings rather than summarizing the results here.

The experimental methods have been further studied and improved and their range of validity more clearly defined. A summary of these findings for the cavity method is given here, and a detailed report is in preparation.
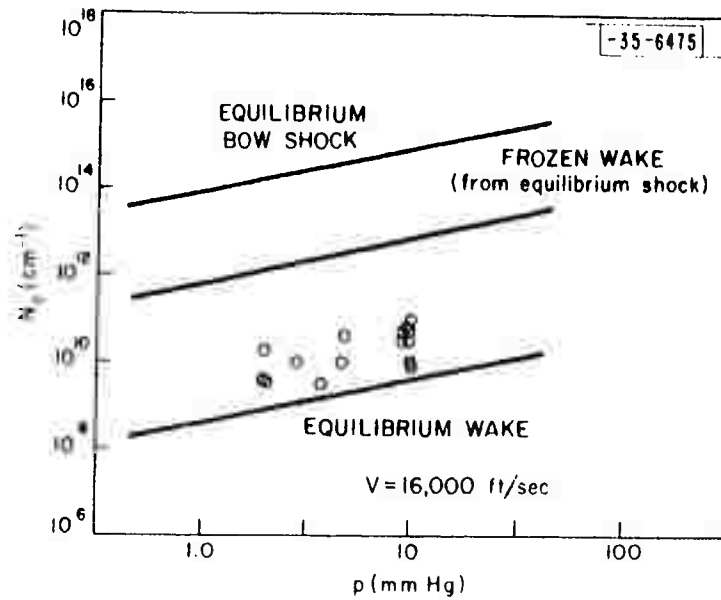
Fig. III-1. Initial electron density as a function of ambient air pressure. Theoretical curves are for 16,000 ft/sec. Experimental points (circles) are for a range of velocities from 14,000 to 18,000 ft/sec.

M. Labitt presented a paper with H. Pascalar of Group 312 on "R-F Instrumentation of Hypervelocity Ranges" at a Symposium on Hypervelocity Range Instrumentation held at CARDE, 29-30 June 1961. This paper may be read in the Symposium Proceedings when it becomes available.

Photography of the turbulent wakes of pellets has been extended downward in pressure to the point where the laminar-turbulent transition has been observed directly. This transition and the growth of the wake diameter with time after passage of the pellet are described here. Motion picture films have also been made with a Fastax camera. These show clearly the growth of the wake, the slowing of the forward component of velocity in the wake, the persistence of identity and evolution of individual eddies, and the growth of "feathers" and other fine structure of interest in the electromagnetic scattering problem. Some of this work has been submitted to the Journal of the Physics of Fluids under the title:

> "Width of the Turbulent Trail Behind a Hypervelocity Sphere,"
> R. E. Slattery and W. G. Clay.

Also, a presentation of this work was made at an informal meeting on wake aerodynamics held at the RAND Corporation, 22-23 June 1961. No written proceedings are planned for this meeting.

B. ELECTRON-DENSITY MEASUREMENTS IN THE WAKES OF HYPERVELOCITY PELLETS

Electron-density measurements using the resonant-cavity technique have been continued. The pressure range which can be measured using the original equipment appears to be limited on the low end at about 2 mm Hg of air pressure, due to decreasing ionization densities, and on the high end by detuning of the cavity by the shock waves attending the pellet at about 15 mm Hg. The high end is being extended with the aid of a more rugged cavity. Efforts to improve the sensitivity of the equipment will extend the lower limit of the pressure range. The data at all pressures are improved in accuracy by these changes.

Although the pressure range to date is limited, a pressure dependence of initial electron density can be estimated. The points on the curve of Fig. III-1 summarize the pressure variations covered thus far. Within this range, the
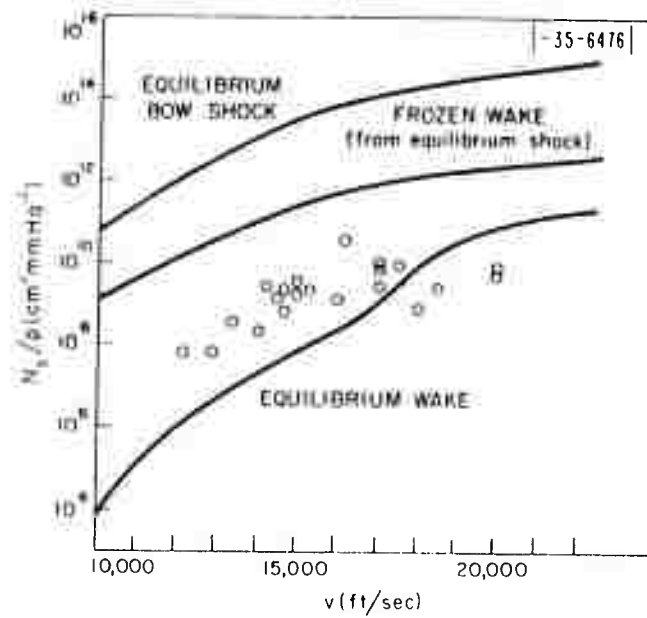
Fig. III-2. Initial electron density per unit ambient pressure as a function of pellet velocity.

pressure dependence is a simple proportionality. A few shots have been taken at lower pressure (approximately 0.5 mm Hg), but some difficulty with trigger timing in addition to equipment sensitivity was experienced and they are not reproduced here. The indication is, however, that a superproportional decrease sets in at about this range. This behavior is consistent with the increasing ion-ization times required as the pressure is reduced.

The pressure proportionality observed in Fig. III-1 suggests the presentation of all the data in reduced form as shown in Fig. III-2. In this figure, the electron density per unit of pressure is plotted as a function of pellet velocity. The points represent all the shots for which satisfactory data were obtained to date. In some instances, the pellets were poorly aimed and impacted with objects only slightly down range of the cavity. The resulting backsplatter generated ionization in the cavity which masked the decay curve. However, the initial electron densities could be read from the oscilloscope traces in spite of the loss of data at later times.

The frozen and equilibrium electron-density curves on Fig. III-2 were de-scribed in the 31 December 1960 Semiannual Report. The equilibrium wake curve has been recomputed with greater care, and lies slightly higher at the higher-velocity end than that shown in the previous report. Consolidating data at several pressures on one curve, more experimental points are available at the high end. It seems fairly well established that the experimental points lie below the equilibrium curve at the high end, in contrast to the frozen-in ioniza-tion indicated at the lower end.

Several electron-density decay curves are shown in Fig. III-3. These curves continue to show the behavior noted in the previous report that the decay time is pressure independent within the pressure range covered. The decay curves, as presented on semilogarithmic scales, are relatively linear. Electron attach-ment would provide linear cleanup curves but would show a pressure dependence.[1] Recombination with a constant electron-ion recombination coefficient is ruled out by the linearity of the curves. It is likely that electron attachment is sup-pressed by the high wake temperatures, and that cleanup is caused by recom-bination with a small coefficient at short times, and increasing with time. The
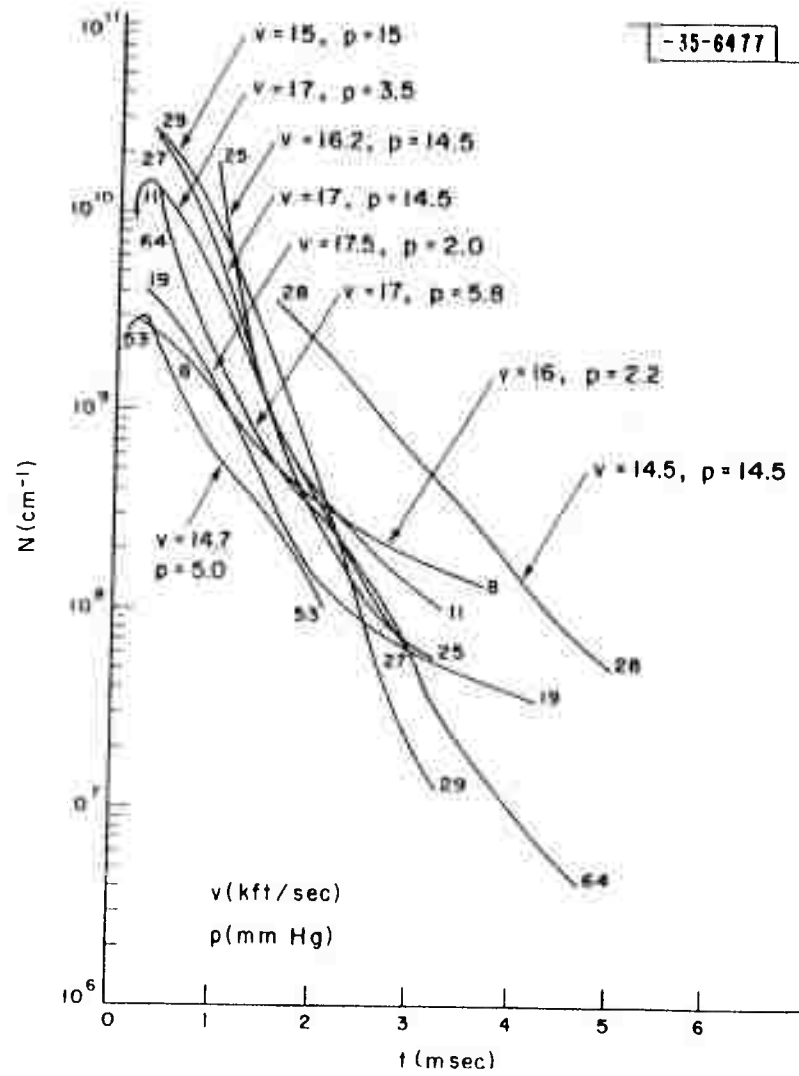
Fig. III-3. Wake electron density decay profiles.

expected falling wake temperature would produce a falling recombination coefficient, as required. A wake temperature profile can be computed from an assumed recombination coefficient dependence on temperature, such as $\alpha_r = 3 \times 10^{-3} T^{-1.5} cm^3/sec$ (Ref. 2). A typical electron-density profile is given by $n_e = n_o \exp[-t/\tau]$, where $n_o \simeq 10^{11} cm^{-3}$, and $\tau \simeq 4.3 \times 10^{-4}$ sec. The corresponding temperature profile is then $T = T_o \exp[-t/1.5\tau]$, where $T_o = (3 \times 10^{-3} n_o \tau)^{2/3} = 2600°K$. The temperature time-constant $1.5\tau = 6.5 \times 10^{-4}$ sec is about four times lower than the laminar-flow thermal-conduction time.[3]

The electron collision frequencies agree in order of magnitude with values expected from known collision cross sections.[4] Collision frequencies should be approximately independent of gas temperature so that wake temperature information cannot be obtained from the collision frequency values.

C. RANGE OF VALIDITY OF THE CAVITY METHOD OF ELECTRON DENSITY MEASUREMENT

The cavity electron-density probe has been subjected to a continuing study to determine its range of validity and to improve the stability and reliability of the electronic equipment. As noted previously, a heavier cavity has been built to reduce errors caused by dimensional changes resulting from shock waves generated by the pellet. Delayed jolts from the gun itself have never been a problem since the proper shock mounting of the cavity was instituted. On those shots where no ionization was observed due to poor aim or low pressure, the oscilloscope traces showed no perceptible deviation from such external sources. This test checks not only the cavity itself but also the oscillators and other pieces of equipment.

An inverse requirement to that of non-perturbation of the cavity by the flow field is that the flow field should not be disturbed by the cavity. The cutoff tubes must be made large enough in diameter to offer a minimum interference with the flow patterns induced by the pellet flight. Since the flow problem is part of the subject under investigation, it is difficult to estimate the extent of this interference in advance. Feldman[5] has given results of computations of flow fields for a similar case which show that the wake reaches sonic values at a distance of approximately 50 pellet radii behind the pellet. Beyond this

region, the shock is very weak and the velocity profile is stabilized. The shock is less than 10 pellet radii from the axis of flight, and the velocity profile decays to ambient in about 5 pellet radii from the axis. Our experiments have employed $\frac{1}{4}$-inch diameter pellets, and 6-inch diameter cutoff tubes, placing the tubes at a distance of 24 pellet radii from the axis. The interaction of the flow with the cavity should therefore be small.

The range of applicability of the cavity method has been investigated with respect to four effects: (1) the electron-density range for which perturbation analysis of the cavity is valid, (2) end effects, (3) surface-wave coupling of the cavity through the portals to the outside region in the presence of an ionized wake, and (4) the effect of RF heating of the electrons by the probe field and its limitation on signal-to-noise ratio. The details of this analysis are given in a forthcoming report on the cavity method. The results are summarized below.

1. Breakdown of Perturbation Theory

The analysis of the cavity fields and their interaction with the wake electrons is carried out under the assumption that the plasma constitutes a small perturbation on the fields. This assumption may be tested from two points of view. First, the shift of resonant frequency must be a small fraction of the resonant frequency itself, and the plasma Q must be large in comparison with unity. These statements amount to the single statement that

$$\left| \frac{1}{Q_e} + j \left(\frac{\omega_o}{\omega'_o} - \frac{\omega'_o}{\omega_o} \right) \right| \ll 1 \quad ,$$

where Q_e is the plasma Q, ω_o is the undisturbed resonant frequency of the cavity, and ω'_o is that in the presence of plasma. In terms of electron density and collision frequency, this condition reduces to

$$N \ll 1.4 \times 10^{12} \sqrt{1 + \nu_m^2/\omega^2} \text{ electrons/cm} \quad ,$$

where N is the electron line density, ν_m is the electron-molecule collision frequency, and ω is the cavity radian frequency. Confining electron-density

values to be measured to less than 10^{12}cm^{-1} therefore guarantees that the over-all cavity perturbation is not excessive, and that the cavity acts as a high-energy storage device.

The second point of view concerns the local perturbation rather than the over-all perturbation of the cavity as a whole. The cavity mode is chosen to provide an electric field parallel to the axis of the wake. A large gradient of effective dielectric coefficient of the medium does not therefore imply a large gradient of electric field. The field gradient is determined by the propagation constant $\omega\sqrt{\kappa}/c$, where κ is the dielectric coefficient of the plasma and c is the velocity of light. For small perturbation, we therefore require that

$$\left| \frac{\omega\sqrt{\kappa}}{c} \rho_e \right| \ll 1 \quad,$$

which reduces to

$$N \ll 0.89 \times 10^{12} \sqrt{1 + \nu_m^2/\omega^2} \text{ electrons/cm} \quad,$$

which is substantially the same as the previous result. The upper limit of 10^{12} electrons/cm therefore marks the breakdown of perturbation theory from either the over-all or local perturbation points of view.

It is noted that these results are independent of frequency. The density of electrons required to produce a significant change of dielectric coefficient compared to unity at the cavity frequency of 450 Mcps is only $2 \times 10^9 \text{cm}^{-3}$ (the density where 450 Mcps is equal to the "plasma frequency"). However, the field penetration is complete to densities several orders of magnitude higher than this in the present experiments due to the small-diameter trails. Perturbation theory therefore holds to the higher densities.

2. End Effects

The cavity analysis performed neglecting the effect of the cutoff tubes must be modified to include the fringing of the electric fields at the ends where they leave the plasma and terminate on charges at or near the corners where the cutoff tubes join the cavity end plates. This effect may be shown

to amount to a series capacitance tying the plasma impedance to the cavity end terminals in the equivalent circuit. The impedance of this series capacitance is required to be small compared with the plasma impedance. The value of the capacitance has been estimated two ways. First, the short length of coaxial capacitance corresponding to the length of the fringing field plus the depth of penetration of the field into the cutoff tubes can be estimated from electrostatics. Second, the plasma may be approximated by an oblate spheroid of similar dimensions and the depolarizing field of the spheroid attributed to an equivalent series capacitance. Either approach yields a result similar to that of the small perturbation limit, except that it is multiplied by the square of the ratio of the cavity length to its diameter. This ratio is of the order of unity for the present design, so that again 10^{12} electrons/cm is the upper limit of the measurement.

3. Slow-Wave Coupling

When the dielectric coefficient of the plasma drops below -1, a surface-type slow wave begins to propagate in the cutoff tubes. The upper limit of electron density for which the characteristic impedance of the transmission line thus generated is small in comparison with the plasma impedance has been computed. The result is again of the order of 10^{12} electrons/cm multiplied by the square of the ratio of the length to the diameter of the cavity.

4. Electron Heating and Signal-to-Noise Ratio

The above three types of limitation on the cavity method all result from disturbance of the cavity fields by the plasma. The inverse disturbance — that of the plasma by the cavity fields — must also be considered. If such a disturbance did not take place, there would be no limit to the signal-to-noise ratio obtainable. Any desired accuracy could be obtained with the use of sufficiently high signal-generator power.

If Δu is the maximum permissible electron energy increment due to the application of an electric field E, the relation between the two may be shown to be

$$E = \sqrt{\frac{2mg\,\Delta u(\nu_m^2 + \omega^2)}{e^2}} \quad,$$

where m and e are the electron mass and charge, and g is the fractional energy loss on collision between an electron and a gas molecule. Cavity fields have been employed sufficiently low to confine Δu to less than 30°K, measured in temperature units. It has been shown that the minimum electron density measurable with this upper limit of signal-generator power for electrons in air and for a detector noise temperature of 600°K is of the order of a few thousand electrons/cm. The measurement system has not been developed to exploit this degree of sensitivity. The limitations thus far lie in equipment stability. The techniques are being reviewed and improved to extend the sensitivity to smaller electron densities.

D. DOPPLER MEASUREMENT OF WAKE VELOCITY AND ELECTROMAGNETIC REFLECTIVITY

The details of the apparatus for this experiment were described in the 31 December 1960 Semiannual Report. Improvements made since that time include an increase in the length of the waveguide and a better match of the terminations. Also, the calibration of the apparatus is now more accurate.

Table III-1 gives a summary of the successful shots to date. The $\frac{1}{2}$-inch gun uses .50-calibre cartridges loaded with appropriate pellets and powder. It is quite reliable and has a rate of fire limited only by setup time of experiments using the pellets, but at its low velocities there is little shock-induced ionization. The $\frac{1}{4}$-inch gun is the two-stage hydrogen gun with more adequate velocities, but its rate of fire is lower. An electron density of 1.8×10^{10} cm^{-3} corresponds to a plasma frequency of 1200 Mcps so that velocities considered here to be lightly ionizing are often useful to the UHF cavity experiments sharing the shots.

TABLE III-1

SUMMARY OF SHOTS

Pellet	Number of Shots	Velocity (kft/sec)	Ambient Gas
$\frac{1}{4}$-inch aluminum	14	12-18	Air
$\frac{1}{2}$-inch aluminum	3	9	Air
$\frac{1}{2}$-inch nylon	75	9	Air
$\frac{1}{2}$-inch nylon	6	9	Argon
	98		

TABLE III-2

REFLECTION FROM SMALL ALUMINUM SPHERE IN WAVEGUIDE

$$r = C_A C_W \sigma_B$$

$$\sigma_B = 4.35 \times 10^4 (a^6/\lambda_o^4) = 1.12 \times 10^{-4} \, \text{cm}^2 \rightarrow -39.5 \, \text{db}$$

$$C_W = \frac{1}{\pi} (\lambda g/xy)^2 = 2.53 \times 10^{-2} \, \text{cm}^{-2} \rightarrow -16.0 \, \text{db}$$

$$C_A = [(5 + \cos 2\alpha)/6]^2 = 6.5 \times 10^{-1} \rightarrow -1.9 \, \text{db}$$

$$\lambda_o = 25.0 \, \text{cm} \qquad \lambda_g = 38.4 \, \text{cm} \qquad x = 16.5 \, \text{cm} \qquad y = 8.25 \, \text{cm}$$

$$a = \frac{1}{8}'' = 0.318 \, \text{cm} \qquad \alpha = 49.4°$$

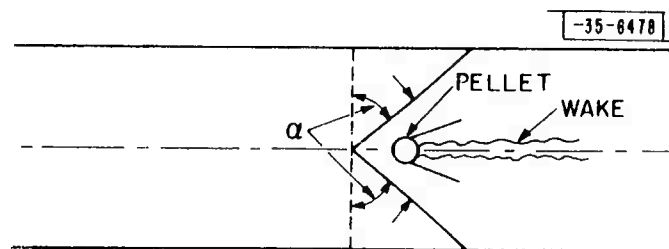| Experimental Values		Theory
−60.0 db	1/4-inch diameter aluminum sphere	−57.4 db
−42.2 db	1/2-inch diameter aluminum sphere ($2^6 \rightarrow 18$ db)	−39.4 db

-35-6478

Fig. III-4. Equivalent incident plane waves in waveguide. α is waveguide propagation angle.

Table III-2 outlines the calculation of the reflection coefficient expected from a small aluminum sphere on the axis of the waveguide without ionization. The free-space Rayleigh backscatter cross section is designated by σ_B. The free-space factor proportional to R^{-4} is replaced in waveguide by C_W. The factor C_A is a correction due to angular dependence of Rayleigh scattering. The sphere is viewed by two coherent waves at the waveguide propagation angle α (Fig. III-4) which contribute, besides backscatter, forward scatter at an angle $\pi - 2\alpha$. Free-space and waveguide wavelengths are represented by λ_o and λ_g, respectively, and x and y are the inside dimensions of the waveguide.

Experimental results given for pellets without wakes are averages over several observations in each case. If the pellet passes off-axis 1.5 inches to either side, as it is allowed to do, it experiences 3 db less resultant field than on the axis. Therefore, the measured reflectivities of bare pellets are well within experimental accuracy.

Figure III-5 shows the reflection from a $\frac{1}{4}$-inch aluminum pellet without wake. The velocity is 14,600 ft/sec, and the air pressure is 0.50 mm Hg. Time increases to the right with a horizontal scale of 0.2 millisecond per division. The upper trace is the output of the synchronous detector. Each cycle of the Doppler waveform corresponds to travel of one-half guide wavelength, or a little more than 7.5 inches. The over-all length of the equipment is 37.1 half-wavelengths. The signal grows as the pellet emerges from between the tapers of the terminations at the entrance, and likewise decays as it passes out between the exit terminations. The small pip about 5 cycles before the end is produced when the pellet passes through the tee. The bottom trace is the logarithmic output, which is more useful in measuring the size of the return, and shows that this return is 60 db down from the incident power. The gain for the upper two traces is adjusted for optimum viewing of the expected waveform for each shot, but the logarithmic gain is held constant for all shots. The flatness of the amplitude trace is the result of the improved match and better balance of the residual reflected signal than was obtained in earlier results.

Figure III-6 is for a $\frac{1}{4}$-inch aluminum pellet traveling 14,000 ft/sec in air at 14 mm Hg pressure. The return starts at -45 db, 15 db larger than for 0.50 mm Hg pressure at a similar velocity, but still quite small. The phase
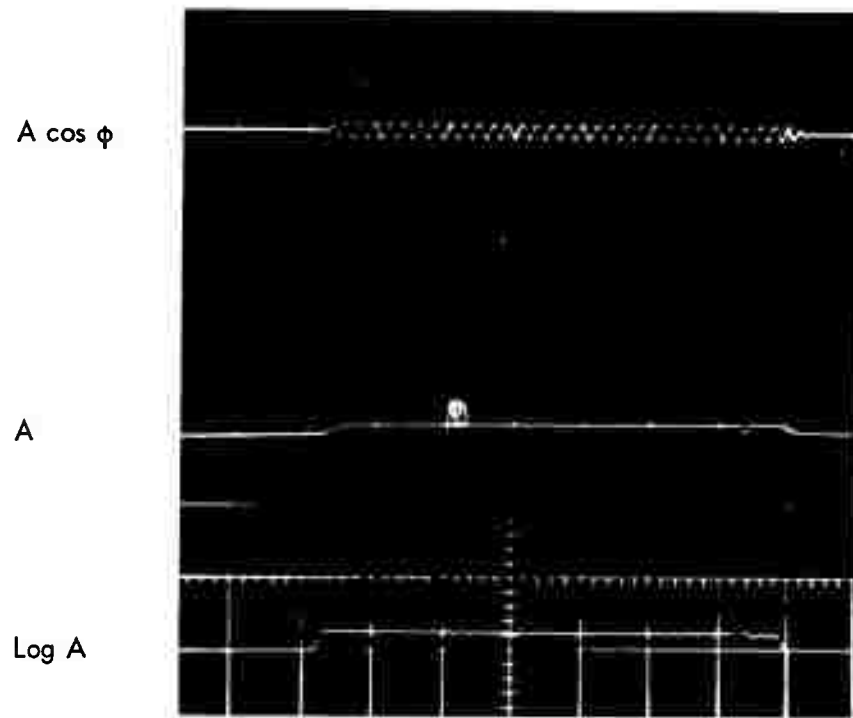
A cos φ

A

Log A

Fig. III-5. 1/4-inch aluminum pellet without wake.

A cos φ

A

Log A
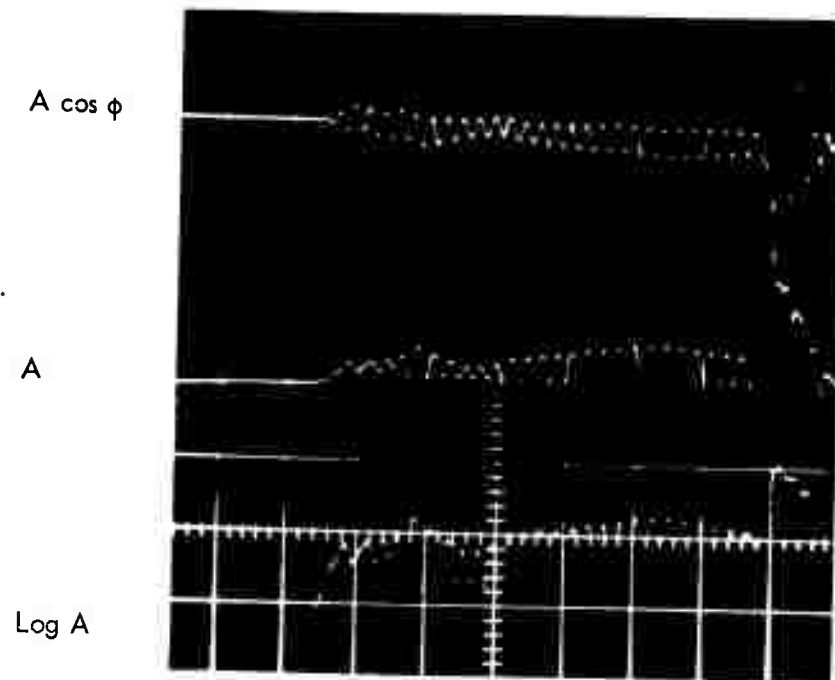
Fig. III-6.   1/4-inch aluminum pellet with
strong wake.

progresses quite smoothly, indicating as in earlier results that the scattering element producing this larger return is moving at the speed of the ball. Also as before, there is a "baseline fluctuation" in the phase, which is attributed to motion of a much slower reflecting medium. The linear and logarithmic amplitude detectors no longer give flat traces as in the bare pellet case. This is an indication that the waveguide contains more than a single reflector, and more than one reflector velocity, the modulation being a measure of relative velocity. When the pellet first enters the guide, the amplitude is modulated slightly, and the modulation phase is quite noisy. The modulation then increases and becomes more regular, having the same frequency as the synchronous detector output. Reflections from the wake arise from variations of electron density in a distance of the order of a half-wavelength. If the wake is considered to be of relatively small diameter, but turbulent in structure, then as the pellet progresses down the guide more and more of the wake is exposed to the incident radiation. The total signal reflected from the turbulent wake, which beats with the high-velocity return, is the complex sum of reflections from individual elements at random phase and amplitude. As more individual scattering centers are exposed, the total wake signal increases in the fashion of a two-dimensional random walk. It grows from a small, noise-like signal to one with a more or less constant amplitude and uniformly increasing phase, with phase rate corresponding to its over-all forward velocity. Since the final amplitude-modulation frequency is the same as that of the synchronous output, the wake is approximately stationary. (In some shots of $\frac{1}{2}$-inch pellets in argon, the wake has appeared to have a velocity nearly one-tenth the pellet velocity, as evidenced by both a sinusoidal baseline fluctuation of the synchronous detector output and a difference in the Doppler frequencies measured by the synchronous and amplitude detectors.) Since the modulation reaches 100 per cent, a further conclusion is that the moving reflector becomes equal in magnitude to that of the stationary portion. Where the amplitude modulation is less than 100 per cent, but periodic, the moving and stationary portions of the wake have different reflectivities. In this case, the amplitude return is compared to the rapidly varying portion of the synchronous output to determine whether the moving or stationary portion is

larger. The time required to settle down to uniform modulation gives an indication of wake length, as does the time required for the signal to disappear after the pellet leaves the waveguide.

Figure III-7 shows the traces for a 15,200-ft/sec $\frac{1}{4}$-inch aluminum pellet in air at 5.1 mm Hg pressure. Here the initial return is equal to that measured for a bare pellet, but the return increases slightly and gradually becomes modulated, finally achieving 100 per cent modulation. Note that the modulation is uniform in frequency, even when it is quite small. This difference from the previous result may indicate non-turbulent flow here, with turbulence setting in between this pressure and the previous 14 mm Hg (Sec. E).

In Fig. III-8, the return is from a $\frac{1}{2}$-inch nylon pellet traveling approximately 9000 ft/sec in air at 11 mm Hg pressure. This shot was fired through a shorter waveguide. Nylon pellets have been successfully fired through the apparatus only at this lower velocity. At the same velocity, $\frac{1}{2}$-inch aluminum pellets give no ionization indicating that the ionization pictured here is due primarily to ablation. This picture is typical of the nylon results in that it cannot be analyzed simply. There are large fluctuations in both the high-speed portion and the stationary portion of the wake, and ionization remains in the guide for some time after the pellet leaves. The large dip in amplitude just after the center of the sweeps may be due to plasma resonance in the region of the hybrid tee. It has been noted that the energy reflected toward the source is quite large for some time after a highly ionizing pellet passes the tee. Even though there are many $\frac{1}{2}$-inch nylon shots, not enough regularities have yet been observed to allow further discussion of these shots.

The signal transmitted through the waveguide is shown in Fig. III-9 for the $\frac{1}{4}$-inch aluminum shots presented in Fig. III-6 Slight fluctuations are seen which are due to reflections from the pellet as it approaches the probe. After it passes, the signal is attenuated appreciably. The time required to reach minimum transmission and the time to recover after the pellet passes the tee are further indications of wake length. The maximum attenuation here is about 12 db. For higher-velocity shots at the same pressure, practically full attenuation has been observed. An analysis of propagation in waveguide containing plasmas with the present characteristics is being undertaken.
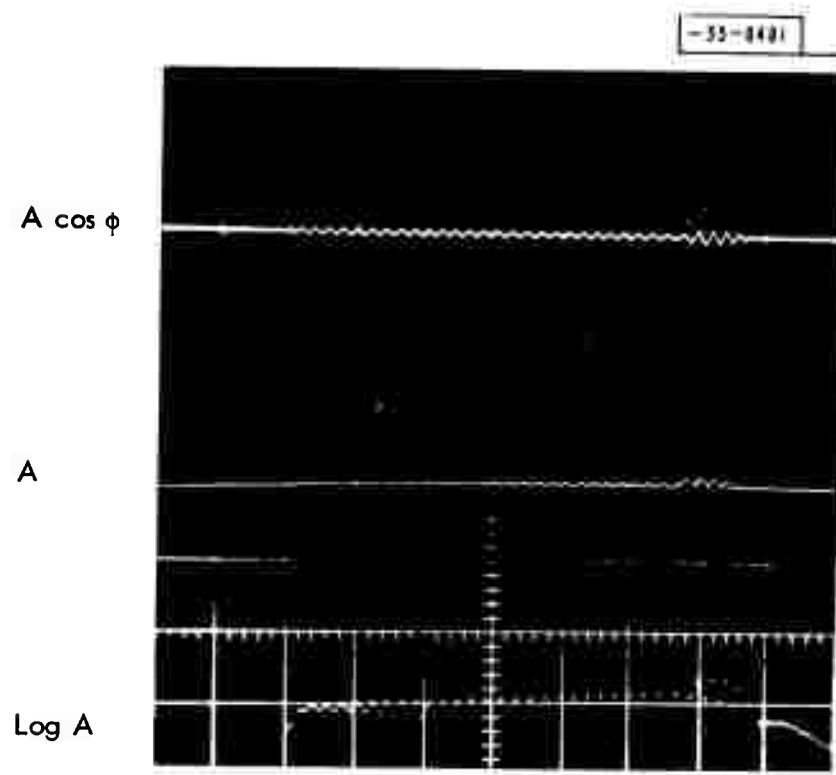
A cos φ

A

Log A

Fig. III-7. 1/4-inch aluminum pellet with small wake. This may show transition from laminar to turbulent flow.
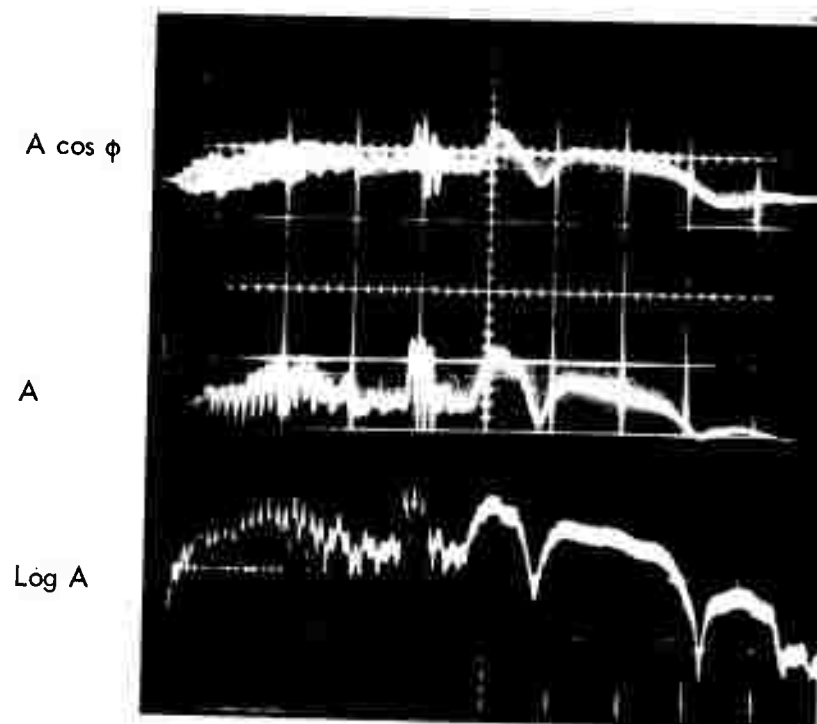
A cos φ

A

Log A

Fig. III-8. 1/2-inch nylon pellet with large wake.
The wake is due to ablation.

A cos φ
A

Log A
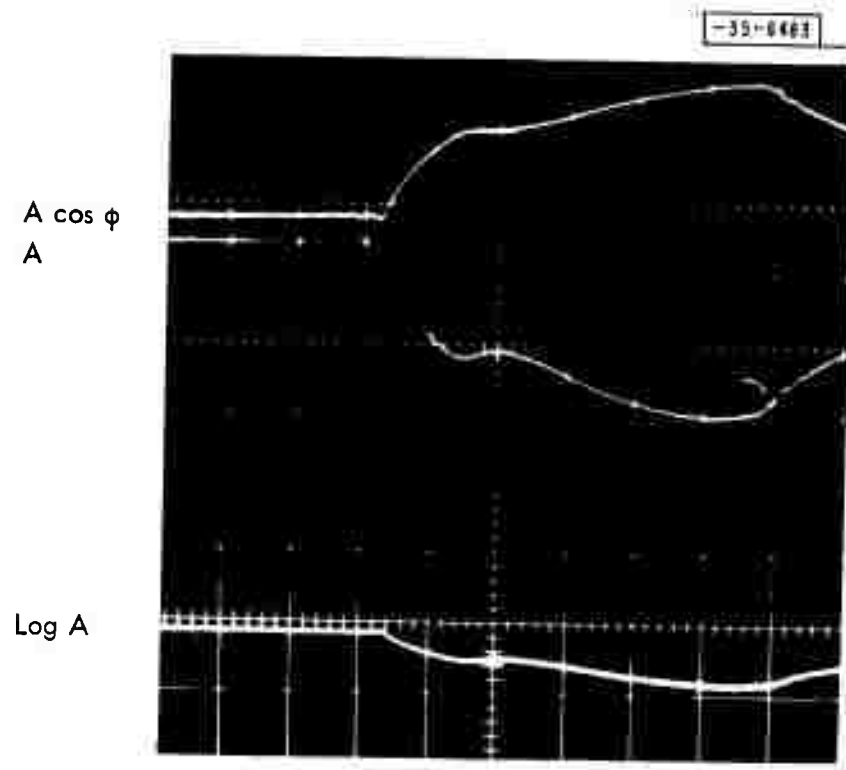
Fig. III-9. Signal transmitted through wake.
This is for the same shot shown in Fig. III-6.

Reflection coefficients for wakes of $\frac{1}{4}$-inch aluminum pellets at various velocities and three different pressures are shown in Fig. III-10. The horizontal dashed line is the bare pellet reflection coefficient calculated in Table III-2. The curves are drawn to call attention to the general trend of the data, which are as yet too scanty to define well-established curves. The points are for reflection coefficients of the portions moving at the pellet velocity; the circles are for the slow portions of the wakes.

The points at a pressure of 0.5 mm Hg scatter around the expected reflection coefficient for the pellet alone, with no measurable slow wake, indicating that the ionization density is always considerably less than 1.8×10^{10} cm^{-3} throughout this velocity range at this pressure. At 15,300 ft/sec, the line indicates that the reflection coefficient decreased uniformly during passage of the pellet. The total range is approximately 6 db, and may be attributed to the pellet entering on-axis but following a skew path so that it leaves the waveguide well off-axis.

There appears to be a limit to the reflectivity from the slow wake regardless of speed or pressure. This is apparently because the wake causes attenuation as well as reflection so that when the signal has propagated some distance down the waveguide containing the wake, it has become so attenuated that additional wake does not introduce additional reflection. In other words, the wake appears as a relatively good matched termination. Figure III-11 shows the initial rate of attenuation of the transmitted signal as the pellet passes the pickup probe, converted to db per foot of pellet travel. Almost complete attenuation is achieved after only a few feet of travel at velocities above the knee of each curve.

Discussion of wakes often brings up the question of length. There is not a unique length to the wake, but it depends upon the frequency and sensitivity of the measuring equipment. The techniques involving measure of rise times in this experiment do not give usable answers because of the attenuation of the signal propagated down the guide containing the plasma. Some information can be obtained from the recovery time of the transmitted and reflected signals after the pellet leaves the guide, but instrumental difficulties have prevented the accumulation of enough data to produce significant curves. Indications are
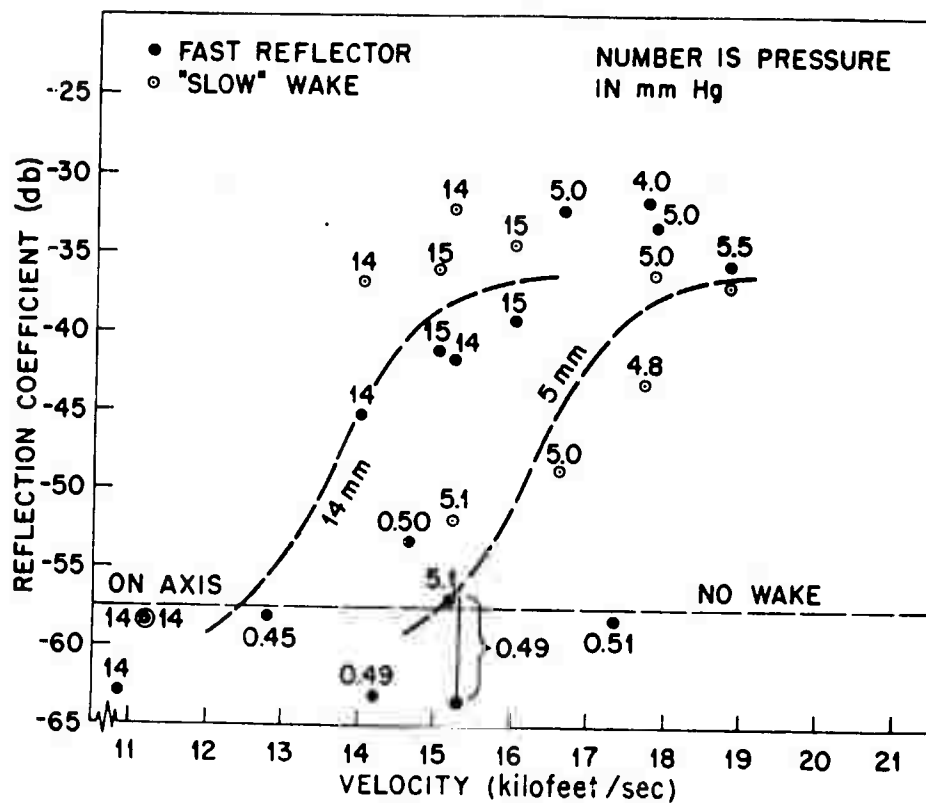
Fig. III-10. Reflection coefficients for 1/4-inch aluminum pellets.
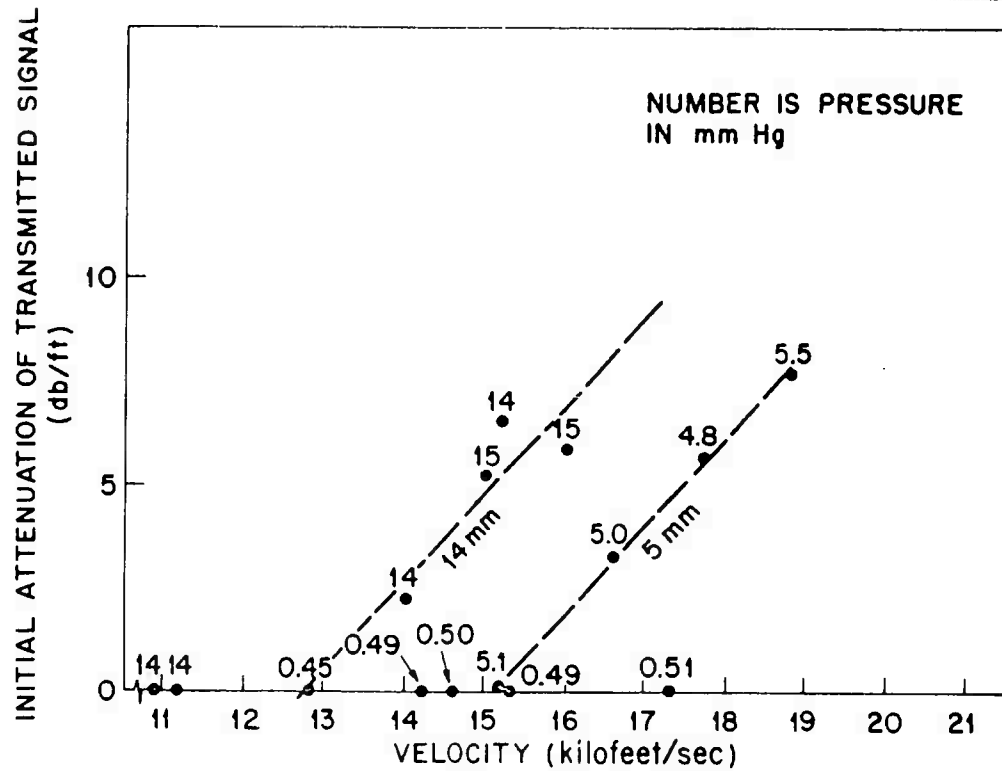
Fig. III-11.   Initial attenuation of signal transmitted through wake.

that this equipment measures appreciable disturbances for several meters after passage of highly ionizing pellets.

Care must be exercised in scaling the relative strengths of pellet and wake reflectivities presented here to larger bodies or to different wavelengths of radiation. The pellet reflectivity calculated in Table III-2 is for Rayleigh scattering, in which the reflection cross section is proportional to the sixth power of the radius and the inverse fourth power of the wavelength for a body very small compared to the wavelength. For body dimensions comparable to or larger than the wavelength, the variation of cross section with size or wavelength is much less. Concerning reflection from the ionized wake, the conductivity of the medium is also dependent upon the frequency of the incident radiation, so that the size and frequency dependence are more complicated than for a metallic conductor. Finally, the aerodynamics of larger bodies results in a different wake configuration, particularly if the body has a more complicated shape than the spheres used in this experiment.

E. TURBULENCE EXPERIMENTS

Optical measurements of the gross radial growth of free turbulence behind a hypervelocity sphere moving in air at one atmosphere of pressure were described in a previous report.[6] These experiments have been extended to lower pressures. The chief difficulty in obtaining data at lower pressure is in obtaining sufficient optical sensitivity to detect density changes in the lower ambient density. Surprisingly enough, despite fairly extensive literature on the subject of non-isotropic free turbulence,[7] almost no experimental work has previously been done for the case of long distances behind the projectile.

All the data described herein represent the turbulent trails behind projectiles fired from a .50-calibre Mann gun (the 0.250-inch spheres were also fired from guns of this type by means of a sabot). At one atmosphere, the spheres were fired through a microwave cavity which formed one arm of a balanced impedance bridge circuit at UHF frequency.[8] The change in impedance of the cavity due to the presence of the sphere creates an unbalance in the bridge and generates a timing pulse. The 0.50-inch data were taken by dividing this pulse. One pulse generates a variable delay which then fires

the spark optical system farther down range used to photograph the wake, and the other starts a microsecond counter. After passing through the optical system, the sphere passes into a second cavity system several feet farther down range. The pulse generated in this case stops the counter. The variable delay permits one to position the portion of the trail under study in the spark photograph, and the time count over a fixed distance gives a measure of average velocity

In the case of the sabot-fired 0 250-inch spheres, a single cavity followed by two crossed parallel-light shadowgraph systems were used. Since the velocity of the projectiles is highly predictable, a fixed delay is used to photograph the sphere with one optical system, confirming the predicted velocity. The firing of the spark initiates a variable delay which fires the second spark sometime later. The second spark is used to photograph the trail in the position previously occupied by the sphere

The low-pressure data were taken in the 5-foot evacuatable tank. A series of light stations and/or cavities was used to measure the velocity of the projectile. The trail itself was photographed by means of a vacuum schlieren system shown in outline in Fig III-12 The main optical arm of the schlieren system is evacuated to the same pressure as that of the tank, eliminating the necessity for plane windows, and reducing the problems of normal convection turbulence generally encountered when the parallel light beam travels a portion of its path through atmospheric air The spark photograph itself was taken via a variable delay initiated by a light screen crossing the field of view of the schlieren system Figure III-13 shows a typical photograph of the turbulent trail taken with this schlieren system (30 mm Hg of air, approximately 185 body diameters behind a 0 500-inch aluminum sphere) The apparent downward course of the trail is due to the offset nature of the optics.

Figures III-14 and III-15 show the results of these measurements. Each datum represents a single photograph of a portion of the trail behind a single shot The uncertainties indicated on each individual datum represent the maximum possible measuring error in determining the trail width at the particular point. In all cases, the trails extended well beyond the distance shown but were not measurable due to the limiting size of our optical system. The lens
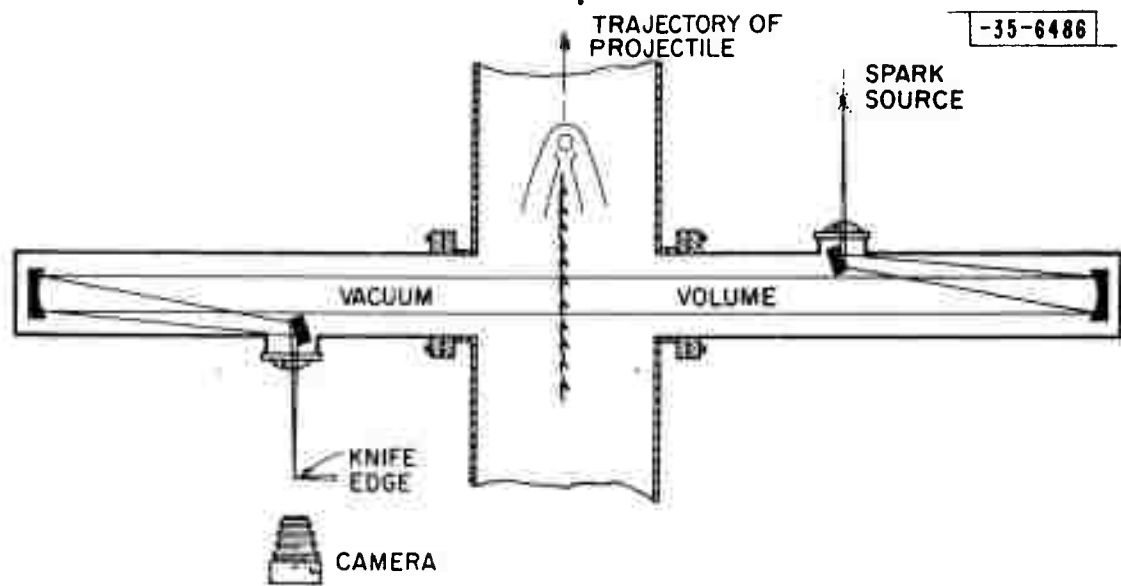
6-inch vacuum schlieren
(18 ft between mirrors, not to scale)

Fig. III-12. Vacuum arm schlieren system.

Fig. III-13. Typical turbulent trail 185 body diameters behind a 0.500-inch aluminum sphere at a pressure of 300 mm Hg of air.
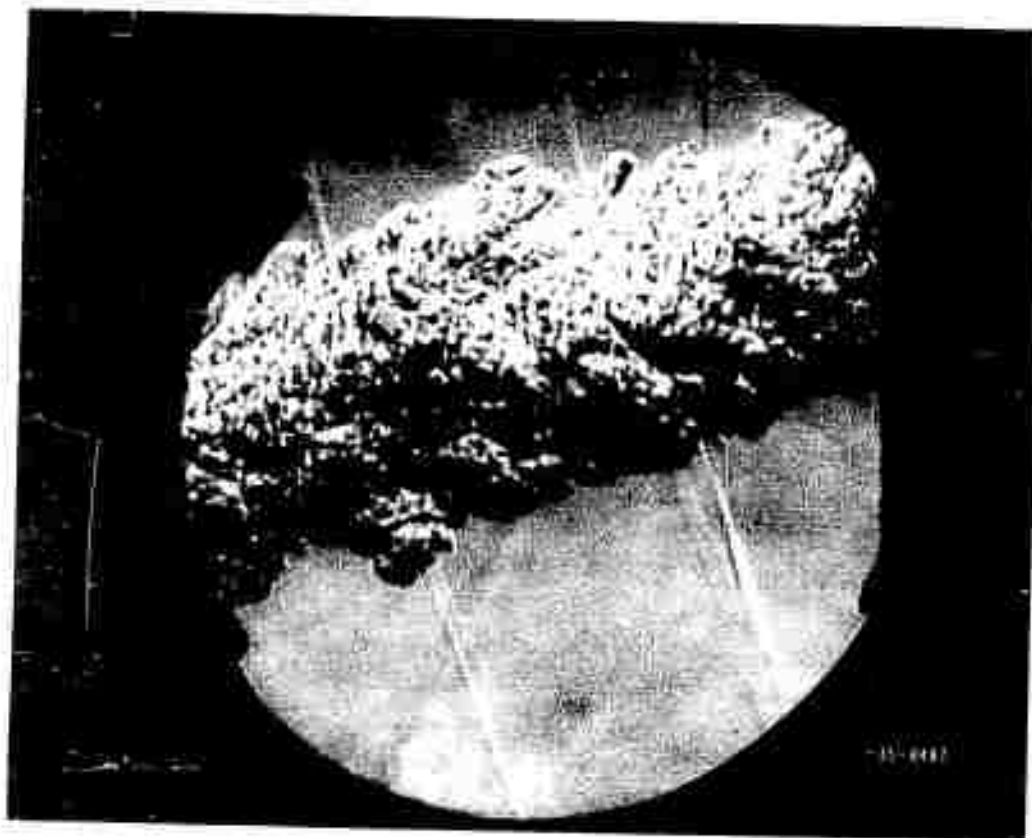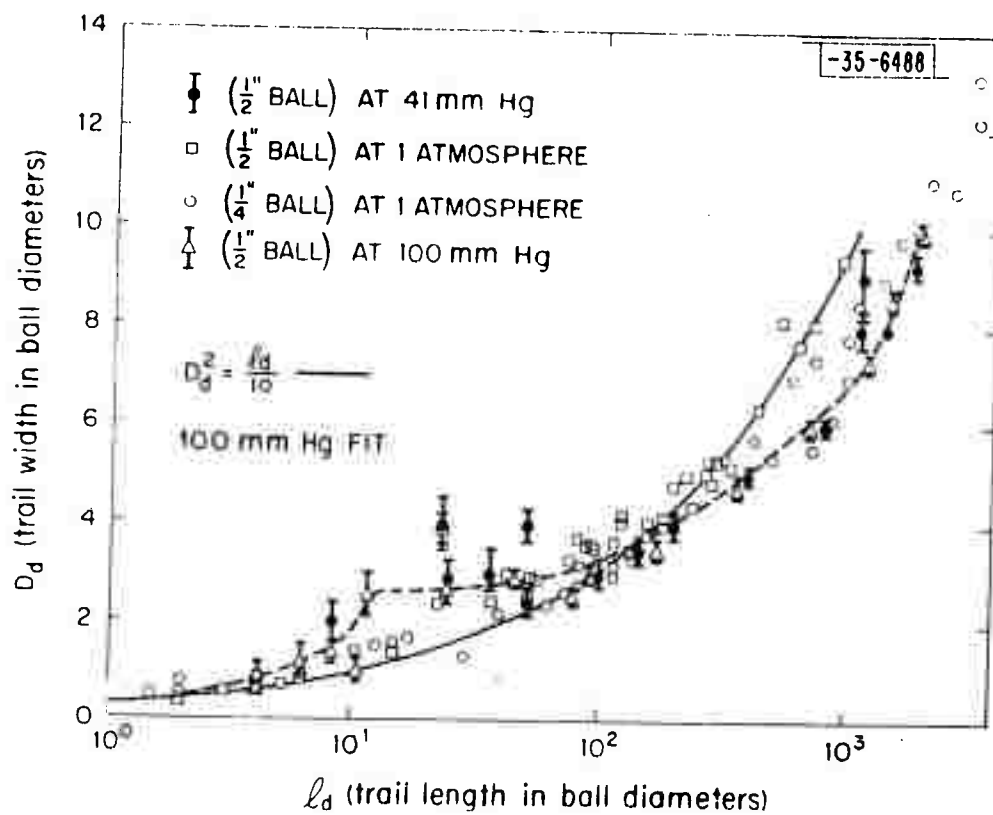
Fig. III-14. Trail width as a function of trail length.

shadowgraph (a comparatively insensitive technique) clearly indicated the presence of turbulence for as long as one-half second after the passage of a 0.500-inch sphere at one atmosphere. (This corresponds to approximately one mile behind the sphere.)

Several of the shots at low pressure were fired using nylon spheres and were allowed to enter the waveguide of the Doppler experiment. Data from this experiment have shown that the slow reflective portion of the wake, which appears turbulent, sometimes has a velocity from 10 to 15 per cent of the projectile velocity. If one assumes that this portion of the wake plasma, which is seen by the Doppler equipment, can be associated with the turbulence viewed optically, then the translational velocity of the turbulence is of the order of 900 to 1200 ft/sec. Although this value appears reasonable, and is of the order predicted by theory, motion pictures give the impression that the wake tends to slow farther than this, and is then set into motion again by the wind generated by the muzzle gases of the gun.

The results plotted in Figs. III-14 and III-15 indicate that there is little or no difference in the growth of gross turbulent width between 40 mm Hg of air pressure and one atmosphere. If anything, the turbulence grows slightly more slowly at lower pressures. (The pressure range changes the Reynolds number by a factor of 19.)

The "bump" in the data of Fig. III-14 in the region ℓ_d = 25 to 50 ball diameters corresponds to the transition predicted by Hromas and Lees[9] as the turbulent core diffuses from the hot rarified region containing the streamlines originating near the stagnation region, into the colder, denser surrounding region Calculations by Hromas and Lees for the size and velocity parameters of this work give excellent agreement with our data.

The atmospheric pressure data in Fig. III-14 follow a curve of the form $\ell_d = D_d^2/10$ by least squares fit. The logarithmic plot of Fig. III-15, of course, indicates a similar $\frac{1}{2}$-power dependence of width upon length (some uncertain data taken with larger optical aperture, not shown, tend to confirm this). For the lower pressures, the data are best fitted to a $\frac{1}{2}$-power dependence for about the first 50 or so body lengths; thereafter, a $\frac{1}{3}$ law appears better. The transition of dependence is expected and corresponds to the transition region predicted above.
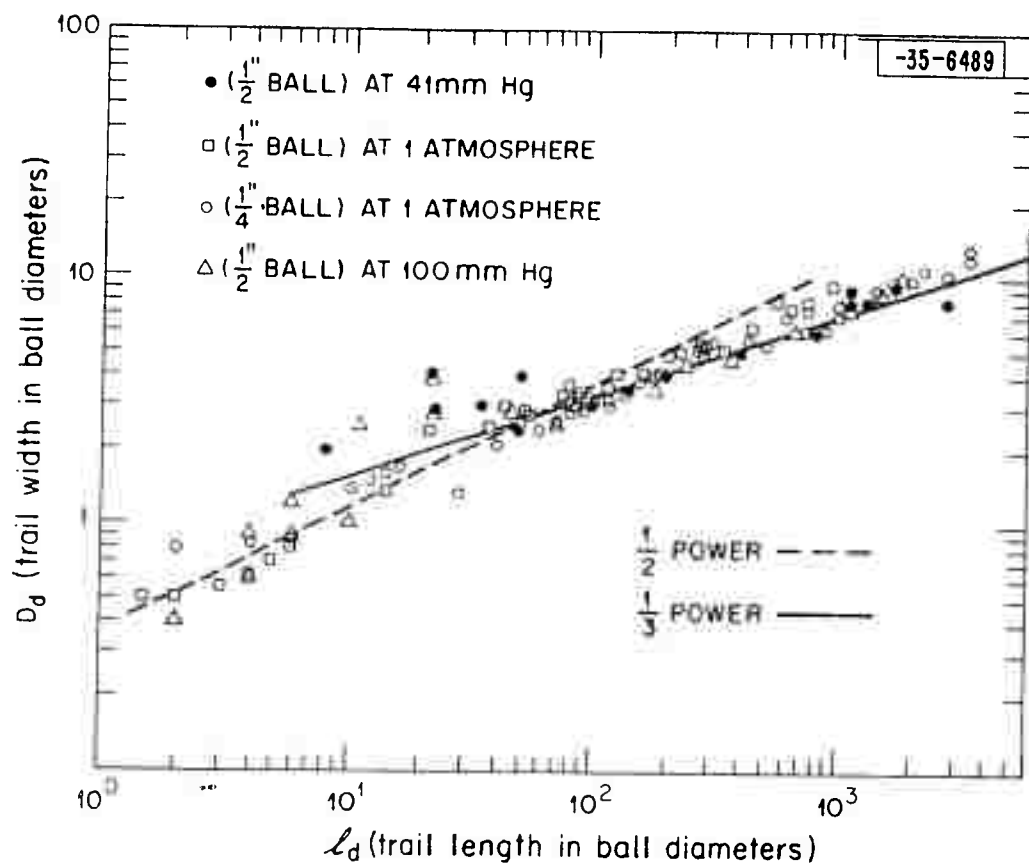
Fig. III-15. Trail width as a function of trail length illustrating functional dependence.

As a natural adjunct to the measurement of turbulent diffusion at reduced pressures, an attempt has been made to observe the transition from laminar to turbulent flow in the hypersonic wake created under our experimental conditions. The transition at 40 mm Hg has been photographed for the case of $\frac{1}{2}$-inch and $\frac{1}{4}$-inch spheres. At 8300 ft/sec, these occur at ~4 body diameters and at ~20 body diameters behind the sphere, respectively. In addition to the two sphere sizes, the transition has also been photographed in argon at 40 mm Hg pressure. The change in the position of the transition point with these changes in Reynolds number serves as a check on our work and provides surety that we are indeed viewing the laminar-turbulent transition. The transition for the $\frac{1}{2}$-inch sphere is shown in Fig. III-16. These results are necessarily preliminary, and we are in the process of constructing a double-pass 12-inch mirror vacuum schlieren system to continue this work.

The growth of turbulence has also been photographed by a Fastax motion picture camera (8000 frames/sec) at pressures from 40 mm Hg to one atmosphere. It is planned to continue this work on a systematic basis. The time record of the turbulent growth should provide an indication of the velocity distribution behind the body. In addition, a statistical analysis of cell and eddy size should correlate with the electromagnetic reflectivity of the wake plasma at various RF frequencies, leading to improved understanding of the radar cross sections to be expected.
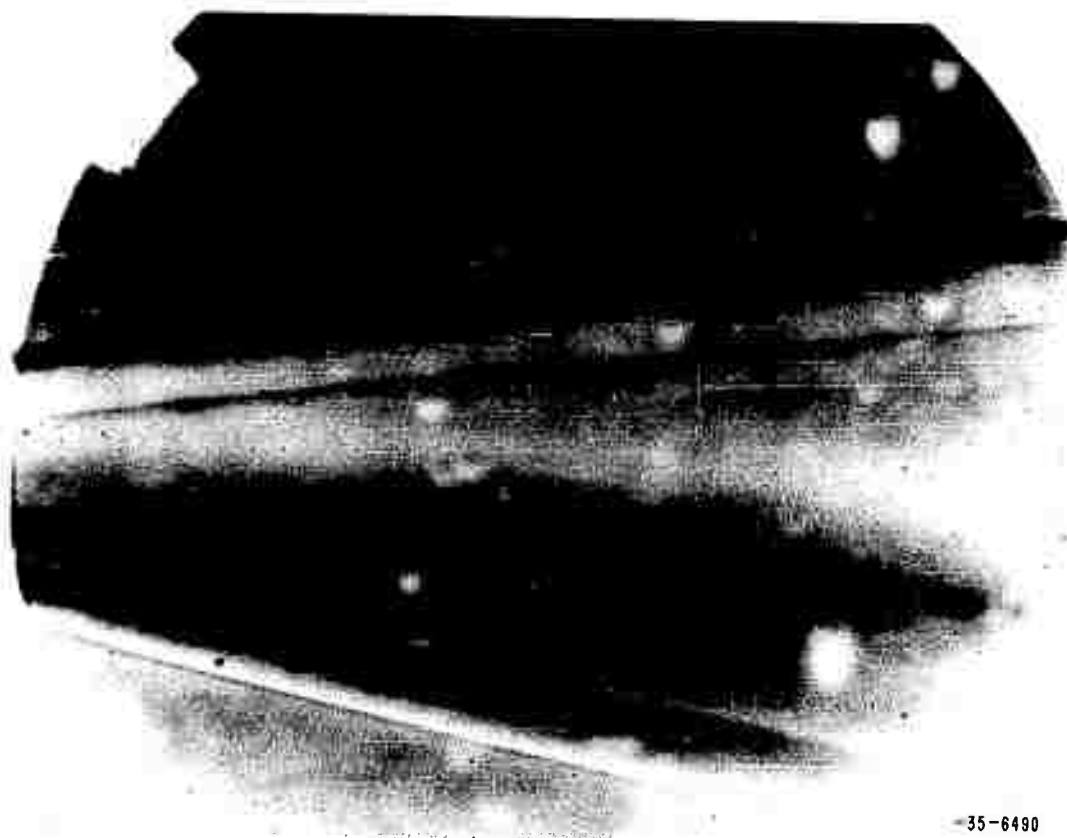
35-6490

Fig. III-16. Transition from laminar to turbulent flow in the wake of a 1/2-inch pellet fired at 8300 ft/sec through air at 40 mm Hg pressure.

REFERENCES

1. Chanin, Phelps and Biondi, Phys. Rev. $\underline{2}$, 344 (1959).

2. Wray, Teare, Kivel and Hammerling, Research Report 83, Avco-Everett Research Laboratory (December 1959).

3. S. Feldman, Research Report 82, Avco-Everett Research Laboratory (December 1959).

4. A. V. Phelps and J. L. Pack, Phys. Rev. Letters $\underline{3}$, 340 (1959).

5. S. Feldman, Research Report 71, Avco-Everett Research Laboratory (June 1959).

6. "Reentry Physics Program, Semiannual Technical Summary Report to the Advanced Research Projects Agency," Lincoln Laboratory, M.I.T. (30 June 1960), p. 7, ASTIA 252669.

7. See, for example, J. O. Hinze, Turbulence, an Introduction to Its Mechanics and Theory (McGraw-Hill, New York, 1959).

8. M. A. Herlin, W. G. Clay, M. Labitt and R. E. Slattery, "The Reentry Simulating Range," 14th Conference on Hypervelocity and Impact, Eglin Air Force Base, Florida, 1960.

9. L. Hromas and L. Lees, "Turbulent Diffusion in the Wake of a Blunt-Nosed Body at Hypersonic Speeds," Space Technology Laboratories report to be published.

IV. ELECTROMAGNETIC INTERACTIONS WITH REENTRY PLASMAS[*]

A. INTRODUCTION

During the fifth semiannual reporting period, microwave data were collected in the NASA Ames Hypervelocity Ballistic Range. Studies of these data were continued, along with several theoretical analyses involving scattering from cylindrical and spherical plasmas.

B. S-BAND EXPERIMENTS

A series of low-pressure (in the order of 1 mm Hg) shots was monitored in the Ames HBR. The scatter in the data is larger than was previously encountered at high pressures. The data from two such firings, MS-134 and MS-144, were analyzed and resulted in plots of electron density and plasma cylinder diameter. These are shown in Fig. IV-1. It is seen that the electron densities are at least an order of magnitude lower than those obtained previously at 10 mm Hg and reported in Fig IV-1 of the Fourth Semiannual Report dated 31 December 1960. The wake diameter does not increase significantly. However, the erratic shapes of the curves are not necessarily due to real effects, but rather possibly to experimental difficulties. An error analysis is being conducted in order to trace the sources of error. Equipment changes and changes in the methods of data analysis, described below, are being made in order to improve the reliability of the interpreted results.

The S-band experimental data are obtained as photographs of oscilloscope traces. Calibration curves and conversion formulas are used to find reflection and transmission coefficients and phase of the reflected signal. A table that lists these three intermediate quantities vs plasma frequency and trail radius is used with any two of these quantities to obtain trail radius and plasma frequency The third quantity is used as a check.

This process has been partially mechanized A Benson-Lehner Oscar is used to transfer the data from photographic to a digital punched card format.

---

[*] The work reported in this section was performed by S. Edelberg, D. E. Crook, C. M. deRidder, B. D. Fowler, M. R. Gorn, N. E Holway, J. J. Mikulski, E. L. Murphy, H. G. Pascalar and L. G. Peterson, Group 312.
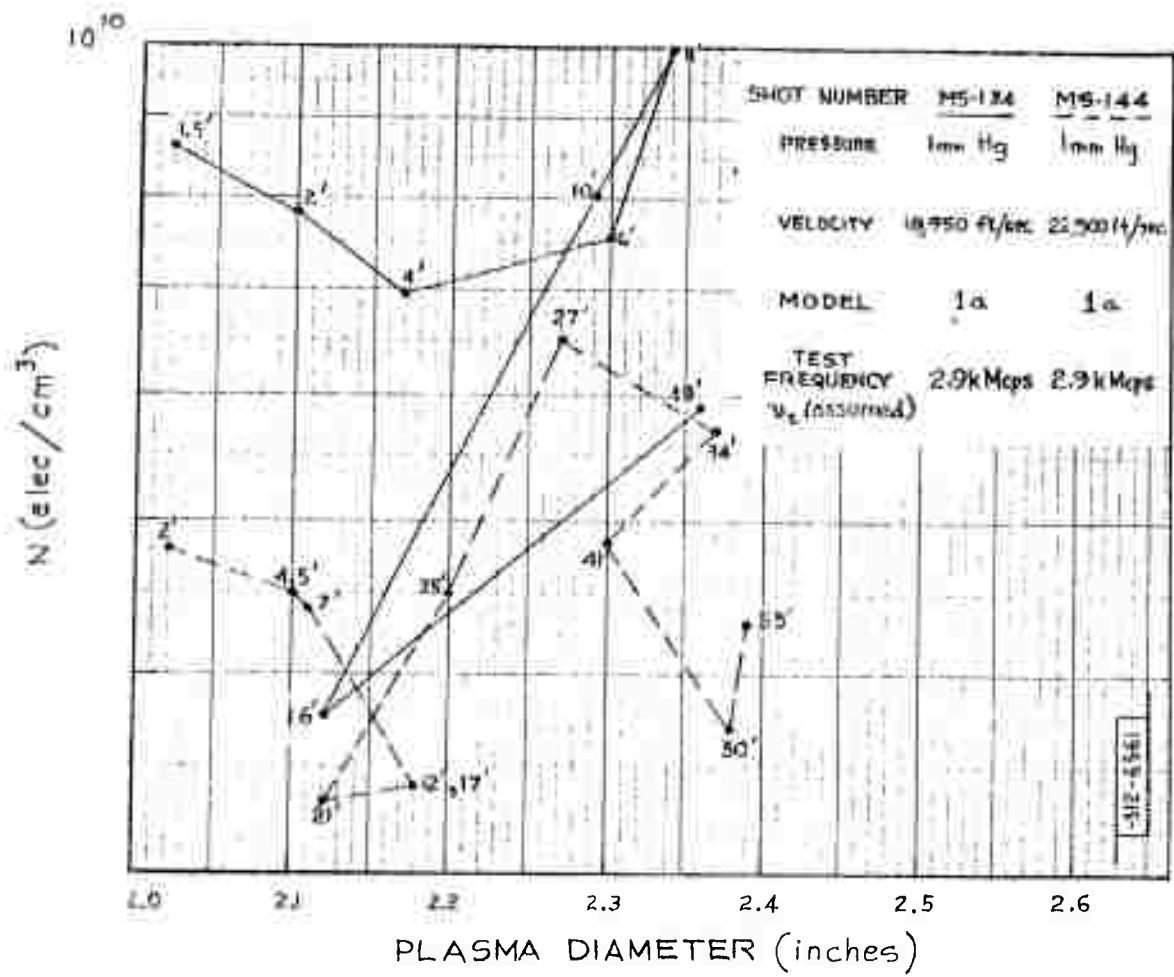
Fig. IV-1. Plasma trail characteristics for low pressures obtained with S-band horn equipment in NASA Ames HBR.

Programs have been written for the IBM 7090 to take data from the cards and compute reflection and transmission coefficients. Two programs are as yet incomplete: one is to compute phase and the other is to calculate by interpolation all the intermediate quantities at specified distances behind the pellet. To facilitate the conversion to plasma frequency and trail radius, the program that computes the reflection and transmission coefficients and phases on the basis of a uniform cylindrical trail has been modified to permit plots to be made of both constant plasma frequency and constant radius curves vs transmission and reflection coefficients. This grid structure provides a direct addressing of plasma frequency and trail radius for any given set of coefficients.

During one of the Ames HBR firings, an accelerometer with an attached aluminum disc, 2 inches in diameter, was suspended 5 inches from the line of flight of the pellet with its axis at an angle of 30° to the line of flight. The pellet traveled at 25,000 ft/sec in air at a pressure of 1 mm Hg. The trace of accelerometer voltage indicated that a wildly oscillating pressure wave of magnitude on the order of 1 mm Hg began approximately 20 ft behind the pellet. This could be the result of shock waves or possibly the incidence of propelling gas from the gun. Neglecting the occurrence of the latter and the effect that it would have on the trail, this disturbance may still cause experimental error, since the pressure may move the microwave absorber within the isolation box in the same way that it moves the accelerometer. However, most of the absorber is much farther than 5 inches from the trail. To lessen any such effects, a higher-performance absorber is to be used.

It has been found that for low-pressure (1 mm Hg) shots, the 60- and 120-cycle ripple is greater than the attenuation by the plasma trail. Most of this ripple originated in the traveling-wave tube amplifier, which has been returned for servicing and some redesign. Changes are being made at other points in the system where such noise may be induced. As a further measure, a photograph of a full cycle of the ripple in the transmitted power before the pellet enters the box will be taken. The attenuation by the trail will then be found by taking the difference between the observed power and the extrapolated ripple.

C. UHF CAVITY EXPERIMENTS

The 400-Mcps resonant cavity and associated instrumentation system was described in a previous report and has been operating reliably at the Ames HBR. The recorded data consist of the magnitude and phase of the voltage reflection coefficient (Γ_V) measured at the input of the cavity. The data analysis performed to date is based on an assumed model of the plasma trail. The following paragraphs outline the essentials of the analysis.

For the particular cavity employed here, a numerical relationship has been established between the value of cavity input admittance and the electron-density and collision frequency of a plasma located in the cavity. This relationship is based on the assumption of a model that represents the ionized trail as a plasma cylinder possessing a distinct radius and uniform electron-density and collision frequency. The two major factors of this relationship are:

(1) The admittance presented by the plasma, at a specified location within the cavity, as a function of the plasma dimensions, electron-density and collision frequency.

(2) The admittance transformation existing between the specified plane in the cavity and a specified plane on the input transmission line.

In order to determine factor (1), it is necessary to assume a model for the plasma density distribution. If the plasma is assumed to be a uniform-density cylinder, and since the cavity consists of a rectangular waveguide section, the solution for the plasma admittance in terms of electron density corresponds to that developed by Marcuvitz for the complex dielectric $\overline{\text{post}}$ in a waveguide. Using the dielectric constant of the plasma as given in terms of electron-density and collision frequency, calculations were made for the normalized admittance of various diameter plasma posts. The results indicate that for plasmas with diameters up to 4 inches, the pure shunt circuit representation could be used. They also showed that the admittance was directly proportional to the cross sectional area of the post and to the electron density. For a fixed diameter and electron density, the dependence of the admittance upon operating frequency f and collision frequency ν is given by $(1 + \overline{\nu}^2)^{-1}$, where $\overline{\nu} = \nu(2\pi f)^{-1}$. It is then possible to express the admittance for arbitrary values of electron

density N, collision frequency $\bar{\nu}$, and diameter d, in terms of an admittance for a certain set of N, $\bar{\nu}$ and d and normalized values of these variables.

For a 2-inch diameter plasma post, with $\bar{\nu} = 1$ and an electron density N yielding a plasma frequency equal to the signal frequency, the normalized admittance equals:

$$Y'_P = 0.044(1 - j) \qquad (IV-1)$$

In terms of arbitrary values of N, $\bar{\nu}$ and d (cm) the normalized admittance presented by the plasma post at the center of the waveguide cavity is given by:

$$Y'_P(N, \bar{\nu}, d) = 2.10 \times 10^{-12} \, NA \left(\frac{\bar{\nu} - j}{1 + \bar{\nu}^2} \right) , \qquad (IV-2)$$

where A is circular cross section in cm^2.

Equation (IV-2) involves the admittance transformation (n^2) occurring between the cavity center and a specified plane in the input transmission line. In the case of the cavity used in the hypervelocity tunnel, transit holes and cut-off tubes are present to permit the projectile to pass through the cavity without appreciable energy being lost because of radiation. Since the plasma cylinder in actual practice extends through the cavity on the axis of the cut-off tubes, the admittance apparent at the cavity center in this case differs from that which would occur with the plasma in the closed-wall waveguide. Thus, a correction factor is required to take into account the effect of the cut-off tubes upon the measured admittance For the cavity as presently employed, the experimentally determined correction factor is 0.725 and the value of n^2 equals 338. The resultant product is the corrected transformation ratio. Hence the input admittance normalized to the characteristic admittance of the input transmission line is given by:

$$Y'_{IN} = 246 \, Y'_P \qquad (IV-3)$$

In terms of electron density and collision frequency:

$$Y'_{IN} = 5.17 \times 10^{-10} \, N_\ell \left(\frac{\bar{\nu} - j}{1 + \bar{\nu}^2} \right) , \qquad (IV-4)$$

where: N_ℓ = NA = line density of electrons (electrons/cm).

The value of Y'_{IN} is given in terms of the measured voltage reflection coefficient Γ_V by:

$$Y'_{IN} = \frac{1 - \Gamma_V}{1 + \Gamma_V} \quad . \tag{IV-5}$$

The photographic data yield Γ_V as a function of time after the projectile passage. The real and imaginary parts of Y'_{IN} are determined by means of Eq (IV-5). From Eq. (IV-4) it is apparent that $\bar{\nu}$ equals the ratio of the real to the imaginary part of the input admittance. With $\bar{\nu}$ determined, the line density of electrons can be determined by using the imaginary part of the input admittance in Eq. (IV-4).

The photographic data for rounds MS-129 and MS-132 are given in Figs. IV-2 and IV-3, respectively. The plot of N and $\bar{\nu}$ for MS-129 is shown in Figs. IV-4(a) and (b), and for MS-132 in Figs. IV-5(a) and (b).

Examination of the data shows that for a fixed pressure (1.0 mm Hg), the level of ionization is quite sensitive to velocity. It must be remembered that the electric field should penetrate into the plasma, and that this becomes less likely as the plasma frequency exceeds the signal frequency. The volume density of electrons for a plasma frequency of 400 Mcps is: $N = 2.07 \times 10^9$ electron/cm^3. Hence, especially in the case of the high-velocity rounds, the measured data appear to indicate that the plasma is initially and for quite a distance overdense. In the overdense region, the plots of N_ℓ and $\bar{\nu}$ are of questionable validity; only when the final decay portion of the curve has been reached can there be any justification for attempting to interpret these plots literally as the electron line density and collision frequency.

The present conclusions are that, for pressures exceeding 1.0 mm Hg and velocities exceeding 18,000 ft/sec., the 400-Mcps cavity system is of limited utility. However, for pressures below 1.0 mm Hg, the cavity system — by virtue of its great sensitivity — should prove exceedingly useful.

D. DOUBLE-PROBE EXPERIMENTS

The double-probe experiments have been continued at the NASA Ames HBR. The data from several shots have been analyzed, using the theory described in
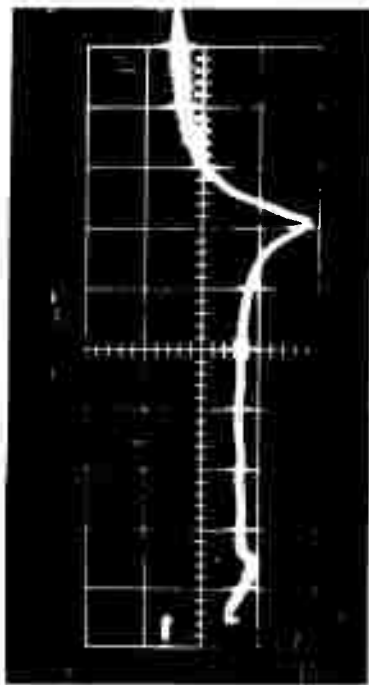
PHASE DETECTOR #2
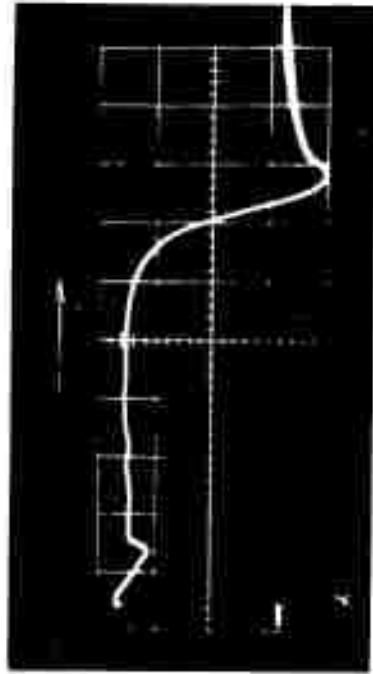
PHASE DETECTOR #1
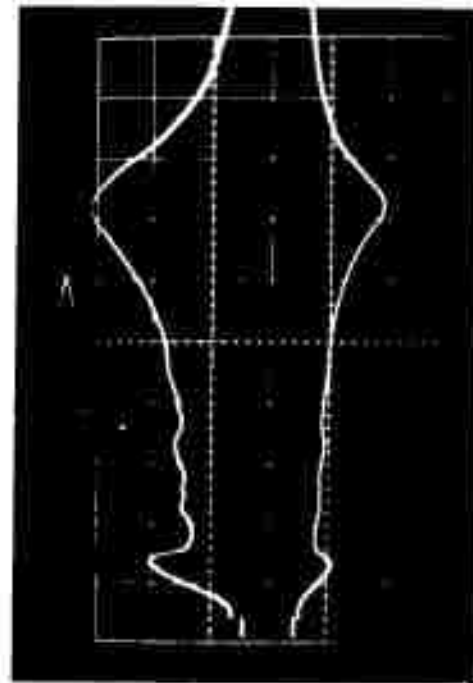
AMPLITUDE   UPPER: LINEAR
DETECTORS   LOWER: LOGARITHMIC

Fig. IV-2. Photographic data for round MS-129.

-312 - 6562

PHASE DETECTOR #2

PHASE DETECTOR #1

AMPLITUDE   UPPER: LINEAR
DETECTORS   LOWER: LOGARITHMIC
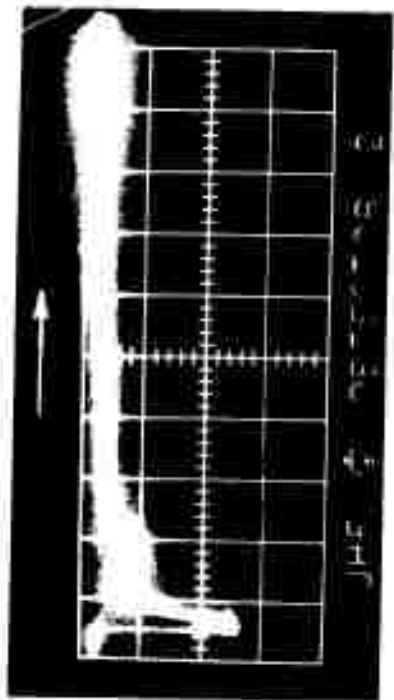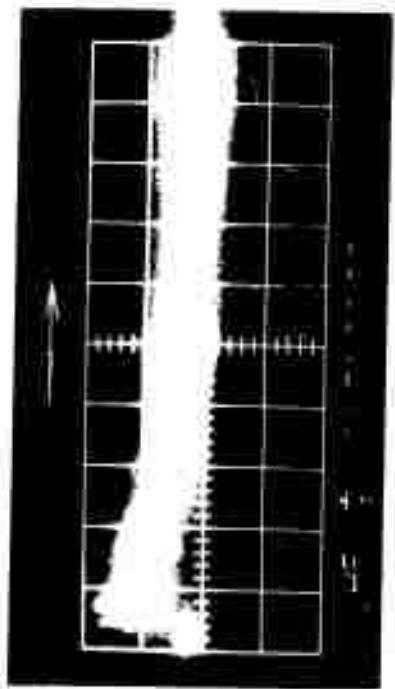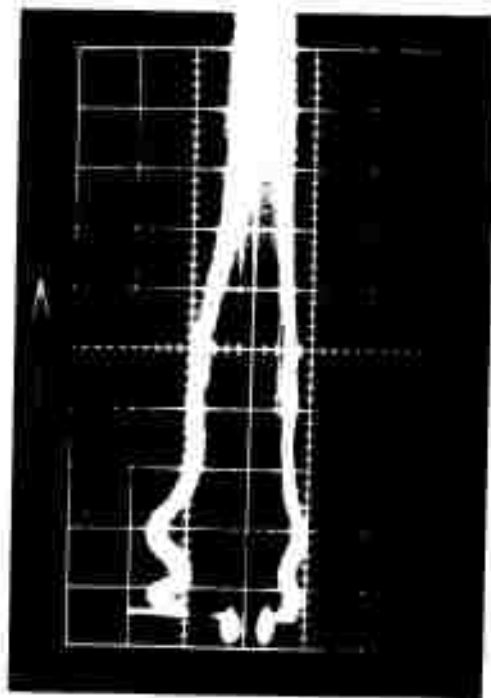
Fig. IV-3. Photographic data for round MS-132.
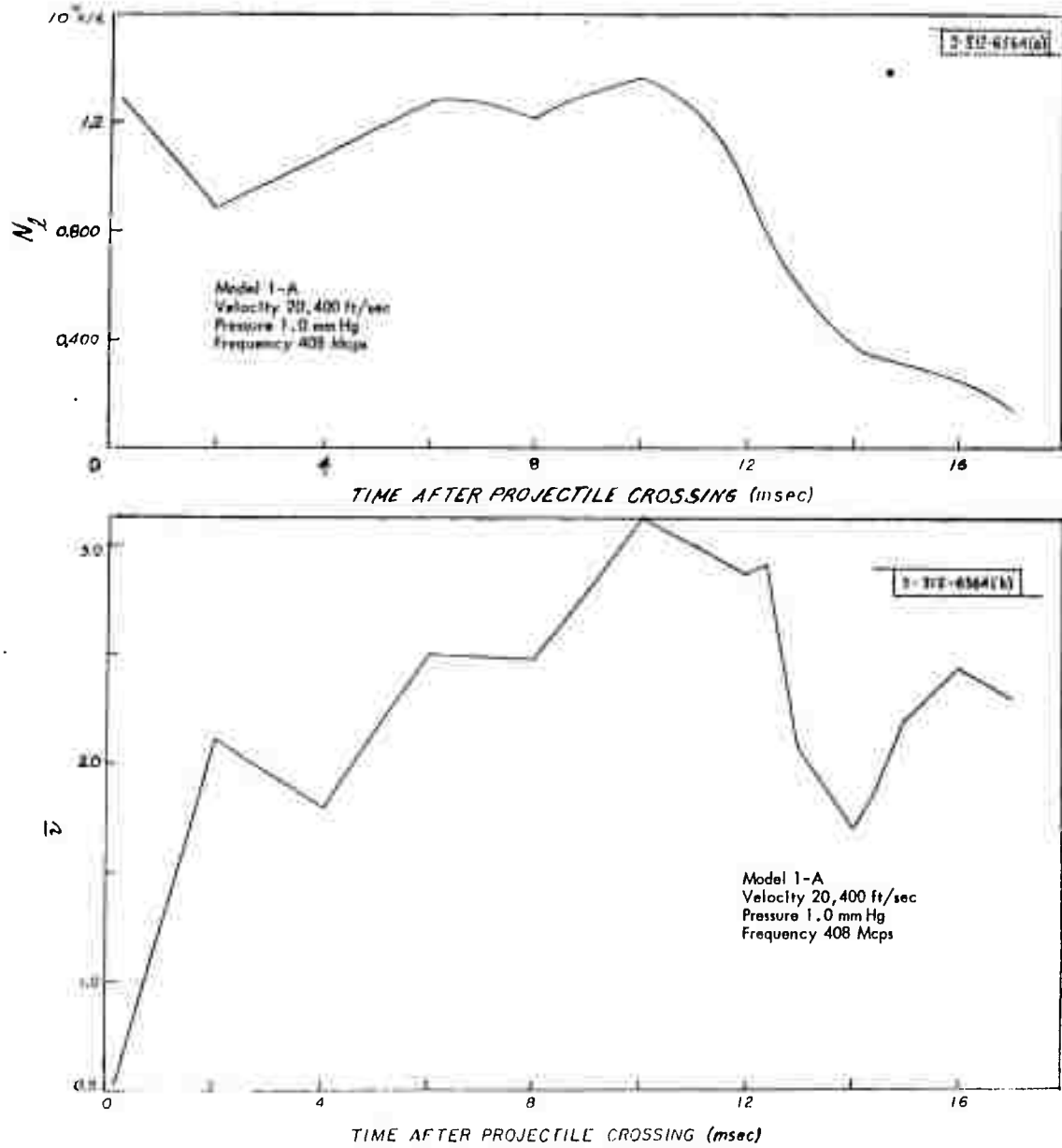
Fig. IV-4. Plasma wake characteristics obtained with UHF cavity at NASA Ames HBR (round MS-129).
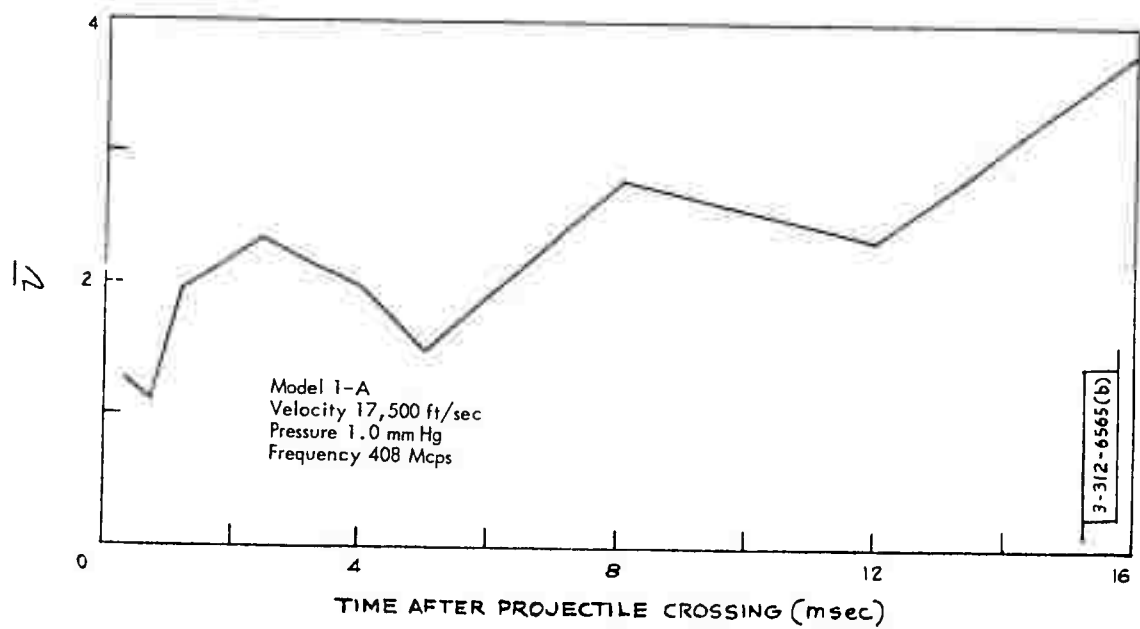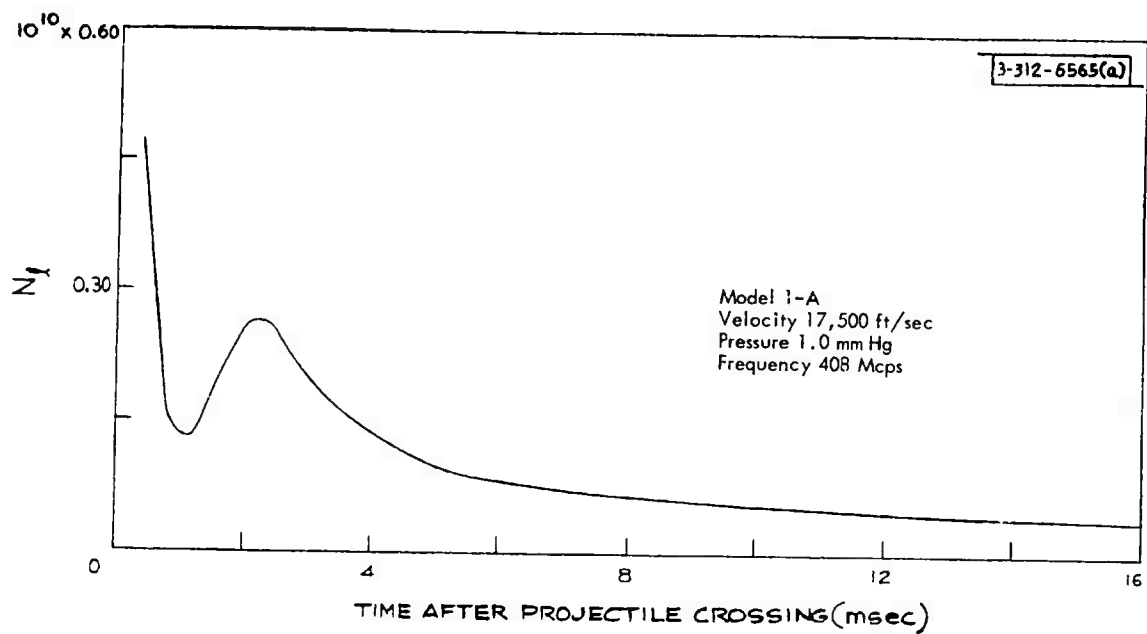
Fig. IV-5. Plasma wake characteristics obtained with UHF cavity at NASA Ames HBR (round MS-132).

Sec. IV-F of the Fourth Semiannual Report. For example, for MS-134 (see Fig. IV-1 for the shot parameters) with the probe about 1.5 inches from the plasma axis, the results in Table IV-1 are obtained.

TABLE IV-1
PROBE RESULTS

Distance behind pellet (ft)	10	20	30	40	50
N(electrons/cm^3)	4×10^8	7×10^8	7×10^8	10^9	10^9

The time constants of the probe circuitry are now being decreased in order to determine the fine structure in the wake.

E. LEAKY-WAVE MODES ON PLASMA CYLINDERS

Results concerning propagating modes on an infinite plasma cylinder were presented in the last semiannual report. These were found to be of the slow-wave type and, in comparison with dielectric antennas, would account for axial lobes in a scattering pattern. It was stated that further study would be concentrated in the determination of complex solutions to the mode equations — the so-called leaky-wave modes. In the last six months this study has been completed with some success.

A fundamental difference between slow-wave modes and leaky waves has been alluded to previously when solutions of the mode equations which fail to satisfy the radiation condition were found possible. These were termed improper resonances and neglected. In looking for complex solutions, a similar situation is encountered, as well as the fact that a complex propagation constant implies an attenuation. If this attenuation is large, as it may well be, it would be difficult, conceptually, to postulate a current on the structure which acts as an antenna current in solving for the scattering pattern. The initial task was then to formulate the problem in a manner that would demonstrate the significance of leaky-wave modes. This is accomplished by studying the excitation problem, i.e., the field due to a source in the vicinity of the structure.[1] Although the problem of a line source over a plasma slab was studied in detail,
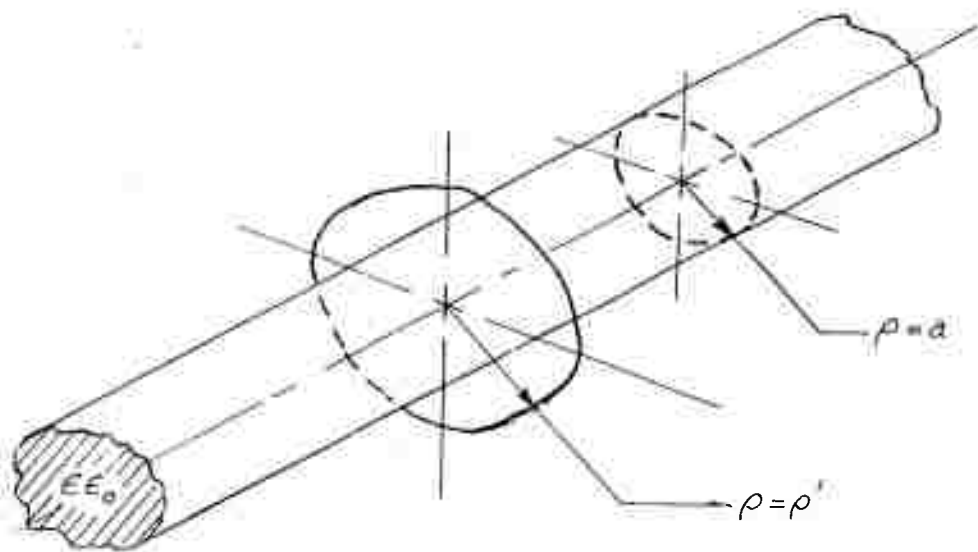
Fig. IV-6. Homogeneous plasma cylinder and ring source of current.

it will not be reported here. This problem is not of immediate interest to us and is also being investigated by other researchers.[2] The problem corresponding to our study is that of a ring source of current encircling the plasma cylinder (Fig. IV-6). For TM-(E-) modes, the source is a ring of magnetic current:

$$\overline{M} = \overline{e}_\Theta M_\Theta = \overline{e}_\Theta \frac{j}{\omega\epsilon} \frac{\delta(\rho - \rho')\ \delta(z)}{\rho} \quad , \tag{IV-6}$$

where δ is the Dirac delta function. For the TE-(H-) modes, the source is a ring of electric current:

$$\overline{J} = \overline{e}_\Theta J_\Theta = \overline{e}_\Theta \frac{j}{\omega\mu} \frac{\delta(\rho - \rho')\ \delta(z)}{\rho} \quad . \tag{IV-7}$$

In the first case, the field equations yield:

$$\frac{\partial}{\partial\rho} \frac{1}{\rho} \frac{\partial}{\partial\rho}\ \rho\ H_\Theta + \frac{\partial^2}{\partial z^2}\ H_\Theta + k^2 H_\Theta = - \frac{\delta(\rho - \rho')\ \delta(z)}{\rho} \quad , \tag{IV-8}$$

and in the second:

$$\frac{\partial}{\partial\rho} \frac{1}{\rho} \frac{\partial}{\partial\rho}\ \rho\ E_\Theta + \frac{\partial^2}{\partial z^2}\ E_\Theta + k^2 E_\Theta = - \frac{\delta(\rho - \rho')\ \delta(z)}{\rho} \quad , \tag{IV-9}$$

with the boundary conditions on E_Θ (H_Θ) and $\partial/\partial\rho\ \rho\ E_\Theta$ ($1/\epsilon\ \partial/\partial\rho\ \rho\ H_\Theta$) being that of continuity. By representing the field components E_Θ or H_Θ by F, the two equations become identical:

$$\frac{\partial}{\partial\rho} \frac{1}{\rho} \frac{\partial}{\partial\rho}\ \rho\ F + \frac{\partial^2}{\partial z^2}\ F + k^2 F = - \frac{\delta(\rho - \rho')\ \delta(z)}{\rho} \quad . \tag{IV-10}$$

The following transform relationship is used:

$$F = F(\rho,\rho',z) = \frac{1}{2\pi} \int_{-\infty}^{\infty} \psi(\rho,\rho';\xi)\ e^{-j\xi z}\ d\xi \quad , \tag{IV-11}$$

$$\psi(\rho,\rho';\xi) = \int_{-\infty}^{\infty} F(\rho,\rho',z)\ e^{j\xi z}\ dz \quad . \tag{IV-12}$$
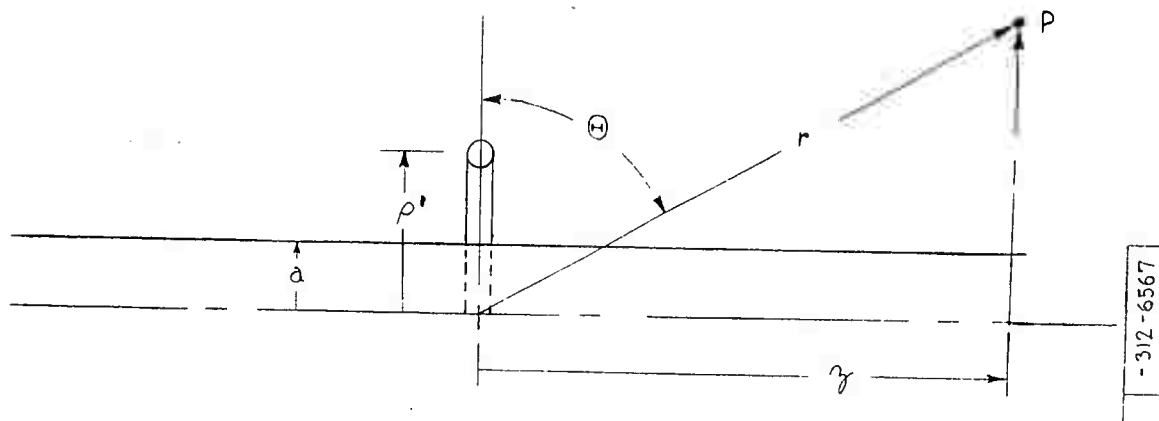
Fig. IV-7. Geometry of far-field determination.

The resultant equation is then:

$$\frac{\partial^2}{\partial \rho^2} \psi + \frac{1}{\rho} \frac{\partial}{\partial \rho} \psi + (\kappa^2 - \frac{1}{\rho^2}) \psi = - \frac{\delta(\rho - \rho')}{\rho} \quad , \qquad \text{(IV-13)}$$

where

$$\kappa^2 = k^2 - \zeta^2 \quad . \qquad \text{(IV-14)}$$

This Green's function problem may be solved with the appropriate boundary conditions yielding an integral equation for the field. Specifically, for TE modes with $\rho' = a$,

$$E_\theta(\rho, z; a) = \frac{1}{2\pi} \int_{-\infty}^{\infty} \frac{1}{\left[\dfrac{w H_0^{(2)}(w)}{H_1^{(2)}(w)} - \dfrac{z J_0(z)}{J_1(z)} \right]} \frac{H_1^{(2)}(\kappa \rho)}{H_1^{(2)}(w)} e^{-j\zeta z} \, d\zeta \quad , \qquad \text{(IV-15)}$$

and for TM modes $\rho' = a$,

$$H_\theta(\rho, z; a) = \frac{1}{2\pi} \int_{-\infty}^{\infty} \frac{1}{\left[\dfrac{w H_0^{(2)}(w)}{H_1^{(2)}(w)} - \dfrac{z J_0(z)}{\epsilon J_1(z)} \right]} \frac{H_1^{(2)}(\kappa \rho)}{H_1^{(2)}(w)} e^{-j\zeta z} \, d\zeta \quad . \qquad \text{(IV-16)}$$

w, z, κ arc defined in the previous report.

These integrals in the complex plane involve residue contributions from poles (leaky waves) and branch cut integrals. As presented, they evaluate the fields everywhere in space, which is wasteful since only the far field is of interest. To this end, the geometry in Fig. IV-7 and the transformations:

$$\kappa = k \cos \varphi \quad ,$$

$$\zeta = k \sin \varphi \quad , \qquad \text{(IV-17)}$$

$$\varphi = \xi + j\eta \quad , \qquad \text{(IV-18)}$$

are used.

From Fig. IV-7:

$$\rho = r \cos \Theta \quad , \tag{IV-19}$$

$$z = r \sin \Theta \quad . \tag{IV-20}$$

If the TE mode integral is used, E_Θ becomes:

$$E_\Theta(r, \Theta; a) = \frac{1}{2\pi} \sqrt{\frac{a}{r \cos \Theta}} \int_C \left\{ \frac{k \cos \varphi \, \exp[jka \cos \psi]}{\dfrac{wH_0^{(2)}(w)}{H_1(w)} - \dfrac{zJ_0(z)}{J_1(z)}} \right\}$$

$$\times \exp[-jkr \cos(\varphi - \Theta)] \, d\varphi \quad , \tag{IV-21}$$

$$E_\Theta(r, \Theta; a) = \frac{1}{2\pi} \sqrt{\frac{a}{r \cos \Theta}} \int_C G(\varphi) \exp[-jkr \cos(\varphi - \Theta)] \, d\varphi \quad . \tag{IV-22}$$

Now a steepest descent technique may be used to evaluate this integral for large kr.

To summarize, a method has been established which places in perspective the role of modes on a cylinder, including leaky waves. These modes determine the poles of the integrand in the representation of the field. The location of the source and its magnitude solely determine the zeros of the integrand.

In evaluating the far field by means of a steepest descent integration, three cases are possible:

(1) Residue terms due to poles of the integrand (leaky waves). It can be shown that these all will attenuate and be negligible in the far field in comparison with the space wave.

(2) With no poles of the integrand near the saddle point $\varphi = \Theta$, the far field is:

$$E_\Theta(r, \Theta; a) = \frac{\exp[jka \cos \Theta]}{\left\{ \dfrac{wH_0^{(2)}(w)}{H_1^{(2)}(w)} - \dfrac{zJ_0(z)}{J_1(z)} \right\}\Bigg|_{\varphi = \Theta}} \sqrt{\left(\frac{a}{\lambda} \cos \Theta\right)} \frac{e^{-jkr}}{r} \quad , \tag{IV-23}$$

and the leaky wave modes affect the far field in a manner analogous to that in which poles of a network determine its steady-state response to a single frequency.

(3) If a pole of the integrand is near the saddle point $\varphi = \Theta$, a modified method of integration indicates a strong lobe in the direction $\Theta = \operatorname{Re} \varphi_0$, where φ_0 is the pole location (Ref. 1, pp. 503-506):

$$E_\Theta = \frac{g(\varphi_0)}{(\varphi_0 - \Theta)} \frac{e^{-jkr}}{r} \quad . \tag{IV-24}$$

The mode equations:

$$\frac{wH_0^{(2)}(w)}{H_1^{(2)}(w)} = z \frac{J_0(z)}{J_1(z)} \quad , \quad (TE) \tag{IV-25}$$

$$\frac{wH_0^{(2)}(w)}{H_1^{(2)}(w)} = z \frac{J_0(z)}{\epsilon J_1(z)} \quad , \quad (TM) \tag{IV-26}$$

and restraint:

$$w^2 - z^2 = (ka\overline{f}_p)^2 \tag{IV-27}$$

have been solved for complex w and z using asymptotic expansions of the functions. Specifically:

$$w = jz \cot(z - \pi/4) \quad , \quad (TE) \tag{IV-28}$$

$$\epsilon w = jz \cot(z - \pi/4) \quad . \quad (TM) \tag{IV-29}$$

When solutions are known in the z-plane, ζ may be found from:

$$(\zeta/k)^2 = \sin^2 \varphi = \epsilon - z^2/(ka)^2 \tag{IV-30}$$

and the results finally presented in the φ-plane. It is possible to show that if (z, w) form a solution, then so do $(-z, w)$ and $(z^*, -w^*)$. This implies a

symmetry in the φ-plane about the origin and about the line $|\operatorname{Re}\varphi| = \pi/2$.
Computer programs for these calculations have been prepared. Shown in
Fig. IV-8 through IV-13 are the results for TE_{01}, TE_{05}, TE_{0-1}, TE_{0-5}, TM_{01},
TM_{0-1} modes.

The mode numbers employed require explanation. The first subscript
refers to the angular variation, as is conventional. However, the variable r
is assimilated into the variable z. In the z-plane, solutions of the mode equa-
tion occur in strips:

$$\frac{4m-1}{4}\pi \leqslant x \leqslant \frac{4m+1}{4}\pi \quad , \quad m = 1, 2, 3 \ldots \quad ,$$

$$\frac{4m+1}{4}\pi \leqslant x \leqslant \frac{4m+3}{4}\pi \quad , \quad m = -1, -2, -3 \ldots \quad .$$

The second mode number is m, and may take on both positive and negative
values; e.g., $TE_{om}\big|_{m=-1}$ or TE_{0-1}. These graphs indicate that only for
$0 < \epsilon < 1$, i.e., $\bar{f}_p^{\,2} < 1$, and for ka large will the steepest descent integration
yield lobes in an off-axis direction. These lobes will be in the direction

$$\Theta = \sin^{-1}\sqrt{\epsilon} \quad . \tag{IV-31}$$

This fact follows from the previous argument that only when a pole of the inte-
grand in the field expansion falls near the saddle point will there be a contri-
bution to the far field. In the graphs shown, it can be seen that only for the
range of parameters mentioned does this occur. As the root locus approaches
the real axis of the φ-plane, ka$\to\infty$ and z remains finite. Thus $\sin^2\varphi\to\epsilon$ and
the lobe direction dependence on ϵ is found. The lowest-order modes are
most significant, i.e., TE_{01} rather than TE_{05}. This points out an inherent
fault of the calculation. Inasmuch as asymptotic forms have been employed,
a region of small z and w has been neglected which may be most significant.

In Fig. IV-8 through IV-11, LSDP indicates the limiting steepest descent
path; that path to be used in the integration where $\Theta = \pi/2$. For $0 < \Theta < \pi/2$,
the steepest descent path lies to the left of the LSDP.

In conclusion, therefore, it is now felt that the initial task in the investi-
gation of scattering from plasma trails on the basis of normal modes has been
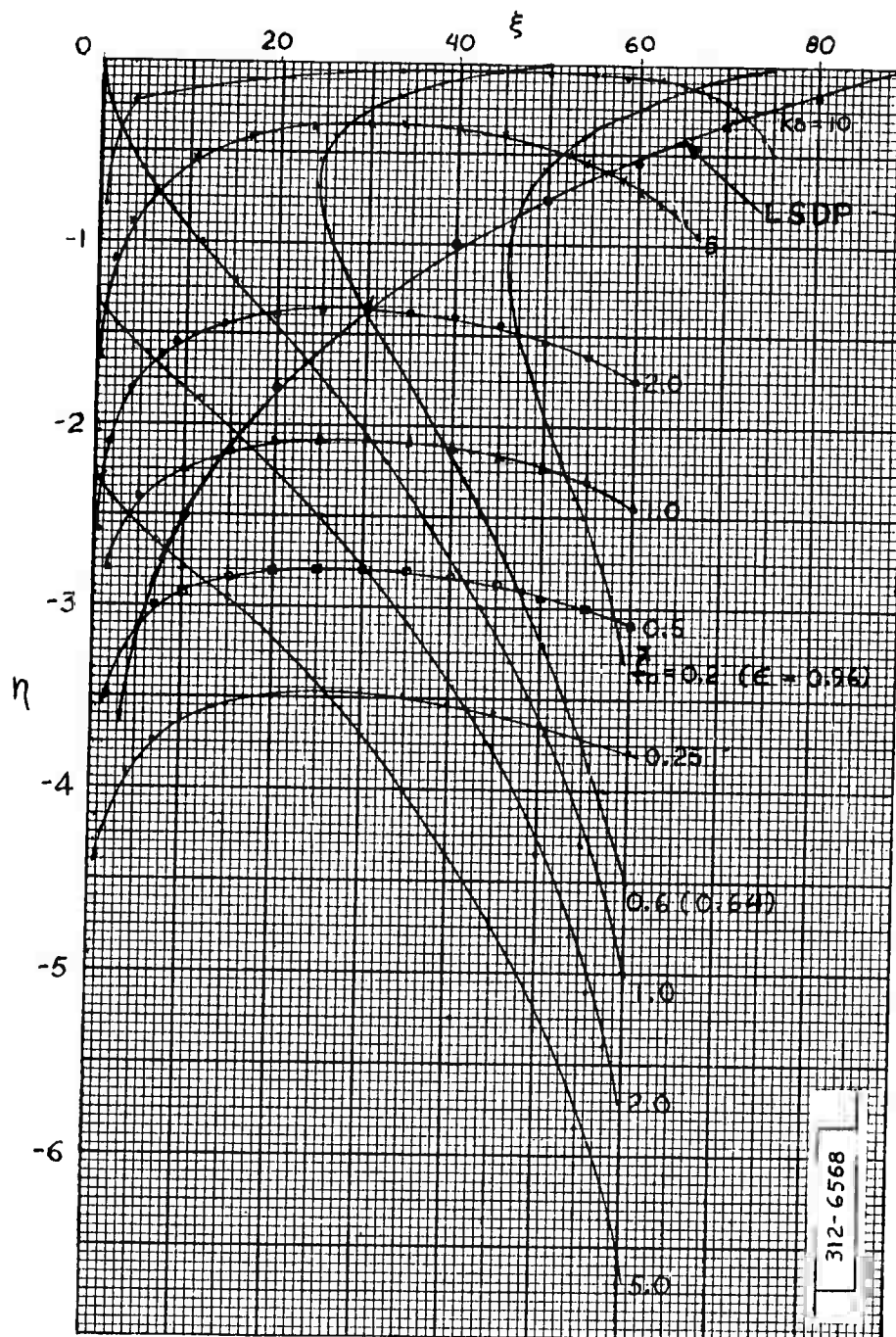
Fig. IV-8. Root loci of TE_{01} mode.
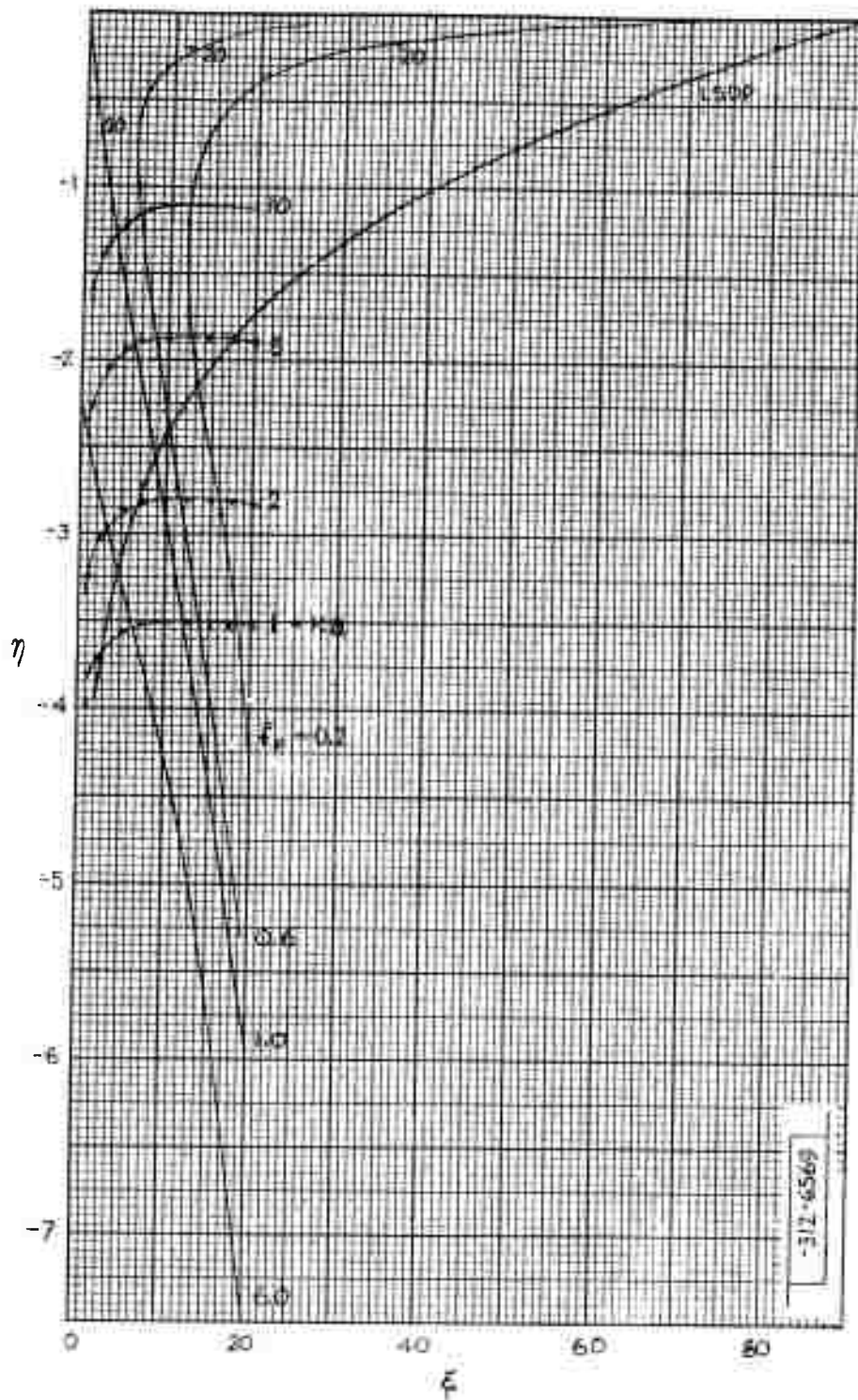
Fig. IV-9. Root loci of TE_{05} mode.
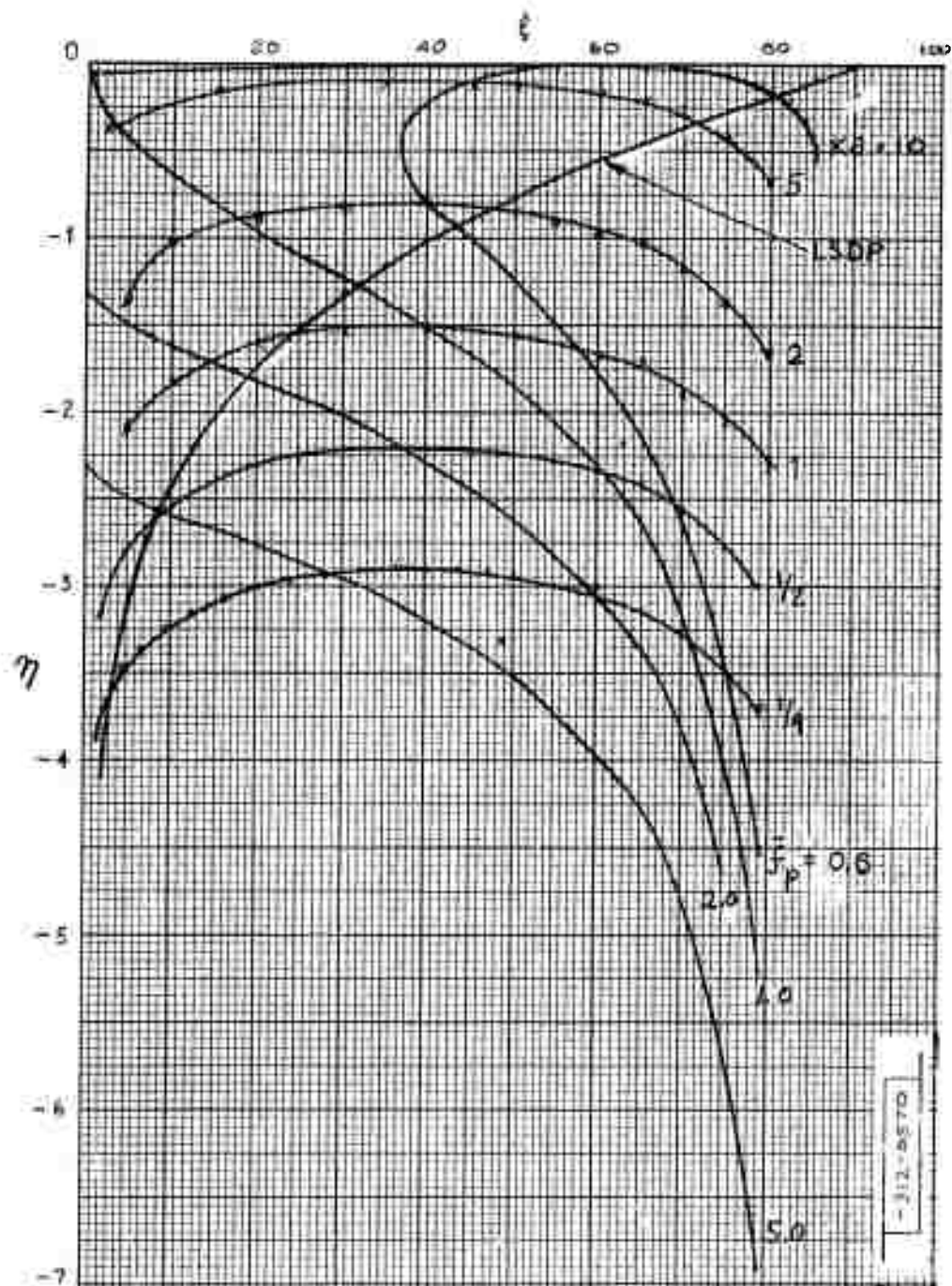
Fig. IV-10. Root loci of TE_{0-1} mode.
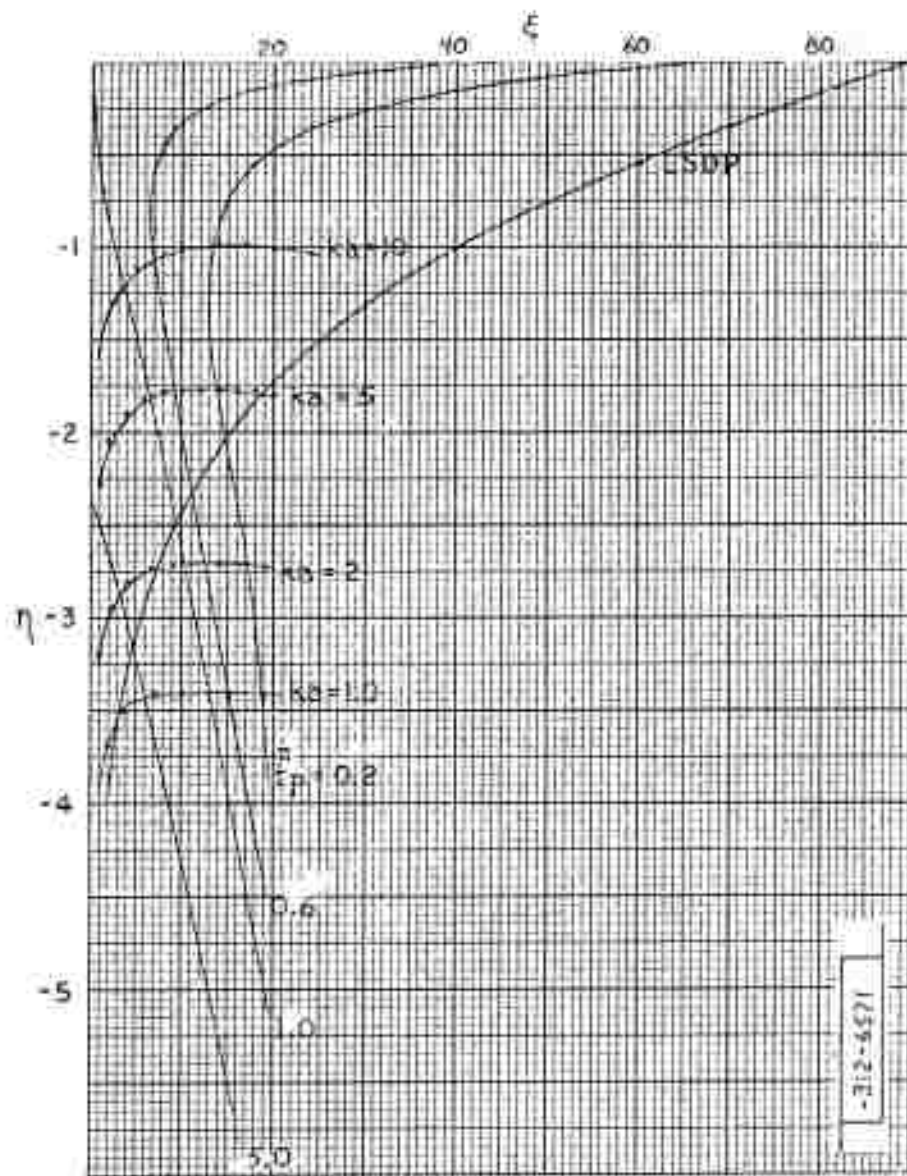
Fig. IV-11. Root loci of TE_{0-5} mode.
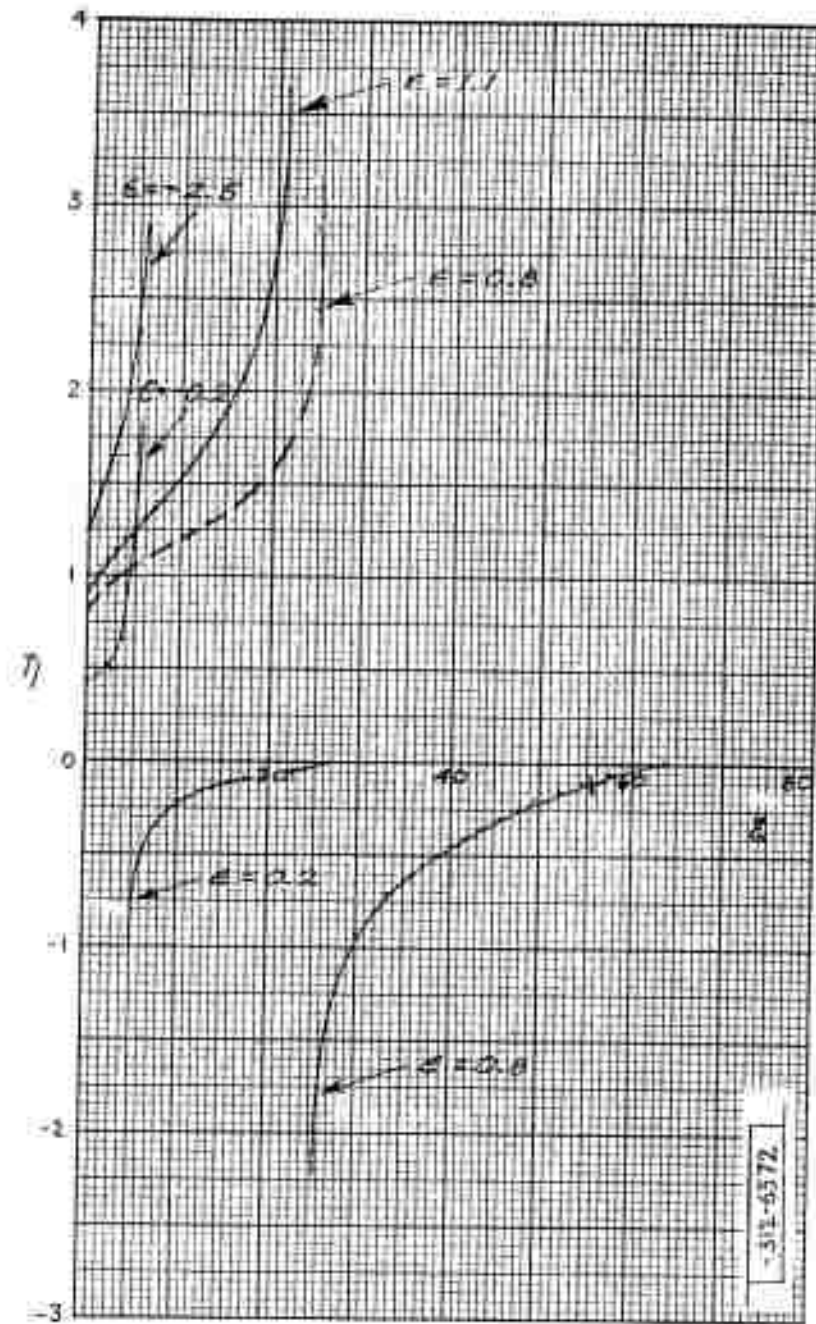
Fig. IV-12. Root loci of TM_{01} mode.
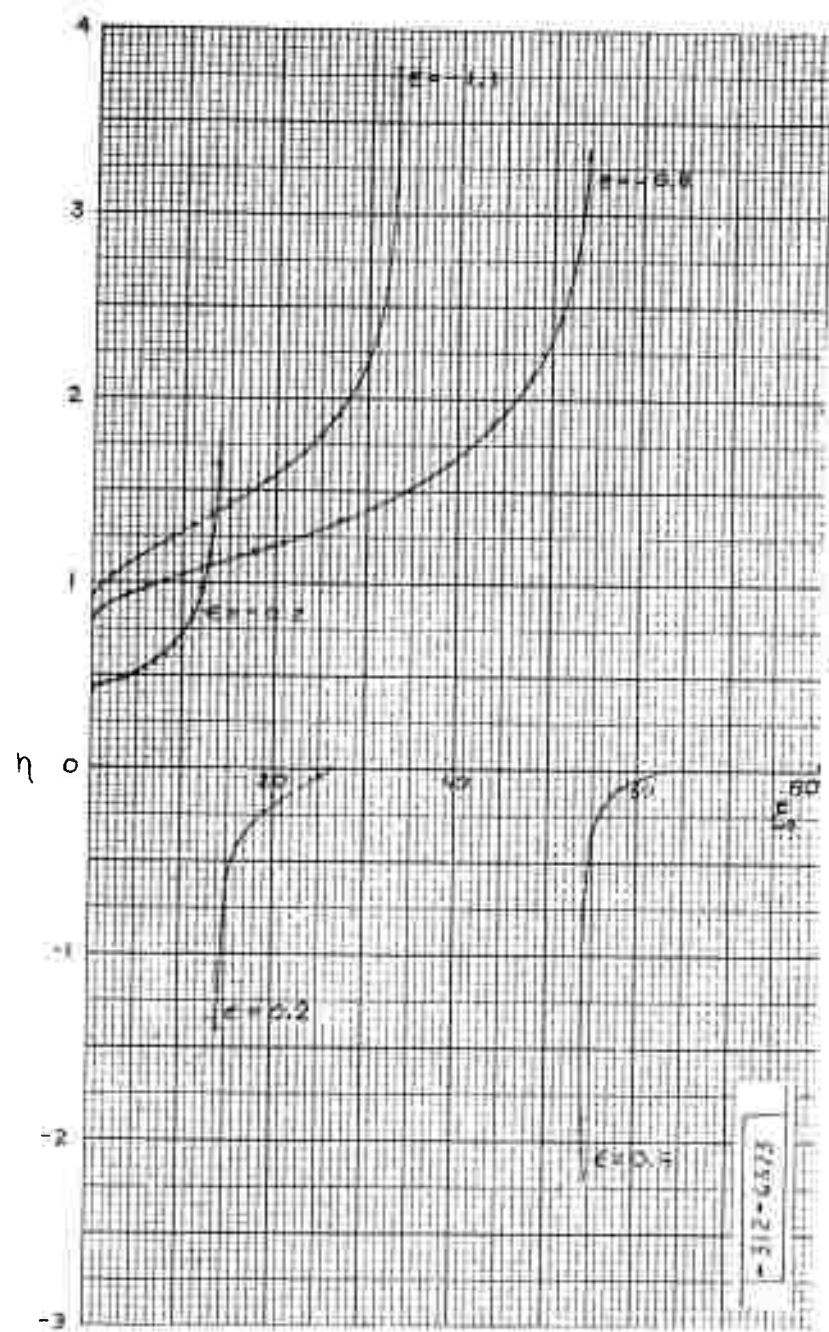
Fig. IV-13. Root loci of TM_{0-1} mode.

completed. An attack on the problem has involved many approximations:

   (1) Infinite-length cylinders, and ring sources of current,

   (2) Circular symmetry,

   (3) Lossless, homogeneous, cylindrical plasmas,

   (4) Asymptotic expansions of Bessel functions.

The results obtained can be of use in a qualitative study of scattering phenomenon.

REFERENCES

1. R. E. Collin, <u>Field Theory of Guided Waves</u>, (McGraw-Hill, New York, 1960), pp. 485-506.

2. T. Tamir, "Leaky Wave Contributions to the Field of a Line Source Above a Plasma Slab," Report PIBMRI-845-60, Contract No. AF-19(604)-2031, Microwave Research Institute, Polytechnic Institute of Brooklyn.

F. SCATTERING FROM AN INFINITE CYLINDER HAVING A RADIALLY VARYING DIELECTRIC CONSTANT

In its original form, the program written to calculate reflection and transmission from a cylinder having a dielectric constant which varies as a cubic presented difficulties that made it necessary to change and essentially rewrite the program.

As set up at present, the program determines transmission and reflection coefficients and their phases for an infinite cylinder having a dielectric constant of the form:

$$\epsilon(\overline{r}) = \epsilon_r(\overline{r}) + i \, \epsilon_i(\overline{r}) = b_0 + b_2 \overline{r}^2 + b_4 \overline{r}^4 + b_6 \overline{r}^6 \quad, \tag{IV-32}$$

where $\overline{r}$ is the ratio of the radial distance to the wavelength of the incident radiation.

The complex coefficients $b_n = b_{nr} + i \, b_{ni}$; $n = 0, 2, 4, 6$, and $\overline{a}$, the ratio of the radius of the cylinder to the wavelength of the incident radiation are input values. The symbol b_0 specifies the value of the dielectric constant and hence of the electron density at the center of the cylinder. The remaining coefficients are chosen so that successive derivatives of $\epsilon(\overline{r})$ at the origin are positive or zero and so that:
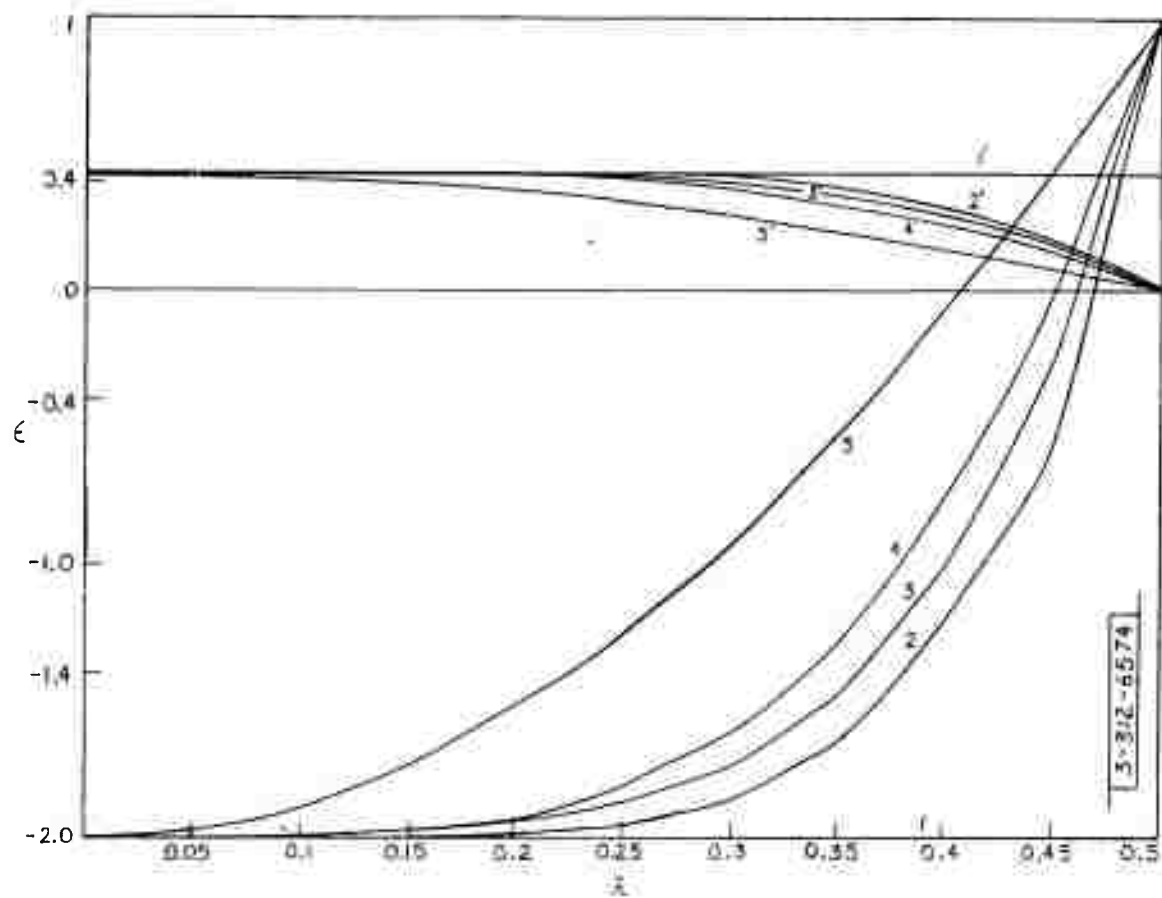
Fig. IV-14. Radial variations in electron density.

$$b_{or} + b_{2r}\,\overline{a}^2 + b_{4r}\,\overline{a}^4 + b_{6r}\,\overline{a}^6 = 1 \quad , \tag{IV-33}$$

$$b_{oi} + b_{2i}\,\overline{a}^2 + b_{4i}\,\overline{a}^4 + b_{6i}\,\overline{a}^6 = 0 \quad . \tag{IV-34}$$

That is, so that $\epsilon(\overline{a}) = 1 =$ free-space dielectric constant. However, various combinations of coefficients satisfying the above requirements will give different values for the real and imaginary parts of the dielectric constant as a function of $\overline{r}$ for every given b_o and $\overline{a}$.

Figure IV-14 shows a set of curves for which $b_o = -2 + 0.43448399i$ and $\overline{a} = 0.5$. The curves 1 to 5 each represent the real part of the dielectric constant as a function of $\overline{r}$ for a specific set of values of b_{2r}, b_{4r}, and b_{6r}. The curves 1' to 5' each represent the corresponding imaginary parts of the dielectric constant as a function of $\overline{r}$, where in this case it has been assumed that the collision frequency is a constant. The results given by the program for these dielectric constants are shown in Table IV-2. Here TM, PTM, RM, and PRM are defined as in the homogeneous cylinder program discussed in previous semiannual reports. Curves 1 and 1' simply represent a homogeneous cylinder of dielectric constant $\epsilon = -2 + 0.43448399i$ and radius-to-wavelength ratio $\overline{a} = 0.5$. The results given by the program for this case were found to be in agreement with the results given by the homogeneous cylinder program.

For low electron densities, the results given by the program were compared with results obtained by assuming the electrons to scatter independently. It was found that for values of $b_o = 0.6$ and 0.9 and $\overline{a} = 0.5$ there is a discrepancy of 37.9 per cent and 23.6 per cent, respectively, between the values given by the program and those given by calculating electron scattering. However, for a value of $b_o = 0.99$ this is reduced to 1.39 per cent.

G. SCATTERING FROM CONCENTRIC PLASMA SHELLS

Considerable effort has been expended to check out and expand the usefulness of the concentric sphere program as described in the Semiannual Report of 30 June 1960, pp. 37-38. In particular, roundoff difficulties were found in the calculation of Neumann functions by recursion whenever the imaginary part

TABLE IV-2

SCATTERING FROM A RADIALLY VARYING PLASMA CYLINDER

1. $\epsilon_r = -2$

2. $\epsilon_r = -2 + 192\,\overline{r}^{-6}$

" 3. $\epsilon_r = -2 + \overline{r}^{-2} + 10\,\overline{r}^{-4} + 136\,\overline{r}^{-6}$

4. $\epsilon_r = -2 + 48\,\overline{r}^{-4}$

5. $\epsilon_r = -2 + 12\,\overline{r}^{-2}$

1'. $\epsilon_i = 0.43448399$

2'. $\epsilon_i = 0.43448399 - 27.807\,\overline{r}^{-6}$

3'. $\epsilon_i = 0.43448399 - 0.144828\,\overline{r}^{-2}$
$\qquad - 1.44828\,\overline{r}^{-4} - 19.6966\,\overline{r}^{-6}$

4'. $\epsilon_i = 0.43448399 - 6.95174\,\overline{r}^{-4}$

5'. $\epsilon_i = 0.43448399 - 1.73793\,\overline{r}^{-2}$

Real and Imaginary Parts of Dielectric Constant	TM	PTM	RM	PRM
1 and 1'	23.96087	155.0867	1.668822	299.8364
2 and 2'	19.84831	156.5699	1.395096	336.386
3 and 3'	19.44292	156.7823	1.352350	340.6649
4 and 4'	18.75388	157.1403	1.292402	347.7251
5 and 5'	16.57882	158.6688	1.056290	13.12430

of the argument increased to five. Replacement of the recursion relationship by a Wronskian, and introduction of a few other modifications now permits most cases to be processed where $\left| 2\pi(a/\lambda)\,\sqrt{\epsilon} \right| < 35$. However, there seems to be some places where the matrices to be inverted become ill-conditioned. These regions are being investigated.

Provisions to plot, on the Benson-Lehner machine, curves of $\log_{10}(\sigma/\pi a^2)$ vs $\log_{10}(a/\lambda)$ have been incorporated into the program.

Runs have been made using either a metallic or a dielectric center sphere and up to five concentric shells. In particular, runs corresponding to the physical conditions pertaining in Trailblazer Ib have been made. These results are being analyzed.

V. THE EXPERIMENTAL PROGRAM AT WALLOPS ISLAND

A. OPTICAL EQUIPMENT PROGRAM

The Optical Laboratory on Katahdin Hill was first occupied by Lincoln Laboratory personnel in March 1961. Electronic and optical equipment pertaining to the 48-inch tracking and spectrometric telescope have been moved into the Optical Laboratory. The state of progress is described in the following sections.

1. 48-Inch Tracking and Spectrometric Telescope

The 48-inch base pedestal, mount, primary mirror and servo control electronics have been installed and have been undergoing testing and alignment. Initial tests indicate that the mechanical deflection specifications have been exceeded, and hence the boresight requirement has been realized. The servo performance of the mount has been measured, and a mechanical resonance has been found which appears to be in the pedestal base.

The objective has been to decrease the static tracking error to within one second of arc while maintaining an acquisition time of approximately one-tenth second. To this end, considerable mechanical, hydraulic, and electronic redesign has been performed during the past six months. During this period, the static tracking error has been decreased to approximately 20 seconds of arc, and considerable improvement is expected through the use of an improved hydraulic valve design and electronic compensation networks.

2. Electronics for Readout of Photomultiplier Information from Spectrometer

The visible spectrometer for the 48-inch telescope requires that the incident light level from 0.3 micron to 0.6 micron be measured at 30 discrete wavelengths. The system must have a dynamic range of 10^6 with an accuracy of 1 to 2 per cent. The system must be capable of recording a lower light level equivalent to 5 to 10 quanta per second. The system as finally determined measures the pulse output from photomultiplier tubes rather than the current.

By counting the pulse outputs of the photomultiplier tubes, the response or recovery of the system, particularly at very low light levels, is made superior to any technique involving a measurement of the current output. The spectrometer photoelectric readout circuits require a photomultiplier which produces a short output pulse per photoelectron at the photocathode and a high current gain at the anode. The 1P21 photomultipliers initially designed into the spectrograph did not exhibit the necessary gain and exhibited an excessive spreading of the pulse. The EMI 14-stage photomultipliers have the desired characteristics.

For the above reasons, the photomultiplier assembly on the spectrograph has been redesigned to utilize the EMI 14-stage multipliers. The system is presently arranged so that each of the 30 photomultipliers representing 30 wavelengths and their respective counters count for 94 msec and then record in 6 msec Under these conditions, a sample of the light level at each wavelength occurs every 0.1 sec.

By cooling the photomultipliers, the dark count (due to noise) is approximately one count or less per second. An upper value for the count at a maximum light level is 10^6 per sec and is limited by the space charge of the tube. The linearity of the count per second vs the light level appears to be about 1 per cent. An accurate measurement of the light level may prove this to be an optimistic number but, in any case, the count per second vs light level curves can be standardized on all the 30 photomultiplier tubes. Repeatability of measurements so far has been excellent, and recovery of the tubes from a high count to a low count is very rapid and within the requirements of the system.

Each of the 30 photomultiplier-counter circuits has 17 stages with the necessary timing and output circuitry. The output from each counter is in proper form for recording on magnetic tape; in addition, each counter operates a common ladder network that provides a visual (scope) indication of the count at each timing interval. The over-all system excluding the photomultipliers requires a volume of about 6 cubic feet and about 60 watts of input power.

The timing section, one complete counter and the ladder network are operating satisfactorily at present. The remainder of the system (29 additional counters and associated circuitry) is on order and will be received by 15 July.

The complete system will be operational in August. Several photomultiplier tubes have been checked thus far and have the proper characteristics. Accurate measurements of the photomultiplier characteristics at particular wavelengths will be completed shortly.

3. 12-Inch Radiometer

A change in the detector of the total-radiation radiometer from a Golay Cell to a copper-doped germanium type of diode is planned. Problems in design involve the helium-nitrogen cooling system and special reflector optics.

4. Optical Radiation Standards

Two cavity-type black-body radiators, eight calibrated tungsten ribbon lamps and various spectral-type lamps have been purchased and are planned for use in calibrating the 48-inch spectrometer, radiometer and associated equipment. Recording equipment for the radiometer consists of a Brush twin-channel recorder. An absolute quantitative calibration procedure has been initiated and is under development.

5. Electronics for Readout of Infrared Information from Spectrometer

The spectrometer has been provided with 10 lead sulphide (PbS) cells with which the IR portion of the spectrum is to be analyzed. These cells are suitable for detecting infrared energy out to 2.6 microns; however, to extend their range to 4.0 microns, a cooling scheme will have to be arranged.

Figure V-1 shows the basic block diagram of the electronics for converting the electrical analog signal from the output of the IR cell into digital form. Basically, the system consists of a stage of low-noise amplification followed by a pseudo-logarithmic amplifier. The output of the log amplifier is rectified, and this DC signal is then used to modulate the frequency of a variable-frequency oscillator in such a way that the instantaneous frequency of the oscillator is proportional to the logarithm of the energy incident upon a given IR cell. This frequency is then converted into digital form by a multistage binary counter. The digital output of this counter is then recorded on digital tape suitable for
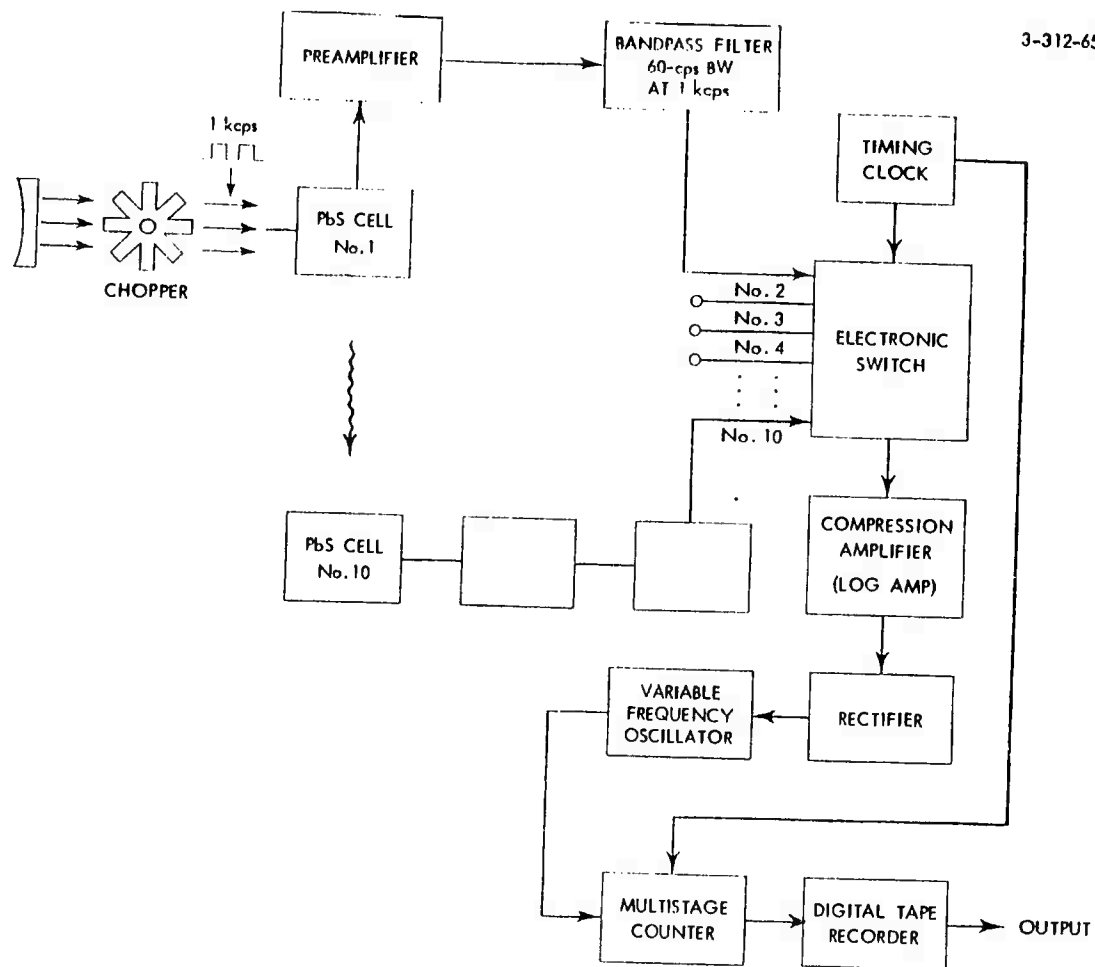
Fig. V-1. Block diagram of IR cell electronic readout.

computer processing   In the proposed system, a suitable electronic switching scheme requires the use of only one counter.   However, this is incidental to the basic operation of the system and is therefore not shown.

Of primary concern in this system is its sensitivity. A cursory examination revealed that the maximum infrared energy incident upon the PbS detector used with the 48-inch telescope (at a wavelength of 1 micron through a 1-micron window whose bandwidth is 0.25 micron) from a 15-inch steel sphere at 2500°K at a range of 100 miles was about 4.7×10^{-7} watts. The specifications provided with the PbS cells indicate that the sensitivity of these cells (N. E. P.) is 5.29×10^{-10} watts   These results lead one to believe that the dynamic range of 10^6 (120 db) is not going to be required with the present PbS detectors. As a result, the emphasis has been placed on minimum detectability rather than dynamic range   This has necessitated research into the design of low-noise, high-gain preamplifiers   To date, a transistorized preamplifier has been designed having an equivalent input noise voltage of about $0.2\,\mu$volt (rms) in a bandwidth of 85 cps at 1 kcps   This corresponds approximately to the minimum rms voltage signal at the output of a typical PbS detector

In summary, a prototype of the digital portion of the electronics for the IR cell readout has been designed and subjected to a series of tests which have proved satisfactory   The preamplifier has also been subjected to tests which have indicated that it will suffice as a low-noise amplifier for the existing IR PbS detectors. The infrared spectrometer design is being studied to increase the detectivity by reduction in cell area and by cooling the cells   The use of arsenic trisulfide fiber optics looks promising for this purpose.

B. RADAR EQUIPMENT PROGRAM

1   S-Band Monopulse Conversion and Coherent Data Channel

The present S-band conical-scan tracking system is being converted to monopulse to provide a modulation-free data channel through which both pulse-to-pulse amplitude and phase measurements can be made. In addition, a coherent klystron modified FPS-18 transmitter with 0.2-μsec to 1.5-μsec pulse capability will be added through the sum channel. The lower-powered coherent system will be capable of seeing the 5-inch sphere only during the reentry phase.

Therefore, the present 4.5-Mw magnetron system will be utilized for tracking the vehicle throughout its entire trajectory. In order to prevent interference with the tracker, the coherent system will be separated in both time and frequency from the tracking radar. Figure V-2 is a preliminary block diagram for the entire system. Figure V-3 shows the entire UHF system as it is presently operating

Transmission of long and short pulses (alternate 6- and 1-μsec pulses) is obtained by switching a 30-Mcps crystal oscillator which is mixed with a crystal local oscillator to obtain the pulsed RF drive. Several systems were attempted to obtain the alternate drive; however, the use of the balanced mixer, tuned amplifier and filter provided the maximum isolation from the local oscillator and other spurious signals in the RF driver. The short pulses are variable from 0.4 to 1.5 μsec, the long, from 3 to 7 μsec. The present system is operating with 1-μsec pulses which will be decreased when the driver chain is broadbanded. The short pulses have been incorporated to obtain more range resolution and to provide more detail in the reentry wake. Each pulse is recorded on continuously moving 35-mm film as outlined in a previous report.

The orthogonal receiving system has been installed in the UHF radar to observe any depolarization effects from the turbulent wake. The horizontal component is obtained by a matched dipole located in the UHF horn. Considerable effort was put into the elimination of voltage breakdown from spurious modes in the UHF horn due to the X-band waveguide running through the center of the horn The present dipole assembly has been tested at 10 Mw peak power without breakdown

Both the vertical and horizontal channels contain parametric amplifiers designed by Blake and McCurley of Group 46 The parametric is an up-converter of which the upper side band is mixed in an LEL orthomode C-band mixer with a portion of the pump added to the local oscillator. This provides a 30-Mcps output which is used in the data-recording system. The parametric amplifier has operated with a noise figure of 1.5 db using MA 450H silicon varactors. The instantaneous bandwidth is 10 Mcps with an average gain at 30 Mcps of 55 db.

In order to match the transmitted pulse, the receiving system is switched from the driver-chain gate generator. The bandwidth is switched from 250 kcps
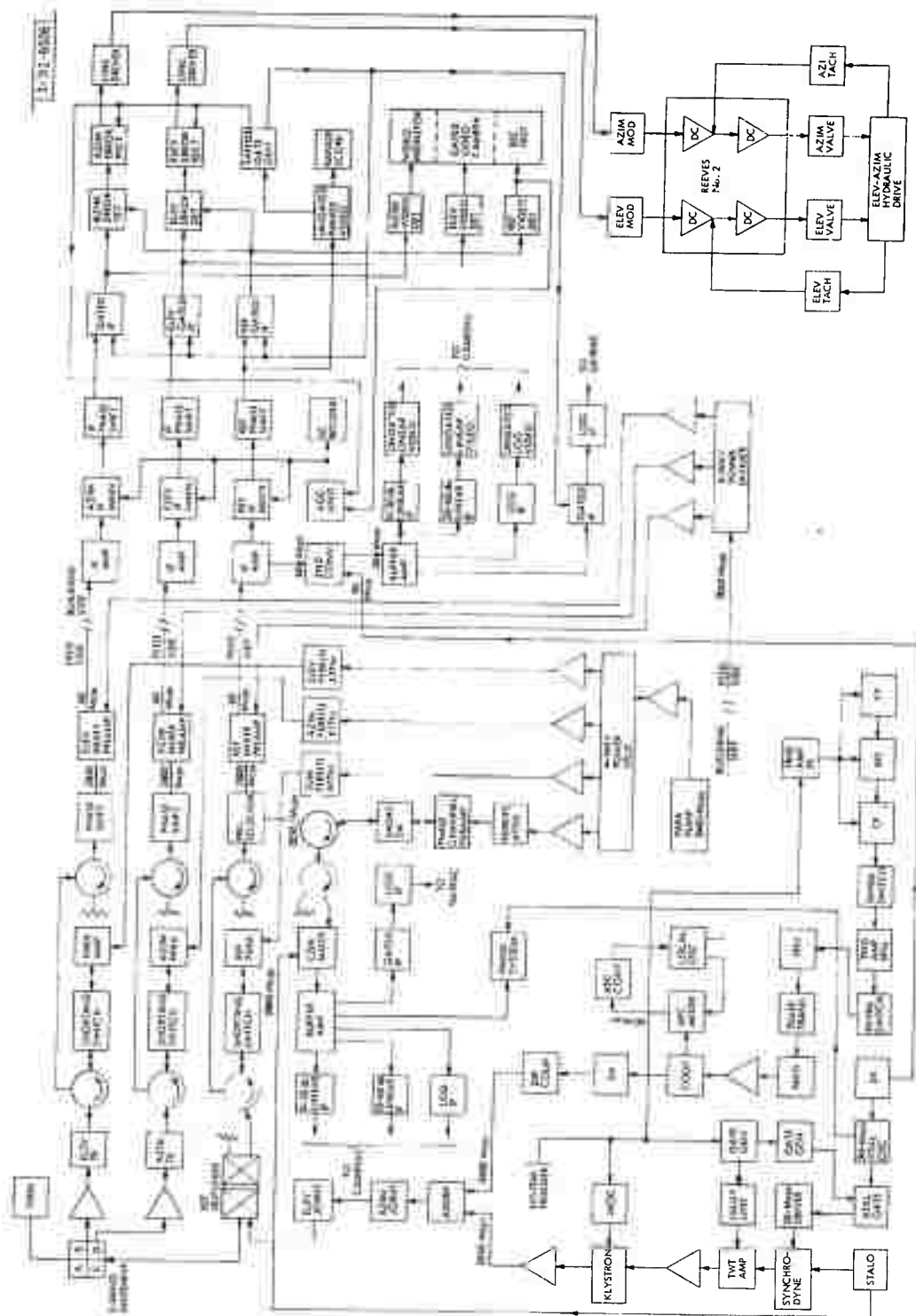
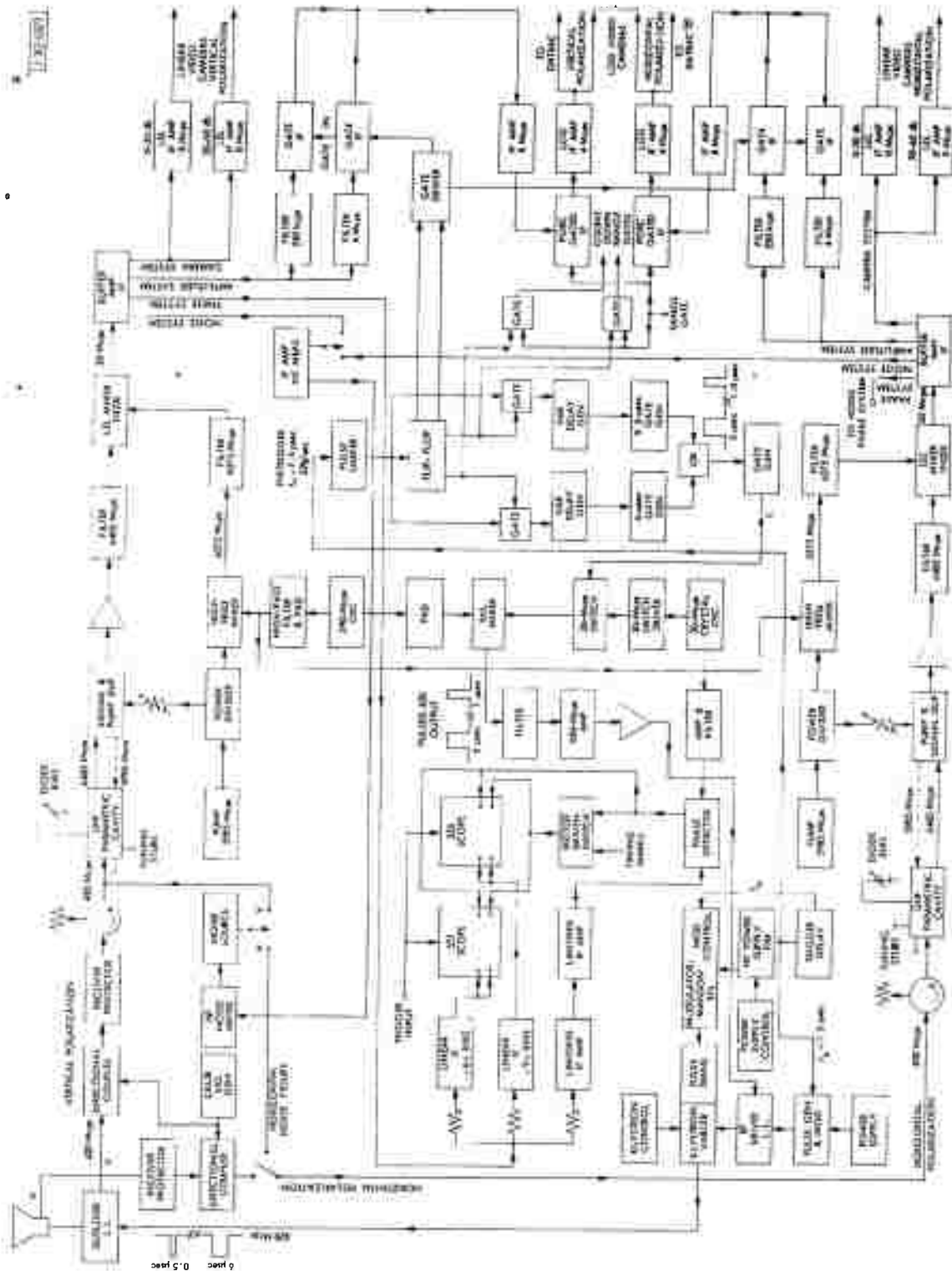Fig. V-2. Wallops Island S-band monopulse and coherent data channel.

Fig. V-3. Wallops Island UHF radar system.

V-8

to 4 Mcps synchronously with the transmitted pulse. In addition, new log IF amplifiers and gated IF amplifiers have been built and installed with 6-Mcps bandwidth to handle the short pulses.

The UHF radar has been made fully coherent by the addition of a stable local oscillator and a 30-Mcps oscillator for the system coherent reference. The output of a 30-Mcps phase detector is recorded on 35-mm film.

The X-band/UHF dual frequency antenna on Tower A was built for slaving to the S-band tracking antenna. Antenna position information (azimuth and elevation) was obtained from the S-band antenna, recorded, and used in the data reduction and analysis. At times, there have been questions as to whether or not the dual-frequency antenna was pointing where the azimuth and elevation data channels in the S-band tracker indicated. This pointing uncertainty has been corrected by the installation of azimuth and elevation shaft encoders on the dual-frequency mount, gear boxes, buffer amplifiers, shift registers, etc., to provide two channels which are identical to the azimuth and elevation channels on the S-band tracker,[*] including printout on the Anelex printer and recording on the primary tape recorder.

Mechanical stops have been installed on the elevation axis of the dual-frequency antenna mount. These are behind hydraulic buffers previously installed.

C. TRAILBLAZER II INSTRUMENTATION PROGRAM

The reentry research vehicle, Trailblazer II, is composed of four stages. The first two stages, a Sergeant and a Lance, are up-firing types. The final stages, an ABL X-248 and the reentry payload, are down-firing. The reentry payload is powered by a 15-inch spherical motor which propels the payload instrumentation and nose cone into the atmosphere at a velocity greater than 20 kilofeet per second.

---

[*] "Reentry Physics Program Semiannual Technical Summary Report to the Advanced Research Projects Agency," Lincoln Laboratory, M.I.T. (31 December 1959), ASTIA 234627, H-127.
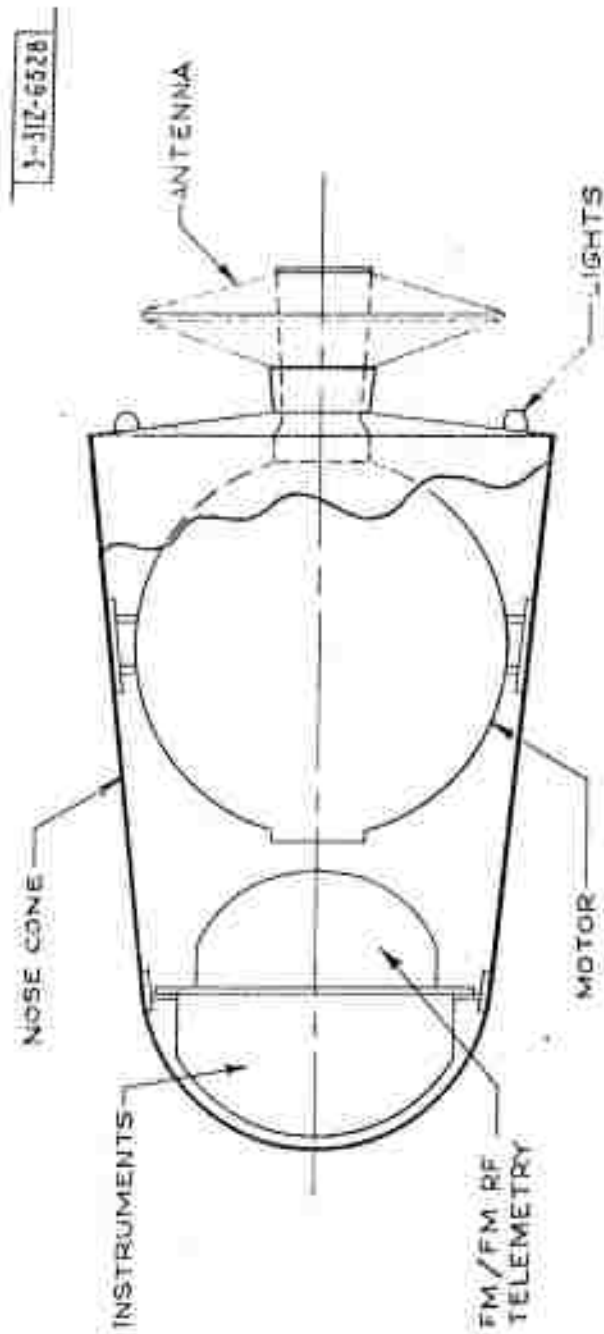
Fig. V-4. Payload for Trailblazer II, shot 1.

Labels: ANTENNA, LIGHTS, NOSE CONE, MOTOR, INSTRUMENTS, FM/FM RF TELEMETRY

3-JIZ-6528

In general, the reentry payload comprises:

(1) Measuring instruments,
(2) Standard 244.3-Mcps FM/FM telemetry system,
(3) Optical flashing-light telemetry system,
(4) Antennas for both telemetry systems,
(5) Reentry nose cone,
(6) 15-inch spherical motor.

The exact composition of the final stage will vary with the experiments. The 15-inch motor is a special unit designed by NASA Langley. The General Electric Company is designing and building the nose cone.

Figure V-4 shows the general layout of the reentry package. For the first Trailblazer II shot, the instrumentation consists of gyros and accelerometers which will give information as to vehicle stability. The optical telemetry system will provide a means of receiving information from the pitch gyro through the reentry period when the RF telemetry is subject to blackout. In addition to the stability measurements, the RF telemetry antenna impedance will be measured.

A block diagram of the RF telemetry is shown in Fig. V-5. For simplicity of design, a DC all solid state system is being used. This system follows closely the telemetry standards of the Inter-Range Instrumentation group. Meaningful signals from the Trailblazer II RF telemetry are receivable on any standard FM/FM telemetry ground station which has the discriminators required for the detection of IRIG channels 10 through 15.

As shown in Fig. V-4, the RF telemetry antenna serves also as a light reflector for the optical telemetry. The antenna, a modified disc cone arrangement, has satisfactory directivity and coverage patterns. Because the payload telemetry antenna is completely enclosed in a metallic shell during a portion of the flight, RF and optical signal reception is limited. A means to transmit the payload signals during the up-firing stages has been devised and will be tested during the next report period.

The basic components of the telemetry system, the subcarrier oscillators, the mixing network, the power supply and the transmitter are all commercial units. The remainder of the components are specially built items. Two complete ground stations, one for the Wallops Island Field Station and one for
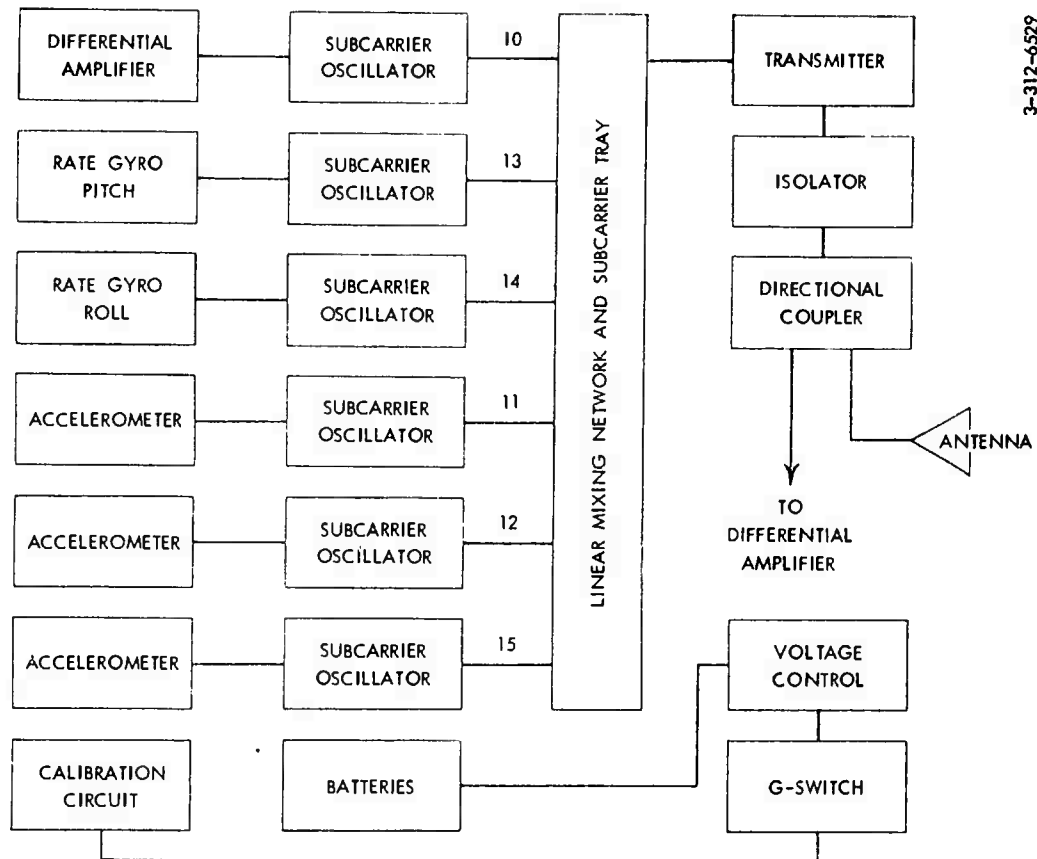
Fig. V-5. FM/FM telemetry system.

general laboratory use, along with auxiliary test equipment are being procured. These stations will be put into operation during the next report period.

Also during the next report period, the instrumentation package for Trailblazer II, shot one, will be built. Design and construction for future shots is in the planning stage.

D. WALLOPS ISLAND DATA

Trailblazer If (D58-3077) was fired from Wallops Island, Virginia on 17 January 1961 at 23h 00m 00s; Trailblazer Ig (D58-3132) on 21 April 1961 at 00h 56m 20.0s, and Trailblazer Ih (D58-3133) on 18 May 1961 at 01h 10m 00s, all EST. Trailblazer Ii (D58-3138) is scheduled for the week of 11 July 1961. The Lincoln Laboratory Millstone Hill radar participates in these shoots.

1. Trailblazer If

The sixth stage of the Trailblazer If was tracked through separation and a reentry was observed by the S-band tracker and the UHF radar located at the Arbuckle Neck site. The sixth stage consisted of a 5-inch spherical rocket motor equipped with a copper shell. This reentry body, shown in Fig. V-6, had a burnt-out weight of 2.001 pounds.

A map plot of the trajectory is shown in Fig. V-7. The ascending trajectory was observed at an azimuth of 145.5° from the S-band tracker. The sixth-stage trajectory lay in an almost due north plane, and the reentry event was observed at an azimuth of 90° from the tracker. The resulting reentry angle was 60.7° measured from the horizontal. This departure from the intended flight trajectory was the most extreme yet observed and is believed to have been due to a large angle precession of the velocity package during the ascending trajectory.

This extreme and unexpected reentry trajectory was responsible for the poor optical data, since it was impossible to reposition the Super Schmidt cameras in time to observe the reentry.

One ballistic camera operated by NASA at the Fentress station recorded a reentry trace at the extreme edge of the film. This trace was of poor photographic quality with some evidence of camera vibration due to repositioning of the camera.

RADIO
BEACON
TRANSMITTER

MAGNESIUM NOZZLE

FORMICA RING

GLASS LAMINATE

CARBON NOZZLE INSERT

2.5 RADIUS

COPPER HEAT SHIELD

J-112-6530
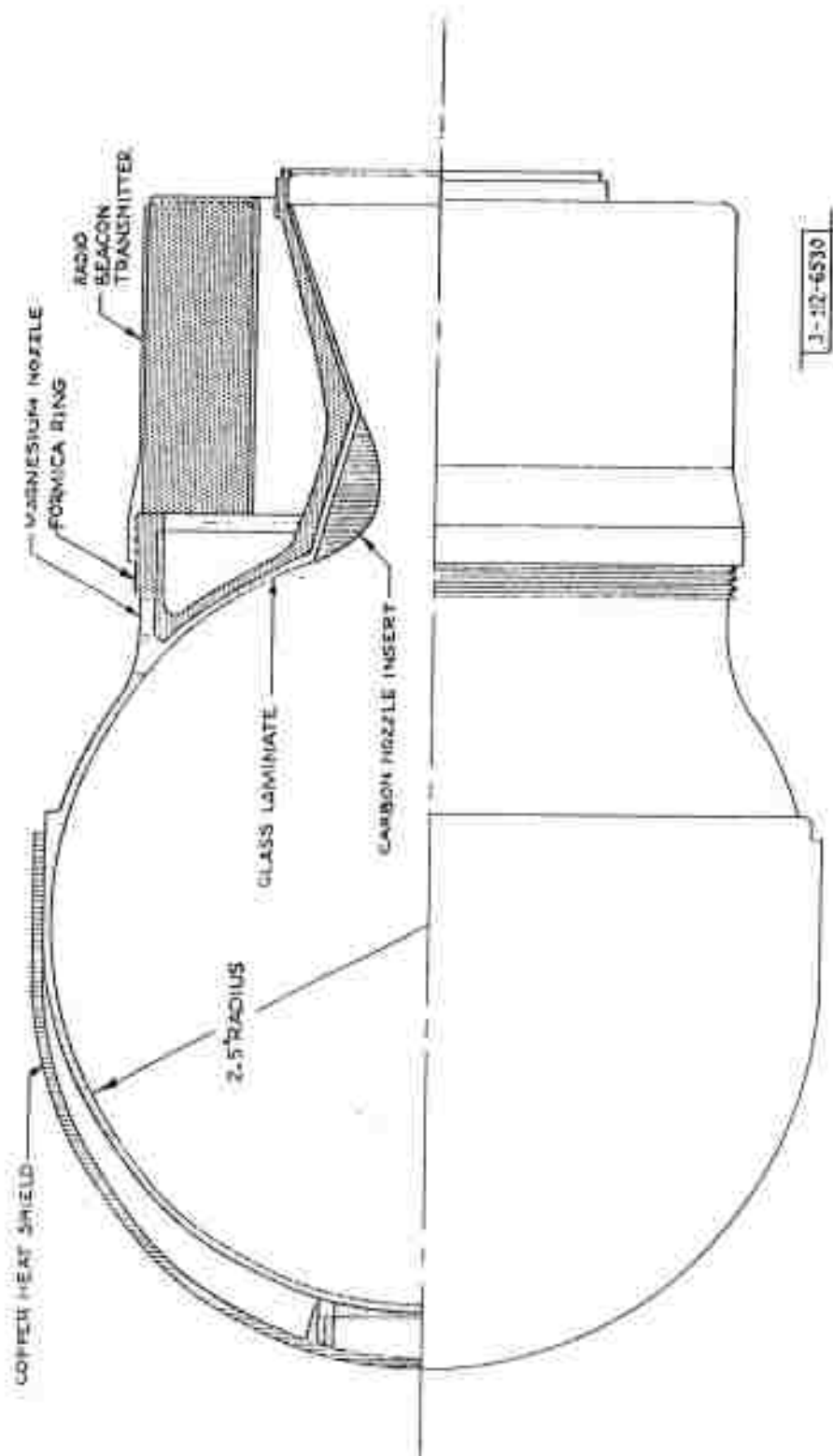
Fig. V-6. Detail drawing of Trailblazer If sixth-stage reentry body (5-inch diameter spherical rocket motor) equipped with copper heat shield.
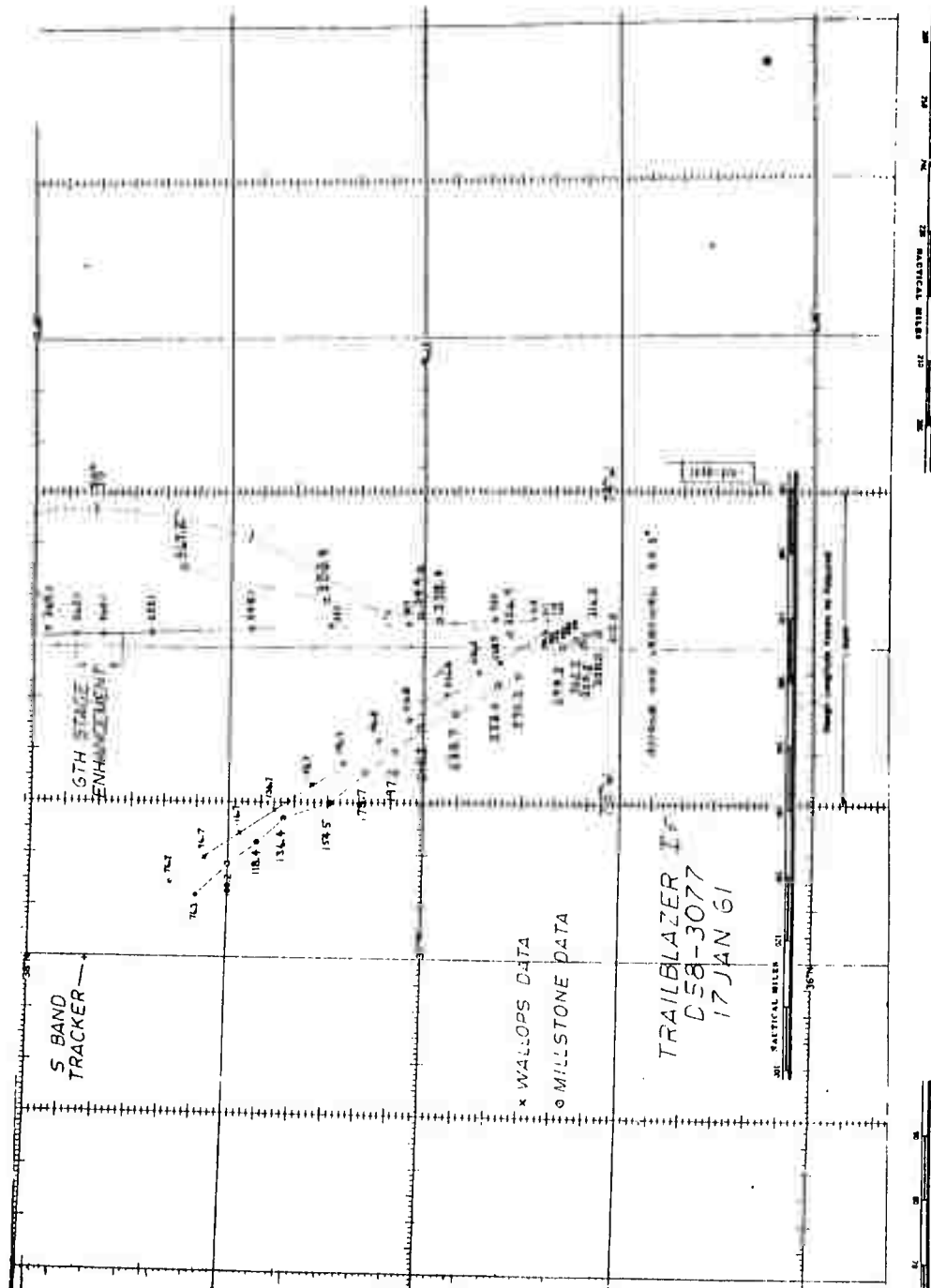
V-14

Fig. V-7. Map plot of trajectory of Trailblazer If. Data derived from Wallops Island S-band tracker indicated by crosses. Agreement over ascending trajectory is within the uncertainty of the transformed Millstone data (indicated by circles).

The S-band tracking data are presented in Figs. V-8 and V-9. Figure V-8 is a plot of sixth-stage velocity as a function of height. Figure V-9 is a plot of the pulse-by-pulse cross section seen by the S-band tracking radar prior to and during enhancement.

It is evident from Fig. V-9 that the target was lost at about 364.5 seconds after T_o corresponding to an altitude of about 110,000 feet. The velocity-vs-height plot in Fig. V-8 indicates that the servo system of the S-band tracker did not follow the reentry deceleration of the sixth stage. This has been verified by a study of the elevation, azimuth and range performance of the radar which indicated that the antenna was coasting after approximately 362 seconds. The trajectory data thus are not usable below about 130,000 feet altitude.

A trajectory reduction was accomplished by Dr. R. E. McCrosky of Harvard University, using the single available trail photograph in combination with S-band radar position data. The velocity was determined from the camera shutter breaks. This has been plotted as an "optical" reduction in Fig. V-8. These data show a somewhat more rapid deceleration than the radar data alone. However, this reduction is somewhat questionable due to the poor quality of the photograph and the difficulty of establishing an exact time coincidence between the radar and the optical event.

The S-band cross section results shown in Fig. V-9 were plotted on a pulse-by-pulse basis at the rate of 320 pulses per second. It is evident that before enhancement the data show a spread of about 4 db. This is about the expected amplitude for the 30-cycle scanning modulation (due to the conical scan) during a satisfactory track with the S-band instrument. The theoretical radar cross section of a 5-inch metal sphere at the S-band frequency of 2790 Mcps is about 17.2 db below one square meter.

A strong enhancement of 30 to 35 db is observed beginning at about 190,000 or 185,000 feet altitude with some indication of slight earlier activity present. The duration of the observed enhancement at S-band is about 5 seconds terminating at an altitude of about 125,000 feet. The validity of these data below approximately 130,000 feet is open to question due to the tracking difficulties during deceleration, as discussed above. There is a marked increase in the fluctuation of the data during enhancement.
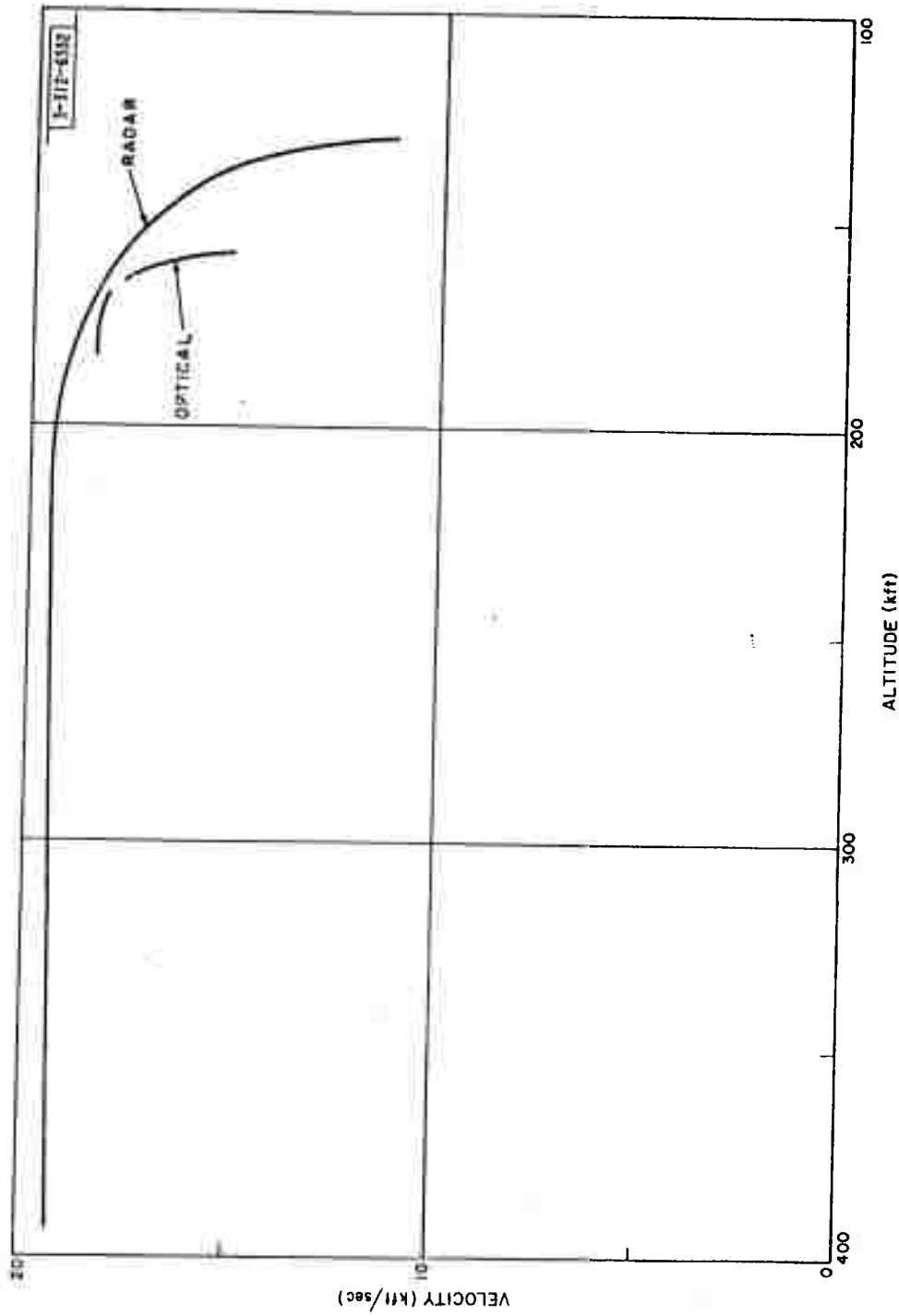
Fig. V-8. Trailblazer II f radar and optical velocities vs height. Optical data reduced from NASA ballistic camera plate. Radar data reduced from Wallops Island S-band tracker data.
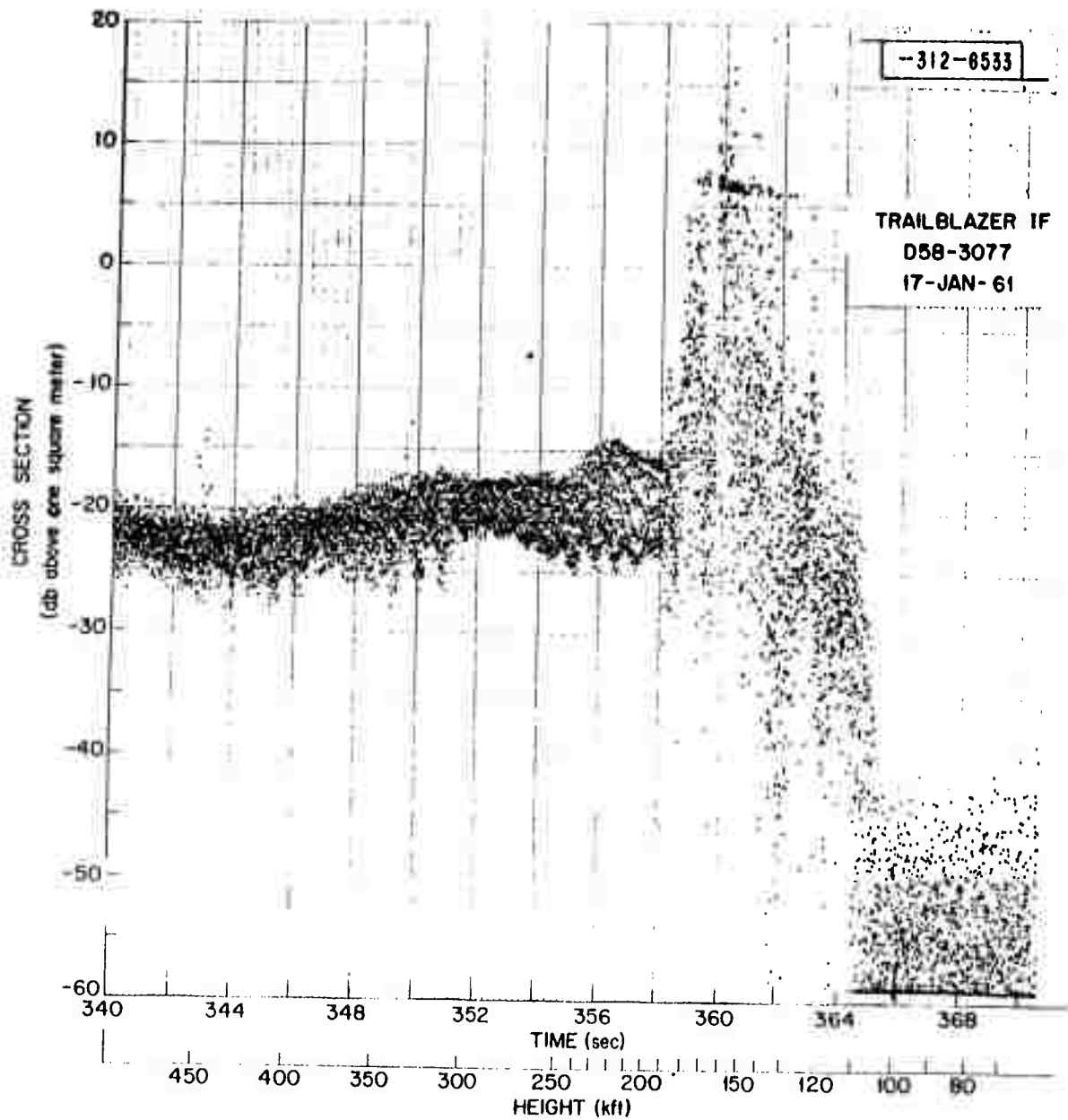
Fig. V-9. Trailblazer If S-band radar cross section vs time and height.
Pulse-by-pulse data plotted at 320 points per second.

UHF enhancement was obtained for this reentry. Unfortunately, the UHF digitalizing equipment malfunctioned, and the data were arbitrarily quantized in approximately 5-db steps. Radar film was read to recover some of the details of the pulse-by-pulse data. The envelope of the UHF pulse-by-pulse data is shown in Fig. V-10. UHF enhancement amounts to about 35 db. The major rise in cross section takes place at the same altitude as the large increase in S-band cross section, but the increase in measured cross section is definitely more rapid at UHF. The UHF enhancement also appears to have a greater duration than the S-band cross section, lasting until about 120,000 feet altitude. When the tracking behavior is considered, this duration could perhaps be attributed to the greater beamwidth of the UHF system.

Similar radar results were obtained on previous shots. The physical significance of these results was discussed in Sec. H, Chap. IV, of the previous semiannual report (31 December 1960) and in a paper (No. 61-40) presented by G. F. Pippert and S. Edelberg during the annual meeting (23 January 1961) of the Institute of Aerospace Sciences.

No satisfactory X-band data were obtained on this test.

2. Trailblazer Ig

The Ig reentry package illustrated in Fig. V-11 was a modified aluminum 5-inch spherical rocket motor. A shaped charge carried by this sixth stage in the cylindrical nose extension was ignited at about 760,000 feet altitude (T_o + 325 sec) to propel a steel pellet approximately 3/32 inch thick and 1/2 inch in diameter downward at high velocity. This pellet or "artificial meteor" has been designated as the seventh stage. The shaped charge-pellet package was provided by the Geophysics Research Directorate of the Air Force Electronic Systems Division.

The Ig vehicle was acquired by the S-band tracker, and a track of the ascending trajectory was obtained at an azimuth of about 152.5°. The sixth stage (the 5-inch sphere carrying the shaped charge) was briefly observed by the S-band tracker immediately after firing. Unfortunately, the radar was unable to hold the sixth-stage target. The track was lost, and the radar did not observe the reentry.
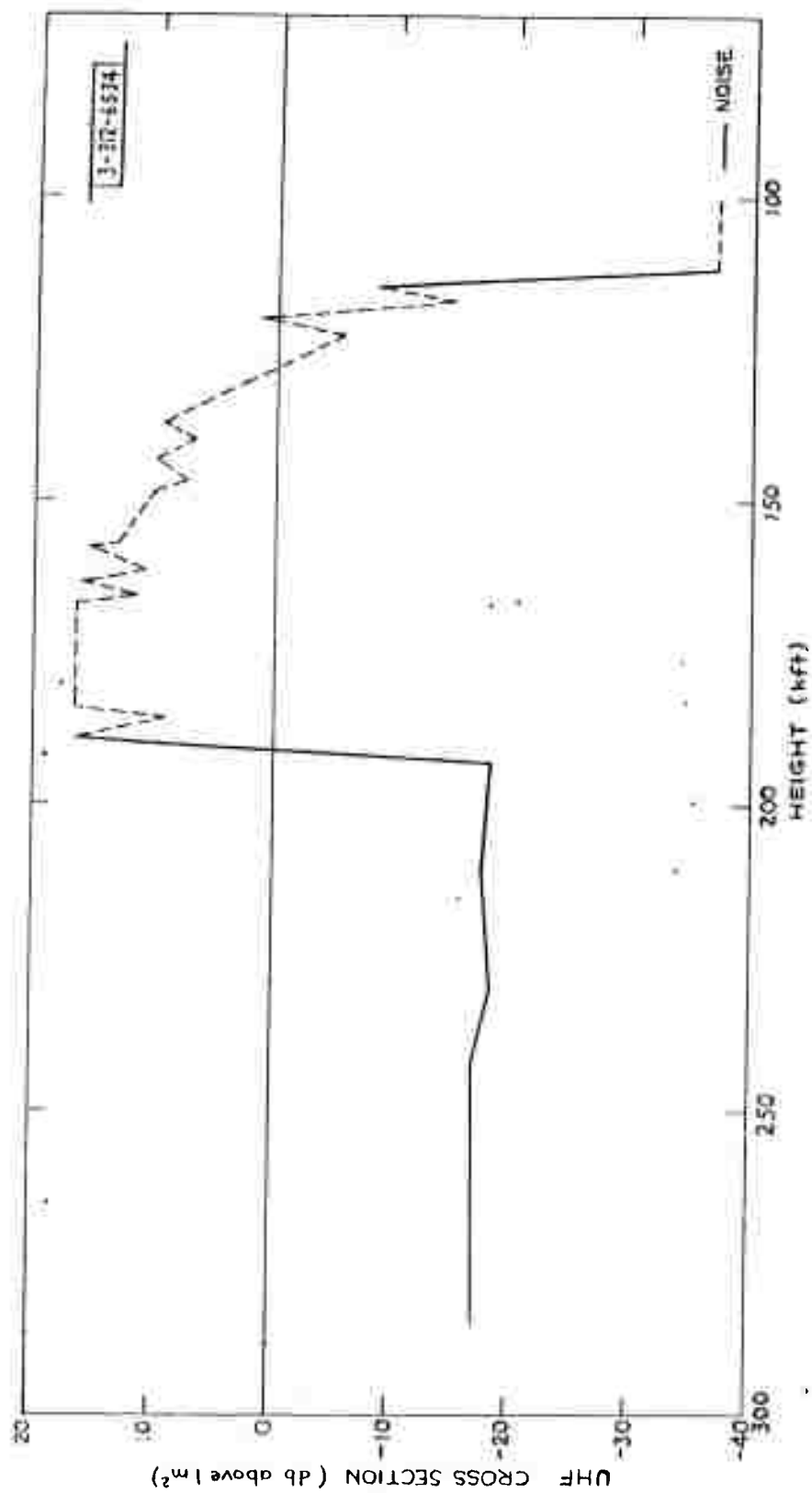
Fig. V-10. Trailblazer If UHF radar cross section vs height. This envelope reconstructed from poor quality digital pulse-by-pulse data and some pulse-by-pulse film records.

V-20

5-312-6535

1.500-20N, CL. 3 THD.

.250 ± .002

10" LONG, MAX. LENGTH FOR 25 SECOND DELAY
6.75" LONG, APPROX FOR MIN. ACCEPTABLE DELAY OF 10 SECONDS

3 No. 18 ANNEALED COPPER, NYLON AND GLASS COVERED WIRE 24" LONG EQUALLY SPACED TAPE AND POT.

75 ST ALUM AL CONTAINER

PROJECTILE

140 G PBX CHARGE

25 G TETETYL BOOSTER

25 SEC. DELAY BLASTING CAP

2 TO 4 lb/ft² ECCOCAST
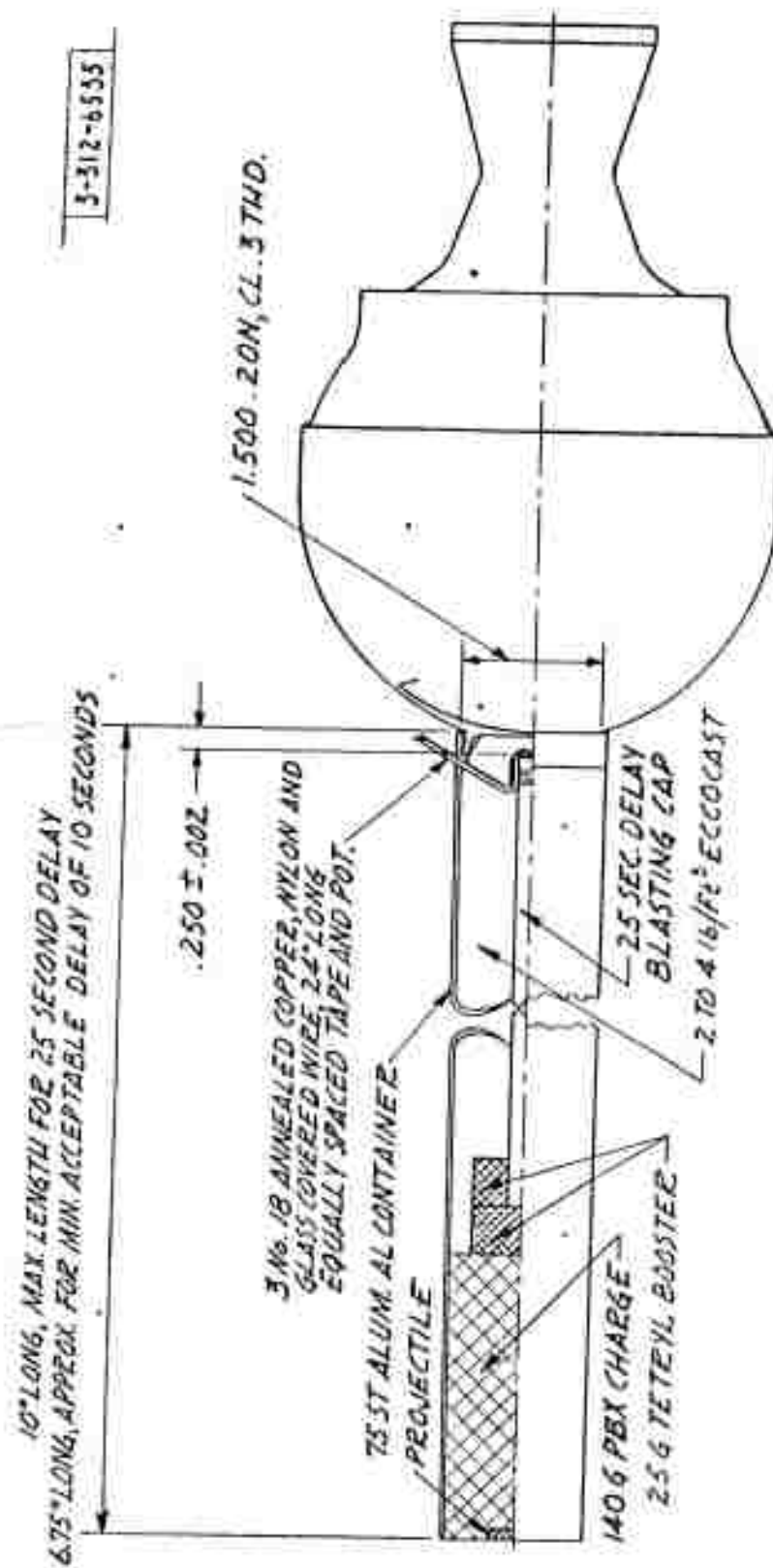
Fig. V-11. Drawing of Trailblazer Ig seventh-stage reentry projectile and shaped charge mounted on 5-inch diameter sixth-stage spherical rocket motor.
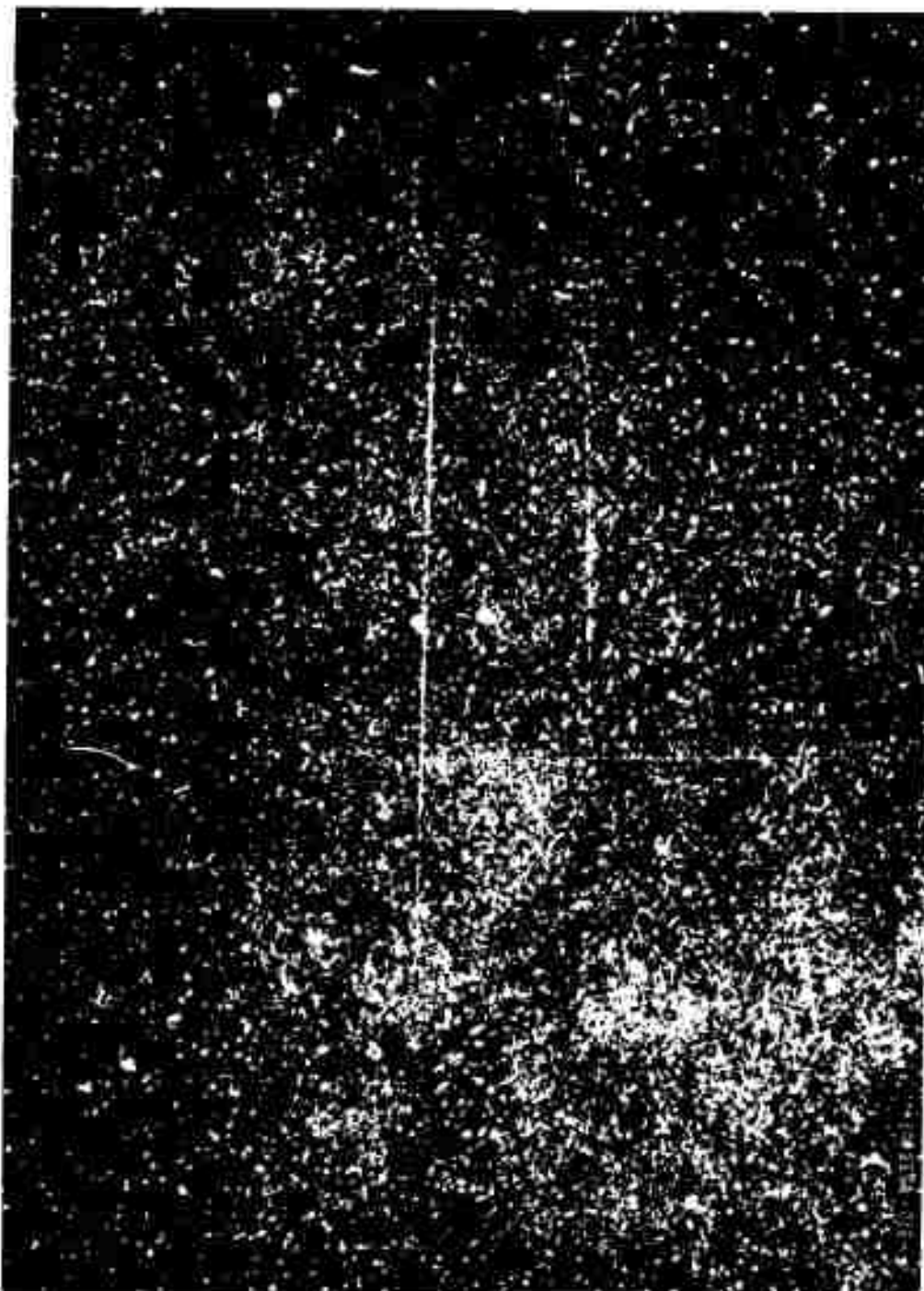
Fig. V-12(a). Wallops Island Super Schmidt photograph of Trailblazer Ig sixth- and seventh-stage reentries. Shorter trace is seventh stage. Super Schmidt meteor camera has aperture of f/0.83 and 8-inch focal length. Film is blue sensitive Kodak x-ray type, premolded to a spherical focal plane. Exposure was approximately 60 seconds, and a rotating shutter, operating in the focal plane, gave 10 shutter breaks per second.

Fig. V-12(b). Eastville Super Schmidt photograph of Trailblazer Ig. Shorter trace is seventh stage. Camera and conditions as given for Fig. V-12(a) except for location and shutter rate of 15 breaks per second.

V-23

Fig. V-13. Trailblazer Ig preliminary optical reduction of velocity vs height for sixth- and seventh-stage reentries.

The sixth and seventh stages were observed by the Super Schmidt cameras located at Arbuckle Neck and at the new Super Schmidt location at Eastville, Virginia, which is approximately 40 miles south of Arbuckle Neck. These reentries were also successfully observed by NASA ballistic cameras at Coquina Beach, North Carolina. The Super Schmidt photographs from the Arbuckle Neck and Eastville sites are shown in Figs. V-12(a) and (b).

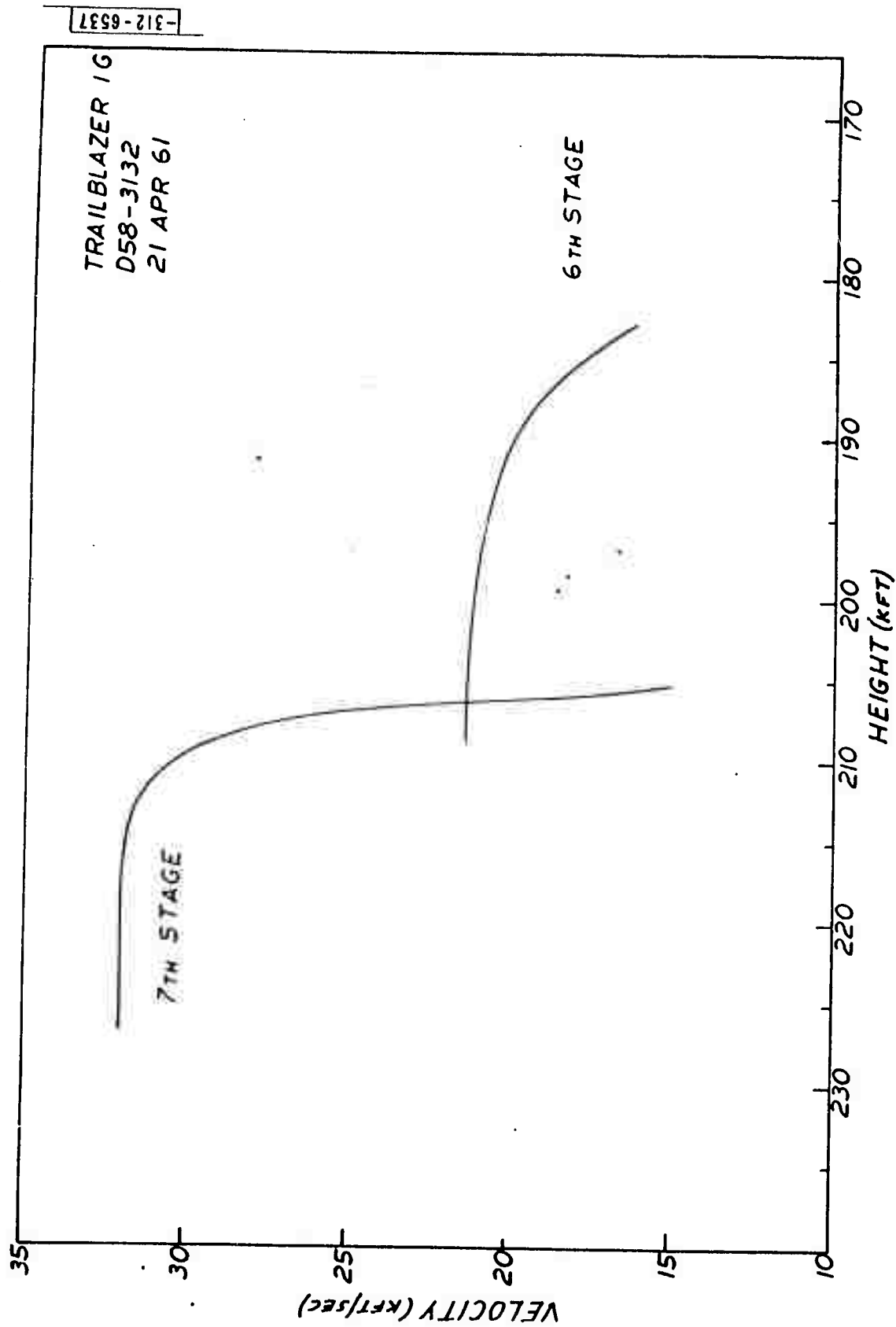A preliminary optical reduction based upon the Super Schmidt photograph from Arbuckle Neck and a ballistic plate obtained by NASA (Fig. V-13) indicates a velocity at reentry of about 21,400 ft/sec for the sixth stage and about 32,100 ft/sec for the seventh stage pellet.

A further reduction using the Super Schmidt photograph from the Eastville site will be accomplished upon completion of the necessary survey of that site. Luminosity studies of the photographic traces of the sixth and seventh stages are in process.

3. Trailblazer Ih

The Ih reentry body was a spherical rocket motor made of iron. As in the Ig event, the sixth stage was briefly observed by the S-band tracker immediately after firing. However, a reentry track was not obtained.

The optical reentry was recorded by the Super Schmidt camera at the Arbuckle Neck site. A photograph of this reentry is shown in Fig. V-14. A reduction of these data is not yet complete.

4. Millstone Hill Data

A new Doppler analyzer display was installed at the Lincoln Laboratory Millstone Hill site at Westford, Massachusetts. This device provides a real-time display of the Doppler velocity and the signal amplitude for multiple targets present in the radar beam and allows identification of the three final stages of the vehicle system upon firing. This display can be used to manually control the position of a Doppler frequency tracking system which should insure that the desired target is subsequently tracked.

For the If event, the Millstone radar observed the sixth stage after firing. The frequency tracker was unable to lock on the sixth stage but subsequently

Fig. V-14. Wallops Island Super Schmidt photograph of Trailblazer Ih
sixth-stage reentry. Camera and conditions as given for Fig. V-12(a)
except for shutter rate of 30 breaks per second.

acquired and tracked the fifth stage. This track, however, was broken off and the antenna lowered in an unsuccessful attempt to observe the sixth stage passing through the beam.

In the Ig event, the Millstone radar again observed the sixth stage but was unable to acquire this target due to a very weak signal. Fifth stage was acquired by the Doppler tracking system, and the Millstone radar observed the fifth stage reentry which saturated its recording system during a portion of that reentry. Peak enhancement amounted to at least 30 db. Due to the large beamwidth of the Millstone radar, it is difficult to assign altitudes to this observation with precision. Optimum utilization of Millstone radar data will be achieved when coincident reentry data on a single target are obtained by both Millstone Hill and Wallops Island radars.

An attempt to acquire the sixth stage of Trailblazer Ih using the Doppler analyzer display was unsuccessful due to a weak sixth-stage Doppler signal.

5. Fourier Analysis of Wallops Island Radar Data

A 7090 monitor program has been written to Fourier analyze selected portions of radar cross-sectional data as seen by the Wallops Island radar. Cross sections in dbm as a function of time are read in from a high-density binary tape, which was previously prepared by the basic Wallops Island program. Up to 9600 consecutive points for each of three radars can be processed where each point may or may not have been averaged. The output consists of a histogram, a cumulative distribution function as a function of db, and the amplitude and phase of the Fourier coefficients as a function of frequency.

6. Coherent Radar Measurements

Equipment has been added to the UHF radar by G. R. Armstrong and J. P. Perry of Group 47 which records the echo pulse amplitude shape and pulse phase shape. Figure V-15 is a block diagram of the equipment. The IF waveform is amplified in three channels. Two of these employ linear amplifiers, the gains of which are adjusted so that, together, an approximately linear dynamic range of 60 db is obtained. The envelope-detected outputs are presented alternately on vertically displaced delayed A-scope sweeps of the
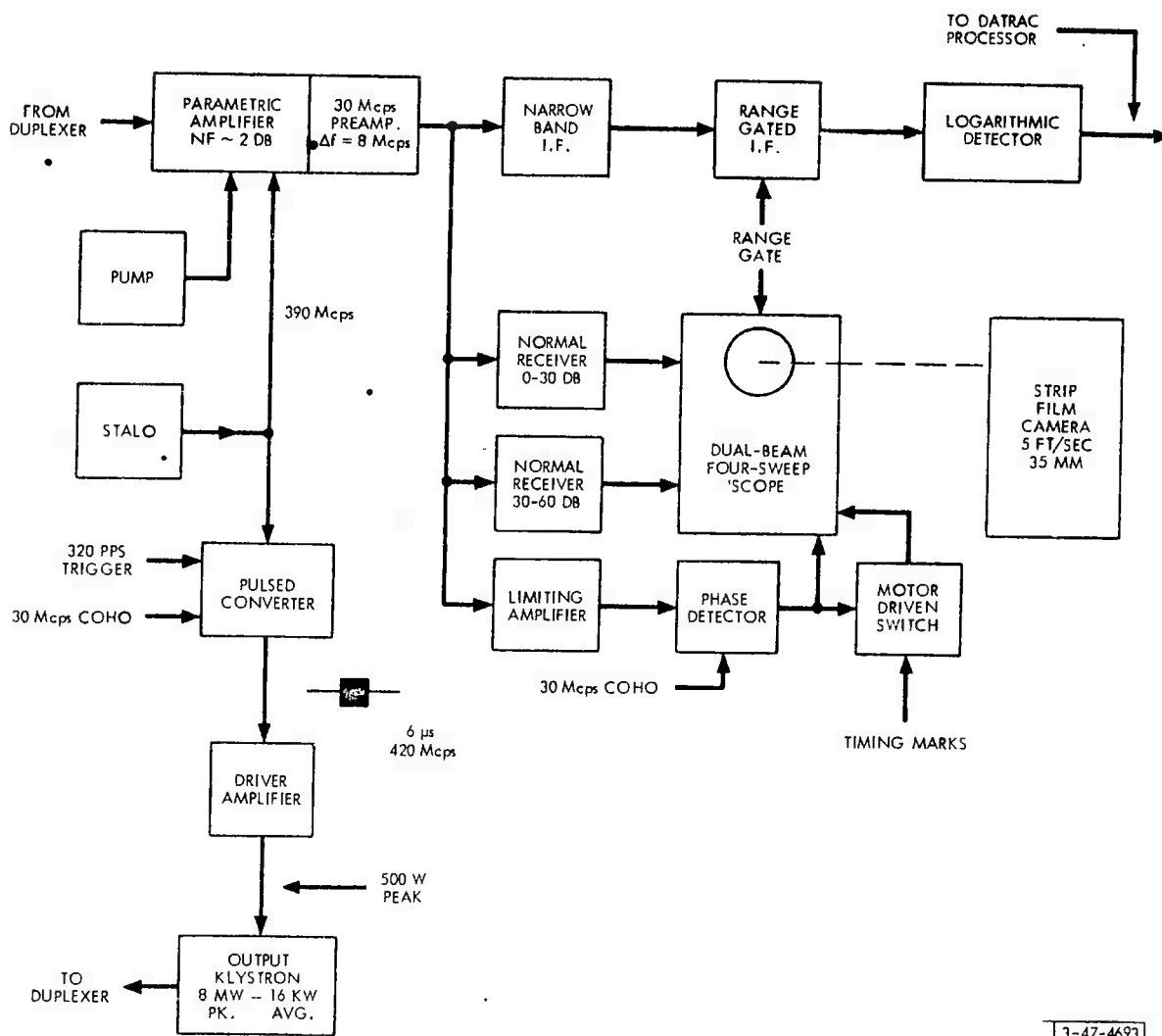
Fig. V-15. Block diagram showing the instrumentation added to UHF radar to permit phase measurements.

dual-beam oscilloscope. The third channel consists of a hard-limiting IF amplifier and phase detector, the reference for which is derived from the transmitter offset frequency oscillator. In order to minimize the overlap of successive traces on the film, the output of this channel is also displayed alternately on displaced traces of the second beam. Timing marks are diplexed at a low duty cycle once a second with one of these traces. The oscilloscope is triggered by the range tracking gate, and the display is photographed by a strip film camera having a film speed of 5 ft/sec. In order to preserve some of the detailed structure of the echoes, the bandwidths of all three channels were chosen to be 2 Mcps, despite the use of a 6-μsec transmitted pulse.

This equipment was first used during the Trailblazer lf firing. Figure V-16 is a typical film record of the amplitude and phase of an echo pulse observed on lf above 200,000 feet and before reentry effects became noticeable. The periodic modulation is caused by ringing in the transmitter modulator and pulse transformer. The slow variation of the phase across the pulse is largely due to the Doppler frequency shift. For an interval of about 0.1 sec at 195,000 feet, a "tail" of small amplitude and about 6-μsec duration appeared behind the otherwise normal echo pulse. Figure V-17 shows a typical echo in this altitude region. The main pulse continues to be coherent. The pulse-to-pulse phase of the tail is noisy (possibly due to the small signal level in the limiter). This phenomenon seems to disappear for a few pulses and then a large enhancement begins at 190,000 feet, as previously noted. Figure V-18 shows some of the anomalous pulse shapes observed during enhancement in the region below 190,000 feet. There does not appear to be any significant pulse broadening here.

7. Trailblazer Ic Optical Radiation Results

The optical data obtained during the reentry of Trailblazer Ic are shown in Fig. V-19. The associated trajectory and radar cross-section data had been previously reported in the Semiannual Technical Summary Report dated 31 December 1960. In order to illustrate the correlation between the radar and the optical data, the S-band radar cross section during this reentry is also plotted in Fig. V-19. The heights for the cross-section data are taken

|← 6μs →|

180°
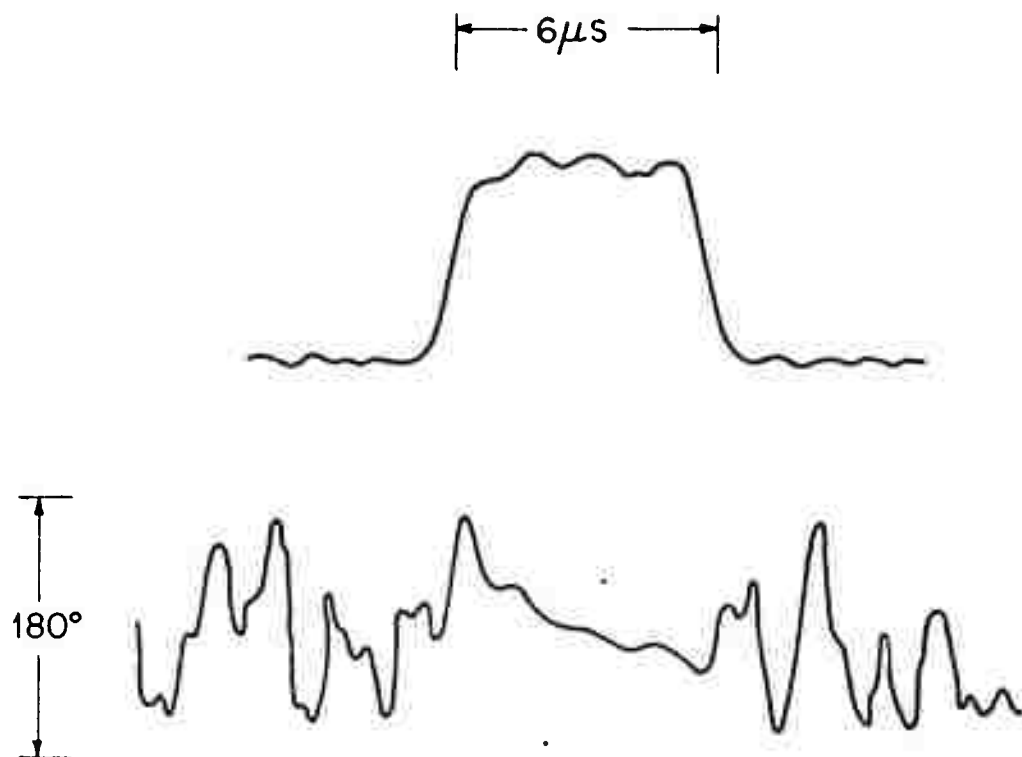
Fig. V-16. Tracings of film record of amplitude and phase of typical echo before large reentry effects occur (t = 356.17 sec; height = 225 kft).
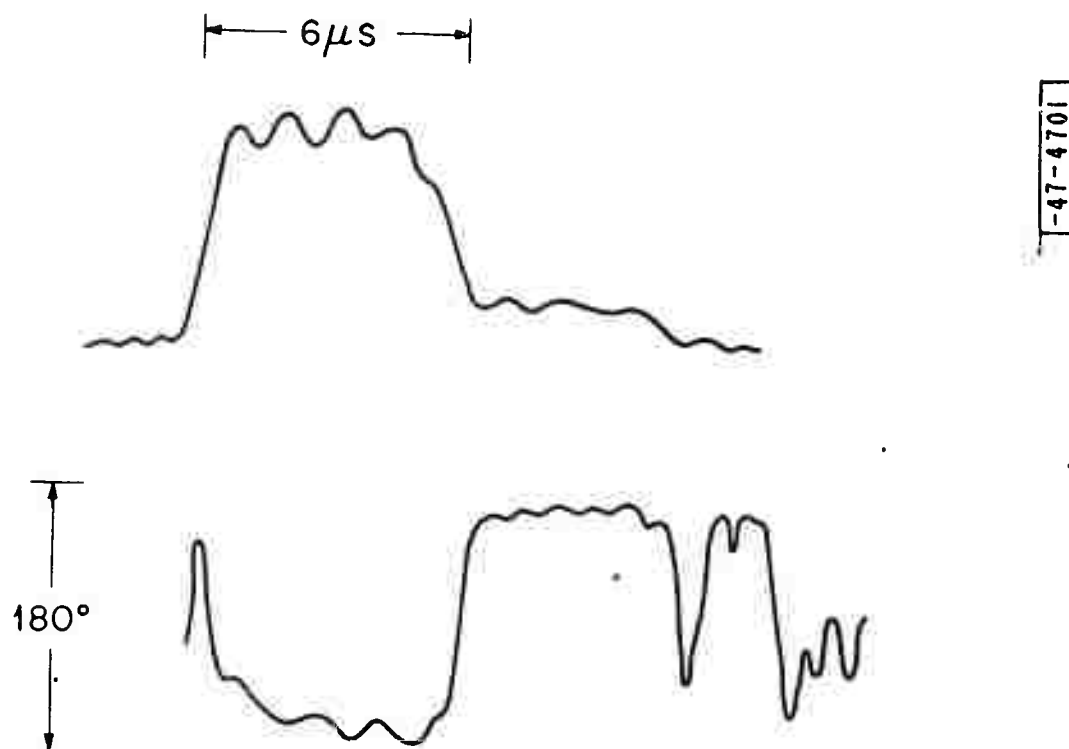
Fig. V-17. Tracings of amplitude and phase of an echo typical of those received during the time interval 357.98 to 358.09 seconds at a height of about 193,000 feet.
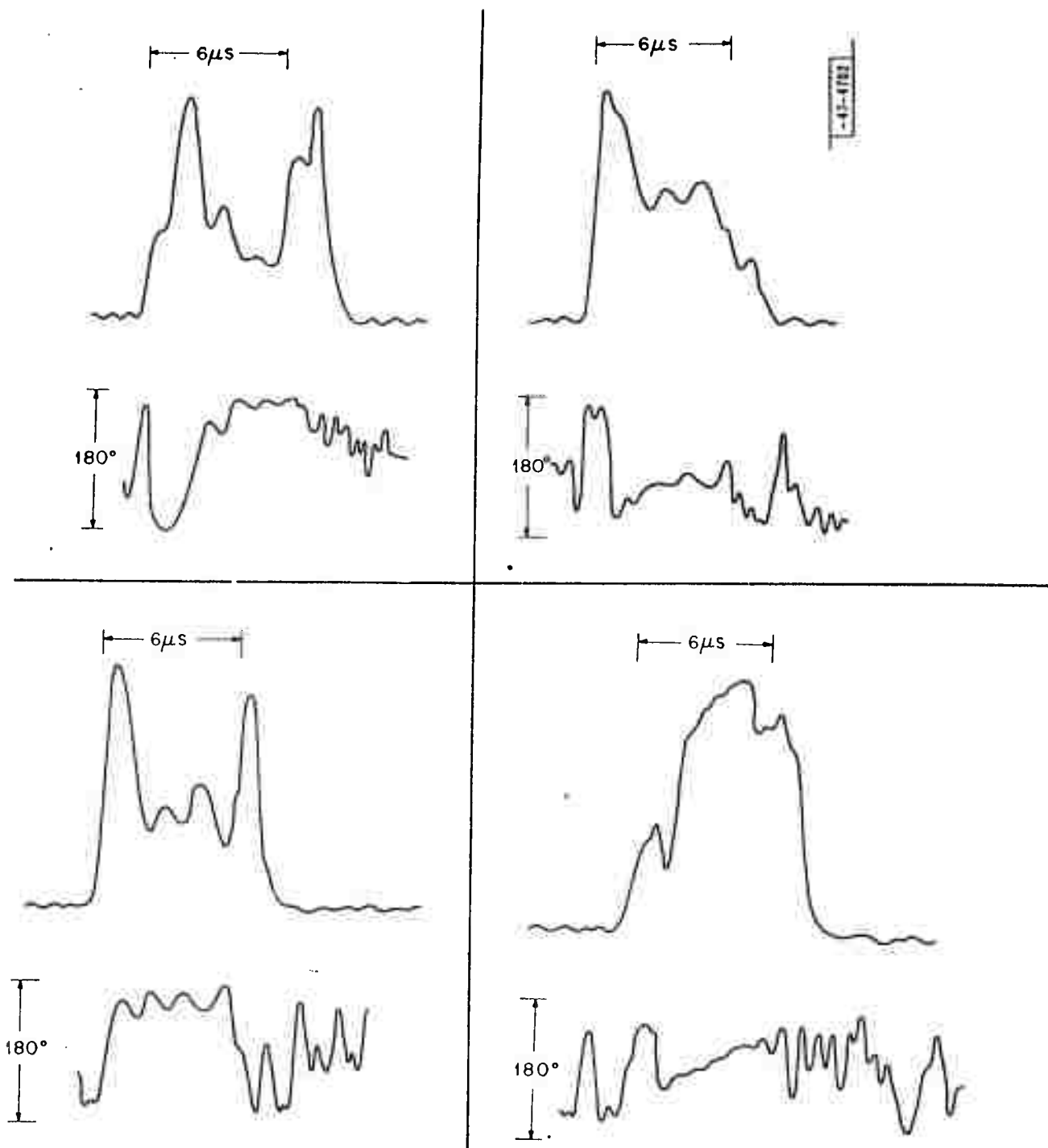
Fig. V-18. Tracings of the amplitude and phase of several echoes received during the "cross-section enhancement" region below 190,000 feet.

from the radar determined trajectory. The heights for the optical data are obtained from a two-station reduction of a pair of ballistic plates. The heights derived by these two methods agree to within about 2000 feet.

The measured photographic magnitude (M_{pg}), as plotted in Fig. V-19 in the range 0 to +3, applies to stars and meteors as seen on blue sensitive film at a standard source distance of 100 kilometers. The star Sirius, which is of spectral class AO, has a magnitude of −1.6 on this scale. The measured photographic magnitude should be convertible to the optically radiated power of the reentry body. This cannot be done rigorously at this time because the energy radiated by the reentry body per unit wavelength is not known. Until satisfactory spectrometric data are obtained, this conversion can only be estimated. Dr. R. E. McCrosky has made the following estimate of the absolute optical intensity.

If the source is flat from 3500 to 5500 angstroms (the radiation per second per angstrom is constant), then zero photographic magnitude (M_{pg} = 0) corresponds to 1×10^3 watts. The uniform distribution of light energy assumed here is completely arbitrary.

In equation form, this becomes

$$\text{Log } I = 3 - 0.4 M_{pg} \quad , \tag{V-1}$$

where I is the radiated power in watts.

Equation (V-1) is quite similar to the estimate for visual magnitude M_V made by Opik.[*]

$$\text{Log } J = 2.72 - 0.4 M_V \quad . \tag{V-2}$$

Here J is in "visual" watts and M_V is the visual magnitude adjusted for the spectral sensitivity of the human eye. The radiated power calculated from Eq. (V-1) is indicated as I (observed) in Fig. V-19. This conversion used here may be valid to within an order of magnitude. It is a preliminary estimate which will be modified when satisfactory spectral data are obtained. The curve marked I (theoretical, in watts) was computed using an equilibrium assumption. The optical radiation was assumed to emanate from the equilibrium gas cap. It is seen to be quite a bit lower than the observed values.

---

[*] E. J. Opik, Physics of Meteor Flight in the Atmosphere (Interscience Publishers, Inc., New York, 1958), p. 147.
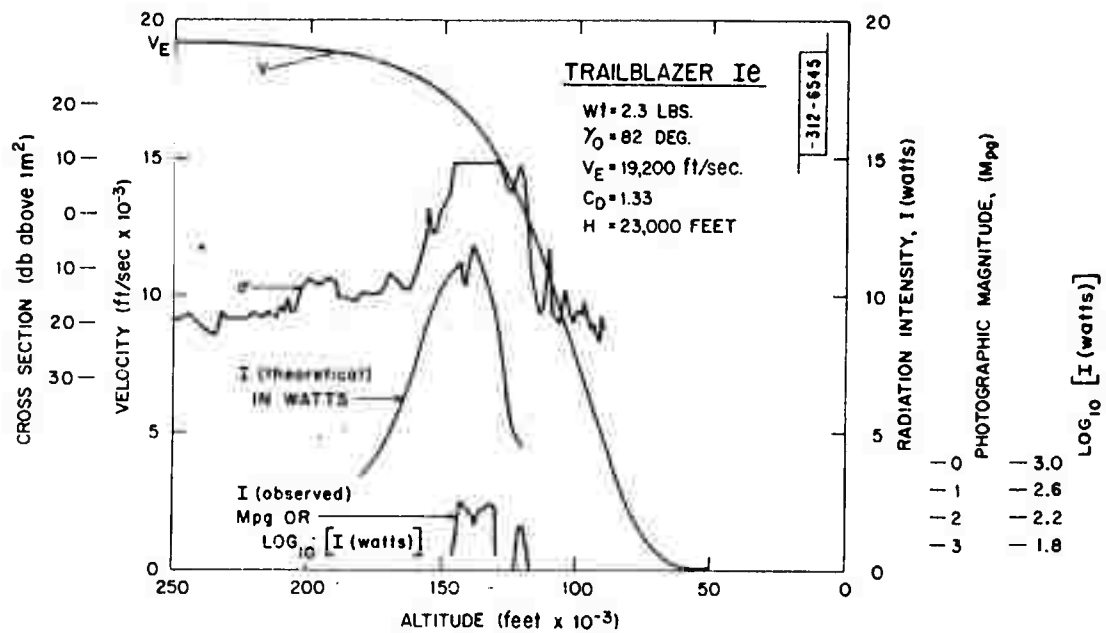
Fig. V-19.   Trailblazer Ie results.

PRINCIPAL CONTRIBUTORS FOR SECTION V

The principal contributors in the various areas are:

RADAR SYSTEMS

E. O. Gronroos, E. Barsack, V. J. Guethlen, H. L. Kasnitz,
H. W. Rudolph, E. F. Tarbox — Group 312

RADAR EQUIPMENT

Antenna Design and Testing

L. J. Ricardi, B. F. LaPage, M. H. Malone, C. A. Lindberg — Group 315
E. F. Tarbox — Group 312

Mechanical Design, Gun Mount Modifications, Controls and Installation

E. W. Blaisdell, M. W. Brawn, E. Jozefowicz, H. A. MacDonald,
A. M. Sanderson — Group 39

F. L. Bacchialoni, V. J. Guethlen, E. F. Tarbox, L. A. Garavano —
Group 312

. F. B. Magurn — Group 21

Site Operations and Testing

J. M. Sobolewski, F. B. Magurn, O. V. Fortier, L. C. Wilber,
P. J. Harris, F. E. Heart, J. H. Hagler, F. L. Carroll, J. C. Howard,
A. C. Dyer, III — Group 21

Data Processing Equipment

R. M. Coles, P. J. Harris, E. J. Peters, K. H. Morey,
E. E. Schowengerdt — Group 21

Parametric Amplifier and Maser Systems

C. Blake, J. F. Bushee — Group 46

Coherent Receiving Systems

G. R. Armstrong, J. P. Perry — Group 47

OPTICS EQUIPMENT

R. V. Meyer, R. G. Burgess, D. R. Dibley, M. Woronoff, R. H. Baker,
E. R. H. Teodorson — Group 312

E. W. Blaisdell, M. W. Brawn, A. M. Sanderson — Group 39

J. Knight — Group 32

PROGRAMMING AND DATA ANALYSIS

S. M. Ornstein, R. J. Saliga — Group 21

P. A. Willmann, L. G. Peterson, H. L. Kasnitz — Group 312

SITE ENGINEERING AND CONSTRUCTION

D. C. Moore, J. B. Paddleford, E. L. Clarke, E. P. Gaudette,
R. J. Sutherland — Group 75

VI. THE PRESS PROGRAM

A. AIRBORNE OPTICAL MEASUREMENTS

The optical measurements program for Project PRESS has as one of its objectives the correlation of information from all sensors (ground-based and airborne) including the TRADEX radar. The existence of a large ground-based tracking radar on Roi-Namur (TRADEX) creates the potentiality of pointing narrow-field airborne optical instruments at the single target being tracked by TRADEX. The system proposed to accomplish this function is the airborne optics control subsystem.

1. Airborne Optics Control Subsystem

a. General

The airborne optics control subsystem can be divided into two major parts; namely, the ground-based equipment shown in Fig. VI-1 and the airborne equipment shown in Fig. VI-2. The ground-based equipment will be installed on Roi-Namur. Each of the three aircraft (KC-135, WV-2 and A3D) to be based at Eniwetok will carry the equipment shown in Fig. VI-2.

Plans are under way to provide and install the ground-based equipment. This would include at least the following individual equipments:

        (1) Search radar,

        (2) Three station-keeping radars (SKR),

        (3) Three special-purpose computers,

        (4) Ground-to-air and air-to-ground data links,

        (5) Aircraft control center equipment,

        (6) Special radar beacons and altimeters to be installed in the aircraft.

Pointing angles computed in the special-purpose computers accurate to one angular mil will be transmitted to the aircraft. Altitude data from the altimeter, target position data from TRADEX and aircraft position data from the SKR are the inputs to the computer required to make the pointing-angle computation.
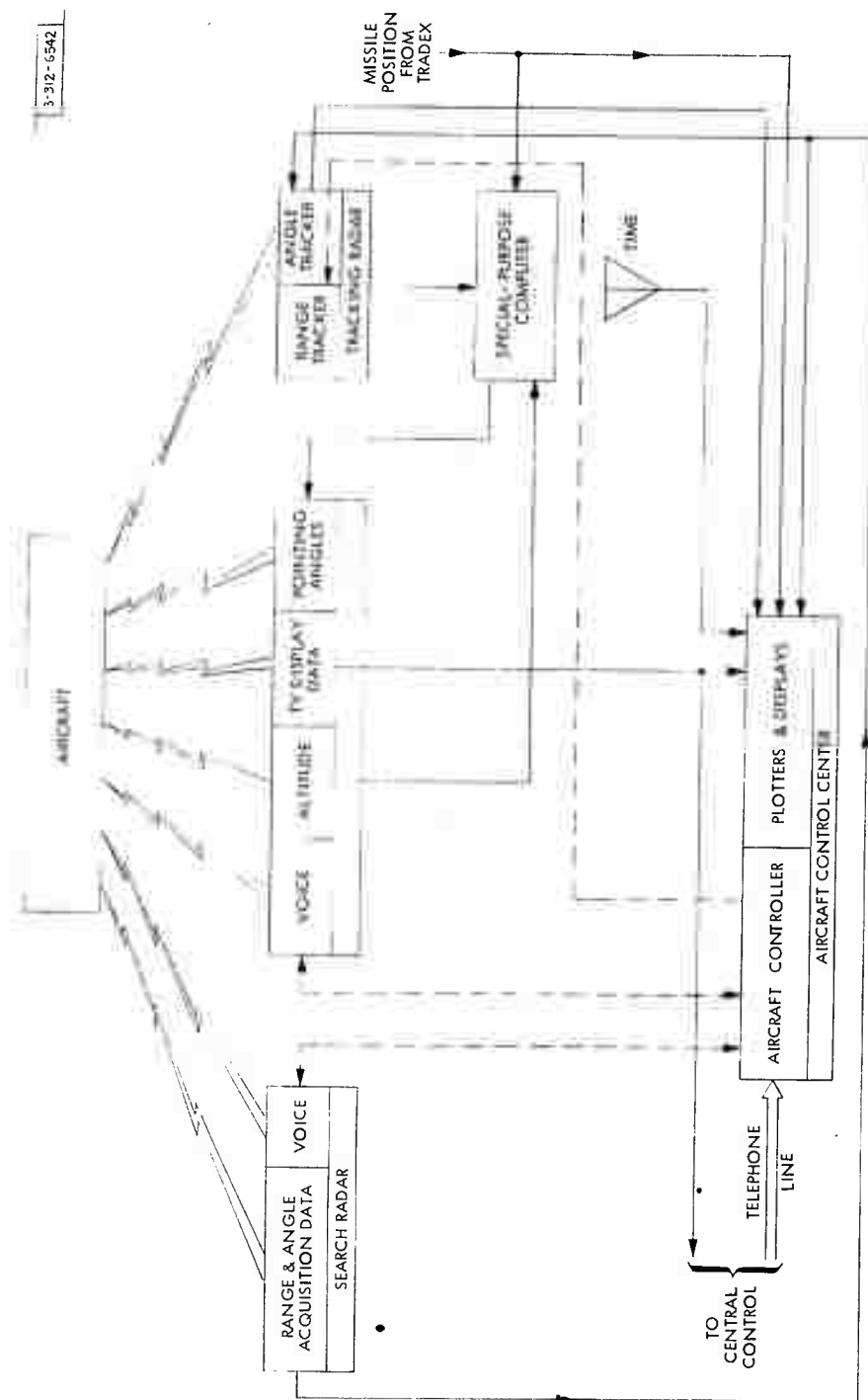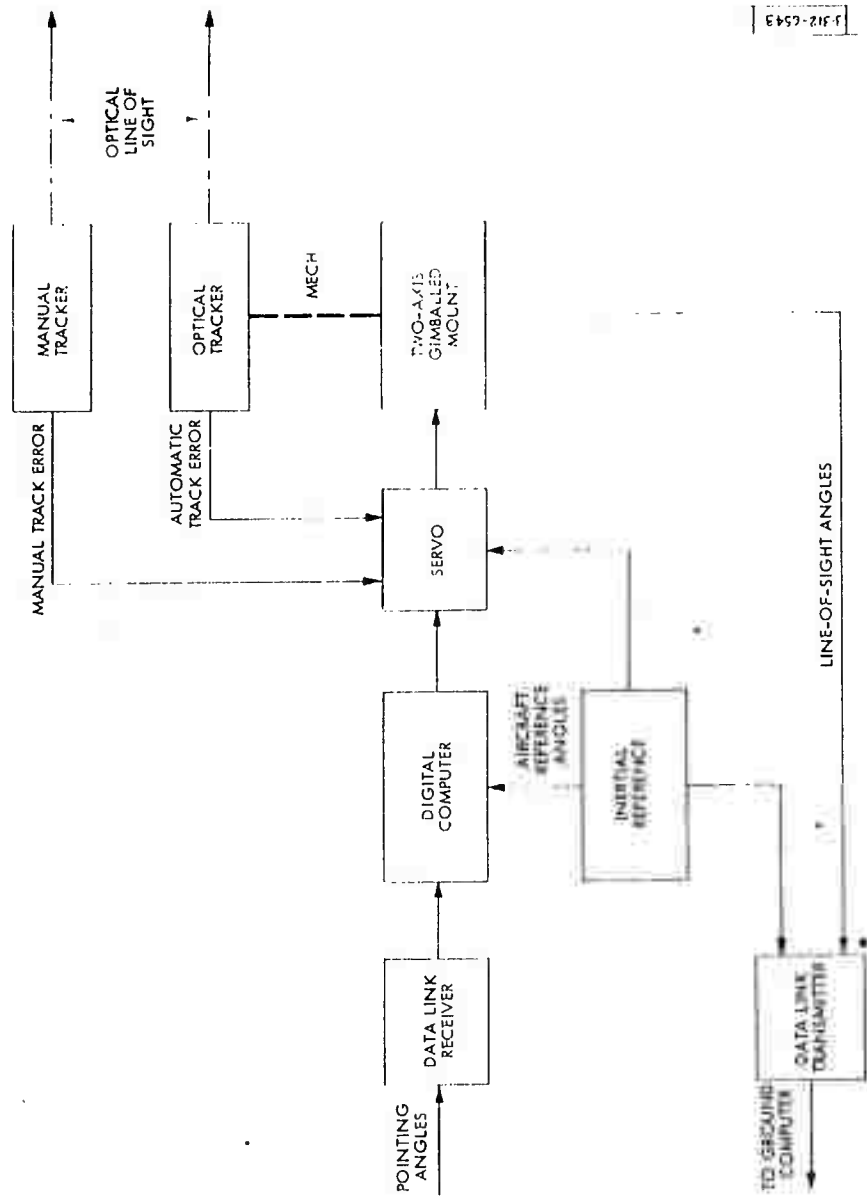
Fig. VI-1. Block diagram of airborne optics control subsystem.

Fig. VI-2. Pointing and automatic tracking equipment in PRESS aircraft.

Several technical discussions between Lincoln Laboratory and the Bendix Systems Division have taken place during this period. The purpose of the discussions were twofold: namely, to become familiar with the present implementation in the KC-135 (Skyscraper) and the WV-2 and to assess the magnitude both in time and cost to modify the scheduled implementation for Project PRESS. Bendix submitted an informal estimate of the cost to Lincoln Laboratory to modify the KC-135 and WV-2 instrumentation to conform with the Lincoln Laboratory recommendations. This material was submitted and discussed at the ARPA meeting on Airborne PRESS at the Pentagon on 15 June 1961.

b. System Study

A study of the various sources of error has been initiated at Lincoln Laboratory to determine component requirements of the airborne optics control subsystem. The errors are of several types:

(1) TRADEX measurement errors.

(2) SKR measurement errors.

(3) Errors due to extrapolating (in time) the pointing angles to be transmitted to the aircraft in order to offset the time lags between the reception of radar information and the time when the optical sensors can be repointed. This type can be considered small compared to the errors of types (1) and (2).

(4) Errors due to refraction. The error in elevation can be minimized by reading height from a radar altimeter; however, it is necessary to correct for the range of the aircraft by means of available tables. Refraction errors should be unimportant for TRADEX because the missile elevation should always exceed 10°.

(5) Errors in the servo system.

(6) Errors in the aircraft's inertial system.

A series of equations has been written and programmed to discover the effect of the above errors on the final pointing accuracy. In this computer study, errors of types (3) and (4) were increments to the errors of types (1) and (2). The results of the computer runs indicate that the final pointing errors are strongly geometry dependent. In particular, the errors are approximately

proportional to the ratio between the distance from TRADEX to the missile and the distance from the aircraft to the missile. A typical case was computed for the following:

(1) TRADEX errors (one sigma value)

| Range | 50 feet |
| Azimuth and elevation | 0.3 milliradian |

(2) SKR errors (one sigma value)

Range	30 feet
Azimuth	0.2 milliradian
Height	50 feet (measured by altimeter)

(3) Location of missile relative to TRADEX

Range	225 n.mi
Azimuth	230°
Elevation	10°

(4) Location of missile relative to SKR

Range	200 n.mi
Azimuth	230°
Altitude	20,000 ft

The computer run for the above conditions led to a one sigma pointing error of 0.87 milliradian in elevation and 4.9 milliradians in azimuth. For this case, the inaccuracies of the radars contribute about one-half of the total permissible pointing error when using one sigma value for the radar errors. Errors due to types (5) and (6) can be added to the computer errors of types (1) through (4) by taking the square root of the sum of the squares.

In addition to these error studies, some approximate conclusions can be made concerning the characteristics of the station-keeping computer. Station-keeping equations have been written for several proposed coordinate systems. In all cases, about a dozen equations must be evaluated including perhaps ten trigonometric functions. Assuming that pointing angles must be transmitted about twenty times a second, this will require a computer about one-tenth as fast as an IBM 7090 (a 7090 takes about 400 microseconds for each trigonometric function). The station-keeping computer should require about 1000 words of core storage as compared with approximately 30,000 for the IBM 7090 computer.

c.   Altimeter Survey

A survey of a number of radio altimeters has been carried out with regard to their accuracy, reliability, and availability.   At the present time, two altimeters have been selected for further investigation.   These are the AN/APN-42 and the AN/APN-110.   All the data have not yet been collected on these two models, but a number of the factors which will be involved in the final choice are discussed briefly below.

Several models of the AN/APN-42 have been thoroughly flight-tested in the past, and it appears to be a reliable unit.   Its accuracy, however, falls somewhat short of that required by the PRESS Program.   Discussions of the feasibility and effectiveness of minor redesign to improve accuracy are continuing.   Although not currently in production itself, this instrument is embodied in a combination low- and high-range unit (AN/APN-120) which is being built for the Navy by Emstron.   The lead time to get the AN/APN-42 high-range unit alone is estimated at six months.   Thus, availability may be a major factor for either of the altimeters under consideration, and both will have to be modified to adapt them for a digital-data output.

The AN/APN-110 is the altimeter that was designed by RCA for the B-58. The servo and resolver of this unit give a shaft accuracy well within PRESS requirements but, in accuracy tests performed by RCA in 1957, erratic behavior of the linear potentiometers used to give the analog output made actual instrument accuracy quite poor.   Subsequent advances in the field of film potentiometers indicate that this problem can be surmounted without difficulty. Availability is not expected to be as much of a problem with this altimeter as with the AN/APN-42.   Flight-test accuracy checks are presently becoming available and, if the accuracy and reliability of the AN/APN-110 prove to be satisfactory, then it appears that this altimeter will be the one chosen for the PRESS aircraft.

d.   Radar and Beacon Survey

A survey of search and tracking radars suitable for the airborne optics pointing subsystem has been initiated.   The AN/FPS-20 search radar is capable

of good skin-track performance against the PRESS aircraft at 325 miles, the approximate distance from Roi-Namur to Eniwetok. This radar used in conjunction with the Mark 10 SIF (selective identification feature) beacon equipment can provide a reliable system for aircraft detection and identification. The Mark 10 SIF is equipped with a number of codes for aircraft identification. The FPS-20 is an L-band radar with a 1.3° beam in azimuth and 60° coverage in elevation. Further study will be given to the surveillance problem before a selection is made.

A cursory examination of the NIKE series radars for the station-keeping task has been made. A detailed study of the modifications required in adapting them for this application is being initiated. A survey of beacons to be used in conjunction with the trackers has also been initiated. Aircraft tracking by the SKR's will depend on tracking airborne beacons.

e.   Inertial Reference and Optical Mount Study

An inertial reference system with small errors in heading and verticality is essential if the airborne optics pointing subsystem is to provide a 3σ pointing error of 0.5°. A preliminary error study indicates that the heading and vertical reference errors should be less than a milliradian. Conferences have been held with the M.I.T. Instrumentation Laboratory staff on this subject. It is their opinion that the state of the art can easily provide a heading reference good to 1 milliradian and a vertical reference to 0.5 milliradian. The Instrumentation Laboratory staff had some reservations on the wisdom of using the B-50 turret as a two-axes platform to carry the optical sensors. It is their recommendation that the inertial reference system and the mount carrying the optical sensors be one integrated mechanical assembly. This configuration would eliminate the pick-off error in slaving the B-50 turret to the inertial platform. How small the B-50 turret error will be after improvement is unknown at this time. An investigation will be made during the next period to ascertain the ultimate performance of a modified B-50 turret, and an inertial reference platform will be selected.

2. Optical Instrumentation

A second objective in Project PRESS has been to standardize the optical instrumentation utilized on the aircraft as much as possible. Provision has been requested to have both the trackers on the A3D and the WV-2 aircraft be the same two-color tracker with fields of view of 0.5° and 2.0°. The ground-based control subsystem has been specified to point the airborne instruments with a 3σ error of 0.5°. This number was chosen to be smaller than the probable separation of targets when the tankage is not fragmented. Hence the airborne tracker with a restricted field of view has the option of acquiring only the target being tracked by the TRADEX radar. Since the early radiation may be more intense in the visible portion of the spectrum, the tracker should be capable of acquiring and tracking in both the visible and the infrared. Furthermore, the sensitivity of the photoelectric mode should permit earlier acquisition.

The cinespectrographs should be standardized to a common type with 70-mm film transports, since the remote field site at Eniwetok requires that all redundant equipment be standardized in the interest of repair, spare parts, etc. Lincoln Laboratory is purchasing seven special 70-mm film transports for the cinespectrographs, boresight and long-focal-length cameras. The special transports have the capability of continuously varying their shutter openings and have a means of rapidly accelerating the frame rate in a single jump of 10 (both features operable while the camera is operating). The purpose of this special capability is to extend the dynamic range of the photographic measurements. A change in shutter opening of 60 multiplied by a change of 10 in the frame rate would multiply the dynamic range of the film itself by 600. The standardization of all film transports should also facilitate a single film reading technique. The data recorded on each frame, i.e., time, shutter opening, frame rate, filter etc., can be automatically read off the film.

All image tube systems, orthicons and IR vidicons should have provision for video recording of their data. The loss in information content resulting from photographing the monitor requires that means be provided to retain and extract the maximum data from image tubes.

The timing system provided by Lincoln Laboratory is to be installed in all aircraft. The secondary time standards in each aircraft will provide synchronized time signals for all sensors.

Plans have been initiated to utilize the forward position of the KC-135 cargo door for a long-focal-length camera. The subcontract study by Cornell Aeronautical Laboratory has demonstrated the feasibility of a long-focal-length camera aboard an aircraft which could be capable of resolution in the order of one second of arc. The mount design required, however, would indicate the use of a large aircraft and fixed plane window. The useful aperture must be in the order of 12 inches. The short exposures required for high resolution demand that a large aperture be used. The restricted field of view of such an instrument will require a precise tracking mount with its own tracker. Because of the flexure of the airframe between the Skyscraper platform and the area available for the long-focal-length camera, the instrument must be separately slaved to the airborne optics control subsystem. The long-focal-length camera will have a color wheel synchronized to the shutter which will permit the phenomena to be successively photographed through a ... ries of preselected filters.

The list of airborne optical instrumentation given in the Preliminary Description of the Experimental Program and Operational I . = for Project PRESS are to be purchased and installed in the aircraft by the Service Agencies. The Service Agencies are now preparing their lists for this equipment. Several discussions have been held with the Service Agencies and the final lists of equipment will soon be submitted to Lincoln Laboratory.

B. METEOROLOGICAL DATA REQUIREMENTS

A survey of the upper atmosphere and surface meteorological data requirements has been made for Project PRESS. The upper atmosphere data requirements are as follows:

Data Required	Altitude Requirements
Temperature	Measured: surface to 130,000 ft. Calculated from density measurements: 100,000 to 300,000 ft.

Data Required	Altitude Requirements
Water vapor pressure	Measured: surface to 130,000 ft.
Pressure	Measured: surface to 130,000 ft. Calculated and/or measured: 100,000 ft. to 300,000 ft.
Wind direction	Surface to 130,000 ft. If possible, 100,000 to 300,000 ft.
Altitude of sounding devices	Surface to 300,000 ft.
Density	Calculated: surface to 130,000 ft. Measured: 100,000 to 300,000 ft.
Cloud cover	Surface to 130,000 ft.
Ozone	Measured: surface to 130,000 ft.
Refractive index	Measured or calculated: surface to 50,000 ft.
Nuclear concentration	Measured: surface to 50,000 ft.
Composition to determine dissociation and recombination	Measured: 200,000 to above 300,000 ft.

The surface meteorological data requirements are:

Data Requirements	Location
Temperature, pressure, relative humidity, wind speed and direction	Kwajalein and Roi-Namur
Surface and upper air weather charts	Kwajalein

C. RADAR INSTRUMENTATION

A report is in preparation which will outline the recommendations of the TRADEX Radar Panel. These will include suggestions for the initiation of both "short-term" and "long-term" work. It is intended that the short-term additions and supplements be incorporated or be available at the time of the initial radar checkout, or soon thereafter. The long-term items will constitute major modifications or replacements of the original equipment and are intended for use when these extensive modifications are deemed to be warranted, presumably about 6 to 12 months after operations begin. The short-term items will include the following:

> L-band parametric amplifiers
>
> Simulation studies
>
> Theoretical studies
>
> Supplementary data recording
>
> Changes to acquisition and track
>
> Multiple range gates.

The long-term items will include:

> A versatile L-band transmitter and associated high-power microwave components
>
> A new receiving and data-recording system for the improved L-band radar

An outline of a more extensive report has been prepared. This will include a description of the TRADEX radar system, an assessment of its measurement capability, and a detailed justification of the recommendations that will be presented in the earlier report.

D. PACIFIC RANGE MEASUREMENTS

1. General

In mid-April 1961, Group 32, Pacific Range Measurements, was chartered within Division 3 and given responsibility for the Lincoln Laboratory activities relating to:

(a) The ground-based elements of the PRESS down-range system, including the TRADEX radar, the data-processing complex, the interface equipment, the three optical stations, and the required communications complex.

(b) The on-site conduct of experiments, involving not only the ground instruments mentioned above, but also the three airborne optical platforms and their associated control system.

(c) On-site data reduction and interpretation in sufficient detail to permit judgments concerning system changes in preparation for further experimentation.

2. Operating Organization Plans

Since the group was chartered, some thought has been given to planning an on-site organizational structure able to carry out the PRESS experiments
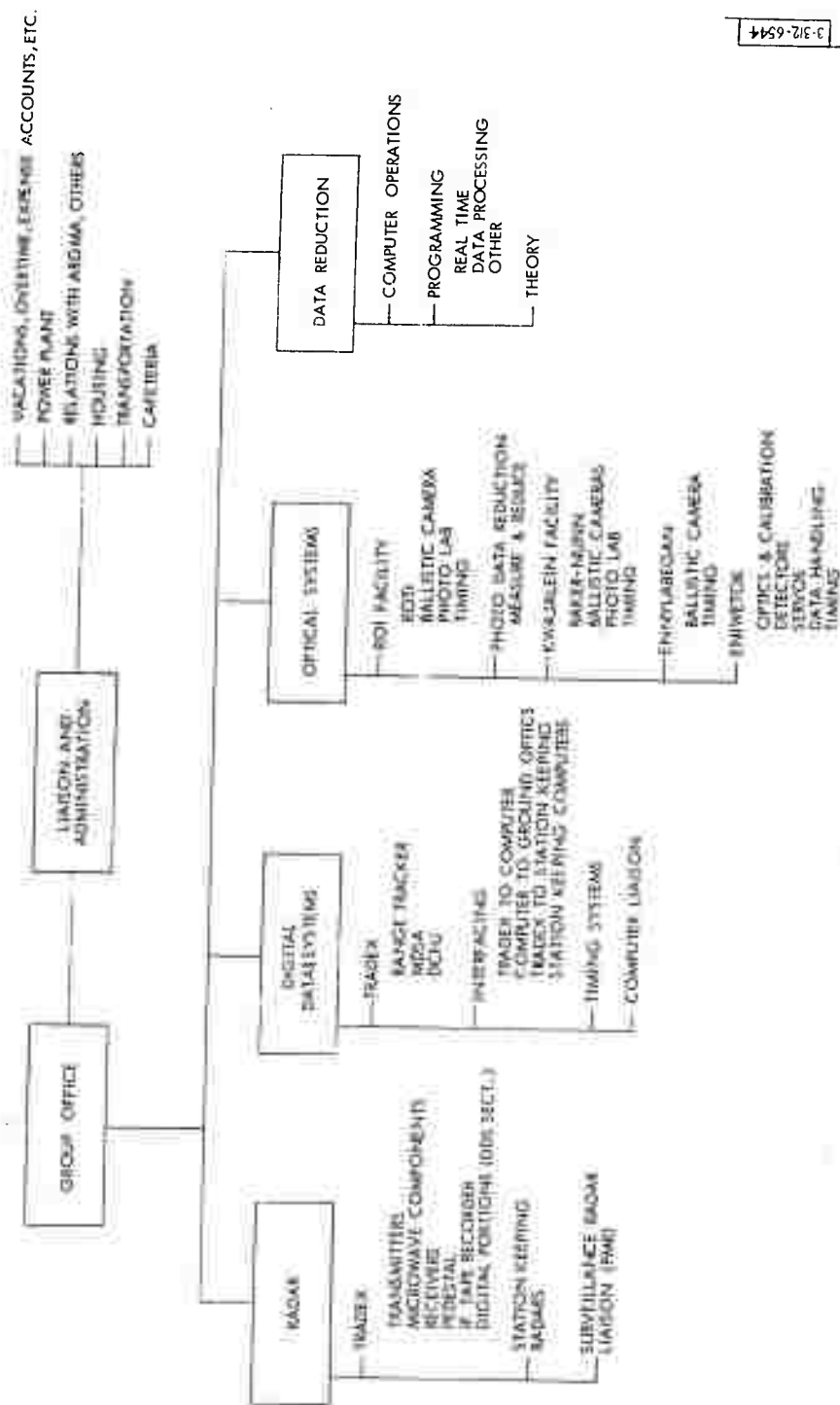
Fig. VI-3. PRESS operating group organization.

as presently visualized. The chart of Fig. VI-3 reflects the planned structure of the down-range operating group.

Each of the major areas is expected to require of the order of four high-level Lincoln Laboratory staff members on Roi-Namur. In the optical area, however, the Eniwetok portion involving the airborne optics is expected to require a complement of some nine staff members resident on Eniwetok, but still reporting to the Group 32 office on Roi-Namur. Lincoln staff in the area will thus total between 26 and 30.

In the radar area, it is planned, in addition to the four Lincoln engineers, to have a complement of between ten and fifteen engineers of RCA, Moorestown, assisting in the operation and maintenance of TRADEX. These people will be arranged for under a Lincoln subcontract. This arrangement has the advantage not only of holding required Lincoln staffing to the figures mentioned above, but also of providing on-site people familiar with TRADEX (it will be remembered that the ARGMA contract for TRADEX does not call for instruction books).

With respect to non-staff personnel, a number of decisions remain to be made. It is expected, as is usual with many operations, that approximately twice as many non-staff (technician level) personnel will be required as staff members. It is expected that a high percentage of these will be obtained under contract with one of the service organizations whose business it is to supply such people. In particular cases, however, it may be desirable to have certain non-staff personnel directly on the Lincoln Laboratory payroll.

This sort of planning will, of course, continue until the group is actually located on site and operating the equipment.

3. PRESS Subsystems

At the present time, specifications and/or work statements covering the following major items of PRESS hardware have been prepared:

Specification	Comment
PS-1 Computer	Five proposals received; evaluation in progress.
PS-2 Timing System	Contract let with Hermes Electronics. Delivery on a schedule compatible with PRESS.

Specification	Comment
PS-3 Communications Plan	This document revised at request of ARGMA and its provisions agreed upon by Lincoln, RCA (TRADEX) and ARGMA.
PS-4 Optical System for a Modified Baker-Nunn Slitless Spectrograph	Contract let to Perkin-Elmer, Norwalk, Conn. They will begin fabrication 1 July and will deliver finished product 1 January 1962.
PS-5 Large Objective Prism	Specifications now out for bids; bids will be closed 15 July.
PS-6 Ballistic Camera	Contract let to Boller and Chivens, So. Pasadena, Calif. Production work has started. Cameras will be ready approximately 1 January 1962.
PS-7 Modified Baker-Nunn Slitless Spectrograph Camera	Contract released Friday, 16 June. Order is in the hands of the manufacturer and work will begin immediately. This is due for delivery in May 1962.
PS-8 Airborne Optics Control Subsystem	Design requirements have been specified by Lincoln. Contractual arrangements with RCA for the equipment required are under consideration.
PS-9 PRESS Control Center	Design philosophy being worked out.

The work reported in this section was prepared by V. J. Guethlen, R. V. Meyer, P. Willmann, J. Whitman, J. P. Perry, J. H. Meyer and P. B. Sebring.